

The spectral energy distributions and the bolometric luminosities of local AGN: study of the complete 12 μ m AGN sample

LUIGI SPINOGLIO ¹, JUAN ANTONIO FERNÁNDEZ-ONTIVEROS ^{2,1} AND MATTHEW A. MALKAN ³

¹*Istituto di Astrofisica e Planetologia Spaziali (INAF-IAPS), Via Fosso del Cavaliere 100, I-00133 Roma, Italy*

²*Centro de Estudios de Física del Cosmos de Aragón (CEFCA), Plaza San Juan 1, E-44001, Teruel, Spain*

³*Department of Physics and Astronomy, UCLA, Los Angeles, CA 90095-1547, USA*

ABSTRACT

We measure the bolometric luminosity of a complete and unbiased 12 μ m-selected sample of active galactic nuclei (AGN) in the local Universe. For each galaxy we used a 10-band radio-to-X-ray Spectral Energy Distribution (SED) to isolate the genuine AGN continuum in each band, including sub-arcsecond measurements where available, and correcting those contaminated by the host galaxy. We derive the median SED of Seyfert type 1 AGN, Seyferts with hidden broad-lines (HBL), Seyferts of type 2, and LINER nuclei in our sample. The median Seyfert 1 SED shows the characteristic blue bump feature in the UV, but nevertheless the largest contribution to the bolometric luminosity comes from the IR and X-ray continua. The median SEDs of both HBL and type 2 AGN are affected by starlight contamination in the optical/UV. The median SED of HBL AGN is consistent with that of Seyfert 1's, when an extinction of $A_V \sim 1.2$ mag is applied. The comprehensive SEDs allowed us to measure accurate bolometric luminosities and derive robust bolometric corrections for the different tracers. The 12 μ m and the K -band nuclear luminosities have good linear correlations with the bolometric luminosity, similar to those in the X-rays. We derive bolometric corrections for either continuum bands (K -band, 12 μ m, 2-10 keV and 14-195 keV) and narrow emission lines (mid-IR high ionization lines of [OIV] and [NeV] and optical [OIII]5007Å) as well as for combinations of IR continuum and line emission. A combination of continuum plus line emission accurately predicts the bolometric luminosity up to quasar luminosities ($\sim 10^{46}$ erg s⁻¹).

Keywords: Active galactic nuclei (16); AGN host galaxies (2017); Seyfert galaxies (1447); Infrared photometry(792); Infrared spectroscopy (2285); Ultraviolet photometry(1740); X-ray active galactic nuclei (2035)

1. INTRODUCTION

The determination of the bolometric luminosity of active galactic nuclei (AGN) is important, to study the AGN phenomenon in itself, which is sustained by an accreting supermassive black hole (SMBH; see, e.g., Rees 1984) and, on the other hand, to understand the role of AGN in galaxy evolution.

The need to place the Seyfert nucleus phenomenon in the framework of galaxy evolution was already clear more than 40 years ago. It was realized that the most universal major contributions to the bolometric luminosity of AGN come from the hard X-ray and the mid-IR bands. For the former, we know that the X-ray band emission is characteristic of AGN: X-ray emission is ubiquitous in AGN and is thought to be produced by comptonization of UV/optical disc photons by a corona of hot electrons located above the black hole. For the latter, in fact, the mid-IR, and in particular the

IRAS 12 μ m band has been used to select a complete sample of AGN (Spinoglio & Malkan 1989; Rush et al. 1993; Spinoglio et al. 1995) because it was realized that this band was carrying a constant fraction of the bolometric luminosity of different types of low redshift AGN, including Seyfert galaxies of type 1 and type 2, and quasars. This result arises from the fact that AGN energy distributions are roughly described by a one-parameter family: a relatively blue quasar continuum altered by varying amounts of nuclear dust. The dust preferentially absorbs continuum at the shortest wavelengths and re-emits it in the far-infrared. These two processes make the resulting energy distribution redder in the optical/ultraviolet, and in the IR. However, there is a pivot wavelength, at which the absorption of the original continuum is balanced by the thermal re-emission. This occurs in the mid-IR and in fact, 7-12 μ m is the only wavelength range where both of these effects (absorption and re-emission) are relatively small (Spinoglio & Malkan 1989).

This study was based on the large-aperture IRAS data (Neugebauer et al. 1984), possibly contaminated by emission from the host galaxy. It therefore needed to be re-examined using mid-IR observations of the intrinsic nuclear emission of the AGN.

The first determination of the bolometric luminosity of low redshift quasars has been done by Sanders et al. (1989) who presented multi-wavelength observations ($10^{9.7}$ – 10^{18} Hz) of 109 bright quasars from the Palomar-Green (PG) survey (Schmidt & Green 1983) and showed that the PG quasars emit the bulk of their luminosity (typically more than 90%) between 3000\AA and $300\mu\text{m}$. A few years later, Elvis et al. (1994) integrated the energy distributions of 47 quasars selected mainly from the PG, 3C, and Parkes catalogs, using a simple linear interpolation through the data points in $\log \nu L_\nu$ space, i.e., connecting the individual points with a power law and derived bolometric corrections for UV, visible, and infrared monochromatic luminosities. They lacked complete data from the hard X-ray bands, and their sample was primarily an ultraviolet-excess selected sample, and biased toward relatively X-ray loud quasars.

Following that pioneering work there have been a few determinations of the bolometric luminosity of AGN, either from selective measurements of the continuum in various spectral ranges and assuming templates to reproduce the spectral energy distributions (SED) of AGN (e.g. Marconi et al. 2004; Hopkins et al. 2007; Lusso et al. 2012), or from observations of spectral lines (e.g. Meléndez et al. 2008; Spinoglio et al. 2022). These estimates assume that the measured radiation is isotropic and that simple bolometric corrections can recover the total luminosities of most AGN.

Marconi et al. (2004) used the following approach to derive the bolometric corrections, i.e. the corrections to be applied to an *observed* luminosity to derive the *total intrinsic*, i.e. bolometric, luminosity of the AGN. Their argument is that although the observed SED of an AGN provides the total observed luminosity (L_{obs}), this does not give an accurate estimate of the BH mass accretion rate because it often includes reprocessed radiation (i.e. radiation absorbed along other lines of sight and re-emitted isotropically). In their view, the accretion rate is related to the total luminosity directly produced by the accretion process, which they call the total intrinsic luminosity L_{int} . In AGN, L_{int} is given by sum of the optical–ultraviolet and X-ray luminosities radiated by the accretion disc and hot corona, respectively. They consider that, in order to estimate L_{int} , one has to remove the IR bump (2.5–60 microns) from the observed SED of unobscured AGN to avoid double counting the source luminosity, i.e. extinction-corrected X-ray emission and reprocessed IR emission. Marconi et al. (2004) used a template spectrum for the AGN, based on the observed optical-UV and X-ray spectra, excluding the observed IR bump, following the above ar-

gument. From the assumed template they compute the bolometric corrections with respect to the optical B-band, and the soft and hard X-ray bands.

With the aim of determining the bolometric quasar luminosity function, Hopkins et al. (2007) have taken a similar approach to the one of Marconi et al. (2004) in calculating the template spectrum, but they included in the template the observed IR bump, giving a more detailed treatment of the optical/IR. In particular, they used the Richards et al. (2006) template spectrum in the B, g and i optical bands and a different determination of the spectral index between optical and X-rays (α_{ox}).

They also found a dependence of the bolometric correction on the luminosity. They used a compilation of many AGN samples, selected from the optical, the soft X-rays, the hard X-rays and also at 8–15 μm , including the 12 μm AGN sample (Rush et al. 1993).

Vasudevan & Fabian (2007) showed that the variations in the disc emission in the ultraviolet (UV) are important by construction of optical-to-X-ray SED for 54 AGN, using Far Ultraviolet Spectroscopic Explorer (FUSE) UV and X-ray data from the literature to constrain the disc emission as well as possible. They also found evidence for very significant spread in the bolometric corrections, with no simple dependence on luminosity being evident. Populations of AGN such as narrow-line Seyfert 1 nuclei (Osterbrock & Pogge 1985), radio-loud and X-ray-weak AGN may have bolometric corrections which differ systematically from the rest of the AGN population.

Lusso et al. (2012) obtained accurate estimates of bolometric luminosities, bolometric corrections and Eddington ratios of a large X-ray selected sample of broad-line (Type-1) and narrow-line (Type-2) AGN from the COSMOS (Scoville et al. 2007) XMM–Newton survey for which extensive data from the far-IR to the optical and ultraviolet regimes were available. They assumed that the intrinsic nuclear luminosity is the sum of the IR and X-ray luminosities ($L_{bol} = L_{IR} + L_X$). They used a SED fitting code to disentangle the various contributions (using starburst, AGN and host-galaxy templates) in the observed SED by using a standard χ^2 minimization procedure and they integrated the nuclear component from 1 to 1000 μm to obtain the total IR luminosity L_{IR} . To derive the nuclear accretion disc luminosity from this value, they applied a geometric correction factor based on the models by Pier & Krolik (1992) to account for the torus geometry and their associated anisotropy (see Pozzi et al. 2010). The total X-ray luminosity L_X is estimated by integrating the X-ray SED in the 0.5–100 keV range. They found that the bolometric correction is significantly lower at high luminosities with respect to the previous estimates of Marconi et al. (2004) and Hopkins et al. (2007). The main limitation of the study of Lusso et al. (2012) is that it is en-

tirely based on an X-ray selected sample of AGN, and therefore can be biased towards X-ray bright AGN with most of the sources showing relatively low hydrogen column densities ($N_H \lesssim 10^{23.5} \text{ cm}^{-2}$), thus missing heavily absorbed – Compton thick – nuclei.

Other attempts have been made to derive the AGN bolometric luminosity from optical and IR lines originated in the narrow line regions (NLR) of AGN. Meléndez et al. (2008) have studied the relations of the [OIV]26 μm and [OIII]5007 Å luminosities with the 2–10 keV and 14–195 keV luminosities. They concluded that [OIV] is a good indicator of the AGN power. Rigby et al. (2009) calibrate the [OIV]26 μm line as a measure of AGN intrinsic luminosity. Finally, recently Spinoglio et al. (2022) have computed the AGN bolometric luminosities using the Lusso et al. (2012) bolometric correction and the corrected (2–10) keV luminosities as a function of the luminosities of the three mid-IR high-ionization lines of [OIV]26 μm , [NeV] 14.3 μm , and [NeV]24.3 μm .

Our approach to measure the bolometric luminosity of AGN is different from the other derivations summarized above:

(i) we do not assume an *a priori* template AGN SED as was done in the other derivations (e.g., Marconi et al. 2004; Hopkins et al. 2007), but we have defined ten photometric bands from the radio to the X-rays to cover the SED of AGN of the chosen local AGN sample and we computed the correlations first among the various bands and then, after having integrated a total *bolometric* nuclear luminosity for as many AGN in the sample as possible, we computed the correlations of the various bands, and combinations of them, with the estimated bolometric luminosity;

(ii) with respect to the work of Marconi et al. (2004), we now include sub-arcsecond measurements of the IR bump, which might be *also* due to reprocessed radiation re-radiated by hot dust, because — even if reprocessed — this radiation ultimately originates in the accretion process in the AGN;

(iii) compared to the other works, we separated the nuclear emission, due to the AGN, from the extended emission, due to stellar emission in the galaxy;

(iv) we also use the mid-IR spectroscopy of the lines of [OIV]26 μm and [NeV]14.3 μm and 24.3 μm , which are mainly emitted in the narrow line regions excited by the accreting SMBH.

(v) our sample includes only local AGN, avoiding possible cosmic evolution in the bolometric corrections derived when different samples obtained at different redshift intervals are combined.

2. SAMPLE OF LOCAL ACTIVE GALACTIC NUCLEI AND MULTIFREQUENCY DATASET

The sample of local AGN used to compute the bolometric luminosity is the 12 μm AGN sample (hereafter 12MAGN), originally selected from the IRAS catalog from Spinoglio & Malkan (1989) and updated in Rush et al. (1993). The chosen sample is essentially a bolometric flux-limited survey outside the galactic plane, and therefore largely unbiased, given the empirical fact that galaxies emit an approximately constant fraction of their total bolometric luminosity at 12 μm . This fraction is $\sim 15\%$ for AGN, including Seyfert type 1, type 2 and quasars (Spinoglio & Malkan 1989), and 7% for normal and starburst galaxies, independent of star formation activity (Spinoglio et al. 1995). The sample is given in Table 1 and it is the same as the one used in Spinoglio et al. (2022). This sample has been selected from the 12 μm flux-limited survey of 893 galaxies (Rush et al. 1993) extracted from the IRAS Faint Source Catalog, Version 2 (FSC-2; Moshir & et al. 1990) with the classification of galaxy nuclear activity with catalogs of active galaxies available at the time of the selection (Veron-Cetty & Veron 1991; Hewitt & Burbidge 1991; Helou et al. 1991). It contains in total 117 AGN, divided into 48 Seyfert type 1, 27 Hidden Broad Line galaxies (hereafter HBL), 30 Seyfert type 2 and 10 Low Ionization Emission Line galaxies (hereafter LINER) and two other galaxies, one classified as “non-Seyfert” (NGC 1056) and one as a starburst galaxy (NGC 6810). We have adopted here the class of HBL galaxies because they are indistinguishable in their IR properties from the Seyfert type 1 galaxies, and therefore belong to the broader class of type 1 AGN (see, e.g. Tommasin et al. 2010). The 10 radio-loud objects in the sample are flagged in Table 1. The average redshift(s) and dispersion(s) for the whole sample is $\langle z \rangle = 0.025 \pm 0.029$, while for the four classes of galaxies considered are: for Sy1: $\langle z \rangle = 0.032 \pm 0.039$, for HBL: $\langle z \rangle = 0.023 \pm 0.019$, for Sy2: $\langle z \rangle = 0.019 \pm 0.016$ and for LIN: $\langle z \rangle = 0.016 \pm 0.021$.

To compute the bolometric luminosity of local AGN, we have considered the following photometric bands, from low to high frequencies: radio 8.4 GHz, mid-IR 12 μm , 7 μm , 5.8 μm and 4.5 μm bands, near-IR 2.2 μm , the near ultraviolet (NUV) Galaxy Evolution Explorer (GALEX, Morrissey et al. 2007) band at an effective wavelength of 2316 Å and the far ultraviolet (FUV) GALEX band at 1539 Å, and the 2–10 keV and 14–195 keV hard X-ray bands.

Our main concern in this analysis has been to derive, from the available observations, the *nuclear* fluxes of the AGN of our sample, because many local AGN are *contaminated* by the galactic component, which at some frequencies can be dominant. In order to isolate the nuclear emission from the total observed emission in the various mid-IR bands that we have considered, we have used the sub-arcsecond observations at 12 μm to correct the other observations and we have corrected the near-IR K-band observations as well as the ultraviolet fluxes. However, the 8.4 GHz flux densities are al-

ready detecting the nuclei at sub-arcsecond resolution and the hard X-ray emission is intrinsically produced mainly by the AGN.

From the low frequency data (radio) to the high energy data (X-rays), we have adopted the following methodology:

(i): the radio data at 8.4 GHz have been taken from the VLA (Thompson et al. 1980) with a resolution of $0''.25$ (Thean et al. 2000) and therefore are sampling the nuclear emission; at the average distance of the whole AGN sample, the angular distance of $0''.25$ corresponds to a linear distance of 134 pc, while at the average distance of Seyfert 1 to 142 pc, at the average distance of Seyfert 2 to 102 pc and at the average distance of LINER to 86 pc, thus confirming that the radio VLA observations are mainly sampling the nuclear emission; the presence of a jet core in the data would in any case be due to the AGN;

(ii): the $12\ \mu\text{m}$ continuum flux density has been taken from VLT-VISIR (Lagage et al. 2004) sub-arcsecond resolution observations (Asmus et al. 2014); when these observations were not available, we used the small aperture $\sim 10\ \mu\text{m}$ observations from Gorjian et al. (2004) and in only two cases from Rieke (1978) (see Table 2);

(iii): the $7\ \mu\text{m}$ and $12.8\ \mu\text{m}$ continuum fluxes have been derived using *Spitzer*-IRS (Houck et al. 2004) spectroscopy of the [ArII] $7.0\ \mu\text{m}$ line and of the [NeII] $12.8\ \mu\text{m}$ line, respectively, using the line intensities together with the measured equivalent widths from Gallimore et al. (2010), these data include galactic emission and therefore need to be corrected;

(iv): the *Spitzer*-IRS data at $7\ \mu\text{m}$, and the *Spitzer*-IRAC (Fazio et al. 2004) data at $5.8\ \mu\text{m}$ and $4.5\ \mu\text{m}$ have been corrected using the observed ratio of the *Spitzer*-IRS $12.8\ \mu\text{m}$ continuum to the VLT-VISIR $12\ \mu\text{m}$ sub-arcsecond continuum flux density (or the small aperture $\sim 10\ \mu\text{m}$ flux density, see the above point ii);

(v): the K-band nuclear flux has been derived from Keck and 2MASS observations as reported and fully explained in Spinoglio et al. (2022);

(vi): the GALEX near-ultraviolet (NUV) and far-ultraviolet (FUV) fluxes have been derived using the GALEX point spread functions of the two UV bands, following the work of Morrissey et al. (2007);

(vii): the 2-10 keV and 14-195 keV hard X-ray data are nuclear and emitted by large by the AGN, so we assume that they do not need to be corrected. The compilation for the $12\ \mu\text{m}$ sample has been taken from Spinoglio et al. (2022)

Table 1. The AGN sample: coordinates, redshift, types and radio loudness.

n.	Name	RA (J2000.0)	dec (J2000.0)	z	Type	Radio
(1)	(2)	(3)	(4)	(5)	(6)	(6)
1	MRK0335	00:06:19.5	+20:12:10	0.0258	Sy1	
2	NGC34=Mrk938=N17	00:11:06.5	-12:06:26	0.0196	Sy2	
3	IRASF00198-7926	00:21:57.0	-79:10:14	0.0728	Sy2	
4	ESO012-G021	00:40:47.8	-79:14:27	0.0300	Sy1	
5	NGC0262=MRK348	00:48:47.1	+31:57:25	0.0150	HBL	RL

Notes: (This table is available in its entirety in machine-readable form). The columns give for each AGN in the sample: (1) name; (2) Right Ascension (J2000.0); (3) declination (J2000.0); (4) redshift from NED; (5) AGN type: Sy1 = Seyfert type 1; Sy2 = Seyfert type 2; HBL = Hidden Broad Line Region AGN; LIN = LINER galaxy; (6) Radio loudness (flagged as RL): an AGN is considered radio loud if the radio flux is larger than ten times the B-band optical flux (Kellermann et al. 1989) ($F(5\text{GHz}) \geq 10 \times F_{B\text{-band}}$).

and the observations have been reported in Ricci et al. (2017) and Oh et al. (2018).

2.1. Deriving the nuclear fluxes for the mid-IR and UV bands

To build up the AGN bolometric luminosity, we have compiled, for our sample of galaxies, in Table 2 the low-frequency (from radio to near-IR) nuclear fluxes and in Table 3 the high-frequency (from UV to X-rays) nuclear fluxes. In Table 2 we give, for each galaxy of the 12MAGN sample observed, the 8.4 GHz radio flux, measured with the VLA (Thean et al. 2000) with a $0''.25$ effective aperture, the $12\ \mu\text{m}$ nuclear flux density measured with the VLT-VISIR in most cases (Asmus et al. 2014) (where these data were not available, we have used the $10\ \mu\text{m}$ small aperture flux taken from Gorjian et al. (2004); Rieke (1978) and inserted a note in Table 2).

We have then extracted from the fluxes and equivalent width measurements of the two fine structure lines of [ArII] $7.0\ \mu\text{m}$ and [NeII] $12.8\ \mu\text{m}$ from Gallimore et al. (2010), who made systematic *Spitzer* observations of the 12MAGN sample, the corresponding flux densities of the continuum at $7.0\ \mu\text{m}$ and $12.8\ \mu\text{m}$. The spectral information was extracted from synthetic, $20''$ diameter circular apertures centered on the brightest, compact IR source, and therefore the derived continuum flux densities are relative to the extended $20''$ emission. In order to remove the extended emission and obtain nuclear flux densities, we have computed the ratio of the $12.8\ \mu\text{m}$ $20''$ diameter flux density from *Spitzer*-IRS to the nuclear $12\ \mu\text{m}$ flux density measured by VLT-VISIR (Asmus et al. 2014). We ignored the small difference in wavelength between the two observations. Using the same ratio, R12 in Table 2, we have corrected the $4.5\ \mu\text{m}$ and $5.8\ \mu\text{m}$ flux densities from *Spitzer*-IRAC, measured by Gallimore et al. (2010) using a synthetic, $20''$ diameter cir-

Table 2. Low frequency nuclear photometry of the AGN sample.

n. Name	Redshift	Type	F(8.4GHz)	F(12 μ m)	F(12 μ m)	R12	F(7.0 μ m)	F(5.8 μ m)	F(4.5 μ m)	F(K)
			VLA	VLT	IRS	IRS/VLT	IRSCOR	IRSCOR	IRSCOR	Keck/2MASS
(1)	(2)	(3)	(4)	(5)	(6)	(7)	(8)	(9)	(10)	(11)
1 MRK0335	0.0258	Sy1	2.1	151.†	190.52	1.26	100.32	77.91	67.53	16.00
2 NGC34=Mrk938=N17	0.0196	Sy2	14.5	57.8	210.38	3.64	—	—	—	5.25
3 IRASF00198-7926	0.0728	Sy2	—	—	—	—	—	—	—	2.15
4 ESO012-G021	0.0300	Sy1	—	—	115.67	—	—	—	—	5.10
5 NGC0262=MRK348	0.0150	HBL	346.0	117.	304.83	2.61	47.89	37.73	28.48	2.17

Notes: (This table is available in its entirety in machine-readable form).

The columns give for each AGN in the sample: (1) name; (2) redshift from NED; (3) AGN type; Sy1 = Seyfert type 1; Sy2 = Seyfert type 2; HBL = Hidden Broad Line Region AGN; LIN = LINER galaxy; (4) 8.4GHz nuclear flux density (Thean et al. 2000); (5) VLT-VISIR subarcsecond nuclear 12 μ m flux density from Asmus et al. (2014), where not available the small aperture 10 μ m flux density has been taken from Gorjian et al. (2004); Rieke (1978); (6) *Spitzer*-IRS 12 μ m continuum flux density as derived from Gallimore et al. (2010), using the [NeII]12.8 μ m line flux and the corresponding equivalent width; (7) R12 is the ratio between the *Spitzer*-IRS continuum and the VLT-VISIR subarcsecond flux density at 12 μ m; (8) *Spitzer*-IRS 7 μ m continuum flux density as derived from Gallimore et al. (2010), using the [ArII]7.0 μ m line flux and the corresponding equivalent width corrected for R12; (9) *Spitzer*-IRAC 5.8 μ m flux density corrected for R12; (10) *Spitzer*-IRAC 4.5 μ m flux density corrected for R12. This table is available in its entirety in machine-readable form. †: the 10.8 μ m flux density is from Gorjian et al. (2004).

cular aperture centered on the brightest infrared source associated with the active galaxy. We have also corrected the 7.0 μ m continuum derived from the *Spitzer*-IRS observations of the [ArII]7.0 μ m line, as described above. We have included in Table 2 the corrected 7.0 μ m, 5.8 μ m and 4.5 μ m flux densities only for objects for which the R12 ratio is less than 3 (R12 < 3), discarding all objects for which this ratio is greater than this threshold. This latter has been chosen because we have estimated reasonable a correction only below this threshold. The number of objects above this threshold (with R12 > 3) is 14 plus two galaxies with upper limits in the VLT-VISIR data (see Table 2).

The near-IR *nuclear* K-band flux density has been derived in Spinoglio et al. (2022) and we refer to this work for the details.

The high-frequency (from UV to X-rays) nuclear flux densities reported in Table 3 include the NUV and FUV ultraviolet flux densities derived from GALEX observations and the 2-10 keV and 14-195 keV band hard X-ray fluxes, together with the photon indexes Γ_1 and Γ_2 relative to the 2-10 keV and 14-195 keV observations, respectively. The Galaxy Evolution Explorer (GALEX) (Morrissey et al. 2007) data have been extracted from the Mikulski Archive for Space Telescopes (MAST, Conti et al. 2011) GALEX Catalog Search¹.

For each AGN in our sample, we have extracted the NUV and FUV fluxes and errors in the 4 smallest apertures and the given values of the galactic interstellar reddening E(B-V). The GALEX absolute calibration and extinction coefficients have been taken from Morrissey et al. (2007) and Wall et al. (2019), respectively. In order to obtain the best approximation of the *nuclear* UV fluxes, we have used the fluxes from

APER_1 to APER_3, corresponding to radii of 1''.5 to 3''.8. For the 23 AGN for which upper limits were present in the APER_1 FUV flux, we have taken the APER_2 flux, for the 9 AGN for which also the APER_2 flux was an upper limit, we have taken the APER_3 flux, while when also this flux was an upper limit we have given an upper limit to the FUV flux. The APER_n (with n=1-3) fluxes have then been corrected using the GALEX photometric *curve of growth* published in Morrissey et al. (2007), to derive the nuclear fluxes.

The 2-10 keV X-ray fluxes, corrected for absorption, and the 14-195 keV band hard X-ray fluxes have been taken from the references given in Table 3. Because these fluxes are intrinsically produced by the AGN, no further correction should be needed.

2.2. Building the bolometric luminosity from the available nuclear luminosities

Once the nuclear fluxes were computed, we have used trapezoidal integration to calculate the total, or *bolometric*, luminosity for our AGN sample. The integration has been performed in two separate spectral regions: the first interval is from the radio (8.4 GHz band) to the FUV band, while the second interval includes only the two X-ray bands (2-10 keV and the 14-195 keV). For those AGN where only one X-ray band flux was available, we computed the missing flux using the median spectral index between 2-10 keV and the 14-195 keV for each of the four AGN classes. The resulting bolometric luminosity is simply the sum of these two integrations. No interpolation has been included between the UV and X-rays data, because this spectral region is not observable and a power-law interpolation would likely have overestimated the bolometric luminosity.

To assign a bolometric luminosity to an AGN of our sample we require a minimum number of detections over the ten

¹ <http://galex.stsci.edu/GR6/?page=mastform>

Table 3. High frequency nuclear photometry of the AGN sample and derived bolometric fluxes and luminosities.

n. Name	z	Type	F_{NUV}	F_{FUV}	$F_{2-10keV}$	$F_{14-195keV}$	F_{bol}	L_{bol}	Γ_1	Γ_2	Ref ₁	Ref ₂	Flag
(1)	(2)	(3)	(4)	(5)	(6)	(7)	(8)	(9)	(10)	(11)	(12)	(13)	(14)
1 MRK0335	0.0258	Sy1	3.517	1.880	16.69	15.97	402.72	44.751	2.03	2.31	(1)	(32)	
2 NGC34=Mrk938=N17	0.0196	Sy2	0.072	0.246	2.35	—	105.68	43.927	1.9	—	(2)		
3 IRASF00198-7926	0.0728	Sy2	—	0.133	—	21.80	148.25	45.248	—	—		(33)	
4 ESO012-G021	0.0300	Sy1	—	—	5.51	4.00	47.86	43.959	1.21	—	(3)	(34)	
5 NGC0262=MRK348	0.0150	HBL	0.089	0.143	37.45	144.81	642.69	44.475	1.68	1.90	(1)	(32)	

Notes. The columns give for each AGN in the sample: (1) name; (2) AGN type: Sy1 = Seyfert type 1; Sy2 = Seyfert type 2; HBL = Hidden Broad Line Region AGN; LIN = LINER galaxy; (3) redshift; (4) Near-ultraviolet flux (NUV) from the Mikulski Archive for Space Telescopes (MAST, Conti et al. 2011) GALEX Catalog Search; (5) Far-ultraviolet flux (FUV) from the Mikulski Archive for Space Telescopes (MAST, Conti et al. 2011) GALEX Catalog Search; (6) 2-10 keV absorption corrected X-ray flux from the references of column (10); (7) 14-195 keV observed X-ray flux from the references of column (11); (8) Computed bolometric flux (see text); (9) Logarithm of the total (bolometric) luminosity; (10) photon index of the 2-10 keV observations Γ_1 , from either Brightman & Nandra (2011) or Ricci et al. (2017); (11) photon index of the 14-195 keV observations Γ_2 , from Oh et al. (2018); (12) reference of the 2-10keV flux, Ref₁: (1): derived from the absorption corrected luminosity of Brightman & Nandra (2011), (2): derived from the absorption corrected luminosity of Guainazzi et al. (2005), (3): Ghosh & Soundararajaperumal (1992), (4): Reeves & Turner (2000), (5): derived from the absorption corrected luminosity of Tan et al. (2012), (6): Ricci et al. (2017), (7): derived from the absorption corrected luminosity of Marinucci et al. (2012), (8): Bi et al. (2020), (9): derived from the absorption corrected luminosity of Iyomoto et al. (1996), (10): derived from the absorption corrected luminosity of Saade et al. (2022), (11): derived from the absorption corrected luminosity of Levenson et al. (2009), (12): Rivers et al. (2013), (13): Walton et al. (2021), (14): Bassani et al. (1999), (15): Tanimoto et al. (2022), (16): Della Ceca et al. (2008), (17): Iyomoto et al. (2001), (18): Boissay et al. (2016), (19): Brightman & Nandra (2008), (20): derived from the absorption corrected luminosity of Akylas & Georgantopoulos (2009), (21): Chen et al. (2022), (22): derived from the absorption corrected luminosity of Zhou & Zhang (2010), (23): Vasylenko (2018), (24): derived from the absorption corrected luminosity of Yamada et al. (2023), (25): Lutz et al. (2004), (26): Osorio-Clavijo et al. (2022), (27): Cardamone et al. (2007), (28): Osorio-Clavijo et al. (2023), (29): Corral et al. (2014), (30): Braito et al. (2009), (31): Zhou & Zhang (2010); (13) reference of the 14-195keV flux, Ref₂: (32): Oh et al. (2018), (33): Deluit (2004), (34): Cusumano et al. (2010); (14) Bolometric flux/luminosity flag: L = lower limit to the bolometric flux and luminosity; N = data not available for a proper integration of bolometric flux and luminosity.

photometric bands considered. We require at least 3 available detections in three bands and that these must include either the 2-10 keV or the 14-195 keV X-ray band. When no X-ray data were available, we were nevertheless able to assign a lower limit to the bolometric flux and luminosity, because the low frequency domain, from the radio to the K-band, is carrying a substantial part of the total luminosity, as can be seen from the shape of the SEDs (see Figs. 12 - 15).

The derived bolometric luminosities and bolometric fluxes for our sample are given in Table 3. For 18 objects we have assigned lower limits to the bolometric flux and luminosity, namely ESO 541-IG012, MRK 1034NED02, NGC 1056, NGC 1241, IRASF 03362-1642, IRASF 0345+0055, ESO 253-G003, IRASF 07599+6508, IRASF 08752+3915, MCG +00-29-023, NGC 4602, MRK 0231, NGC 4922, NGC 5005, NGC 5953, ARP 220, MKR 0897, NGC 7496 and CGCG 381-051. For only two objects we were not able to assign even a lower limit to the bolometric luminosity and flux, namely NGC 1056 and NGC 3511, because of the lack of observations both in the mid-IR (only IRS large aperture data are available) and at X-rays.

3. RESULTS

3.1. Monochromatic luminosities

We have selected three observables as the best AGN bolometric luminosity indicators: the corrected 2-10 keV hard X-ray luminosity, the nuclear 12 μm luminosity, and the luminosity of the [OIV] 26 μm line. These three physical quantities have been chosen because: (i) X-ray emission is ubiqui-

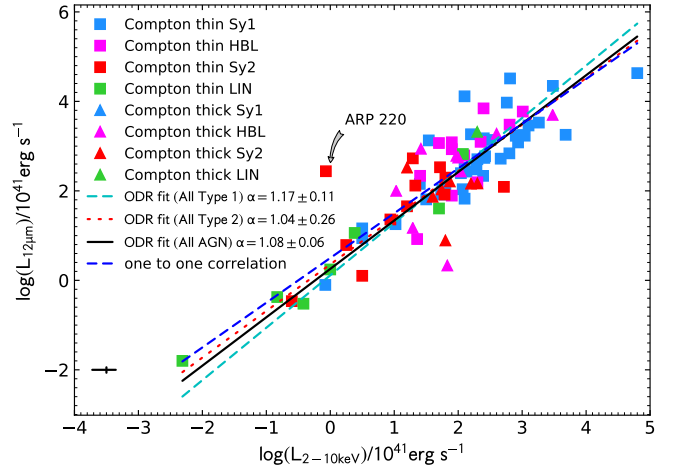


Figure 1. Nuclear 12 μm luminosity as a function of the corrected 2-10 keV luminosity. The position of the outlier ARP 220 has been indicated. In each figure representing the correlations between physical quantities, the error bar at the lower left corner has been computed using the median value of the relative errors of the plotted data (from Fig. 1 to Fig. 11 and from Fig. 17 to Fig. 20).

tous in AGN and is believed to be produced by comptonization of UV/optical disc photons by a corona of hot electrons located near the black hole; (ii) the mid-IR, and in particular the nuclear 12 μm emission, is the spectral region which has been found to have the minimum scatter in the ratio of the observed to total luminosity among various types of AGN (Spinoglio & Malkan 1989) and therefore the mid-IR flux is considered one of the best general indicators of the bolometric luminosity of all types of AGN; (iii) the [OIV] 26 μm line

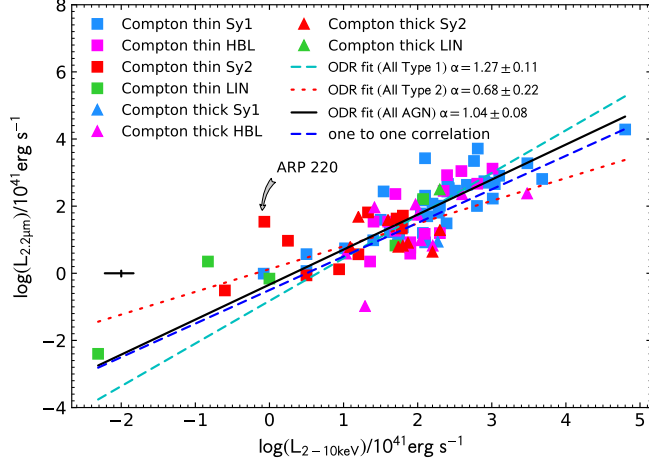


Figure 2. Nuclear K-band luminosity as a function of the corrected 2-10 keV luminosity. The position of the outlier ARP 220 has been indicated.

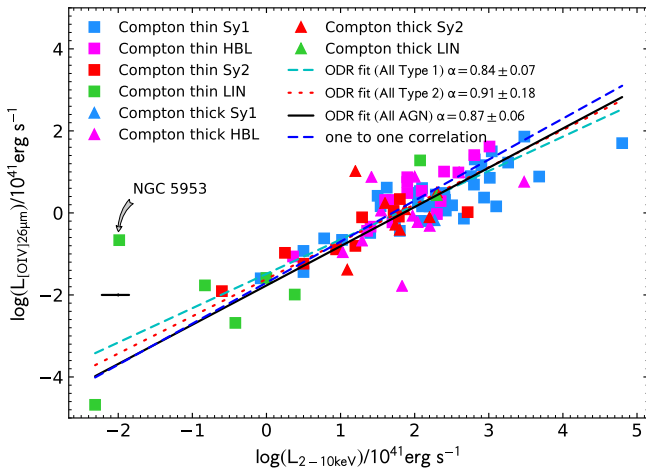


Figure 3. [OIV]26 μm line luminosity as a function of the corrected 2-10 keV luminosity. The position of the outlier NGC 5953, which has been recently classified as a non-AGN (Osorio-Clavijo et al. 2023), has been indicated.

emission, is mainly produced in the AGN narrow line regions (NLR) and therefore it is indirectly linked to the accretion power of the AGN: it is a good measure of the AGN bolometric luminosity, as recently demonstrated by, e.g., Spinoglio et al. (2022). Shorter wavelengths, from the soft X-rays through the optical, can suffer from large extinctions, which are difficult to determine.

To quantify the statistical significance of the relations that we present in the following sections, we used an orthogonal distance regression (ODR) fit (see, e.g., Spinoglio et al. 2022). The best empirical correlations that we have found with the corrected 2-10 keV hard X-ray luminosity are the nuclear 12 μm luminosity (Fig. 1), the nuclear K-band luminosity (Fig. 2) and the [OIV] 26 μm line luminosity (Fig. 3). The statistics of these correlations are given in Table 4, bro-

ken out for each of the subsets of data, i.e. the whole 12 μm AGN sample for which are available these observations, the Type 1 objects, which include both Seyfert type 1's and the so-called *hidden broad-line* AGN (HBL) and the Type 2 objects, i.e. the *pure* Seyfert type 2 galaxies: the number of objects (N), the Pearson correlation coefficient ρ , the null hypothesis probability, the linear regression fit parameters (α and β) and the residual variance σ , measuring the goodness of the fit. The linear equation is defined in the notes of Table 4.

3.2. Monochromatic vs. bolometric luminosities

Having obtained the bolometric luminosities for most (82.9%) of our AGN sample (excluding the lower limits and the two objects with no determination), which are given in the last data column of Table 3, we computed the correlations between 12 μm nuclear luminosity, K-band nuclear luminosity, NUV corrected luminosity, FUV corrected luminosity, 8.4GHz luminosity, 2-10 keV luminosity and 15-145 keV luminosity and the computed bolometric luminosity. We have also computed the correlations of the luminosities of the three mid-IR fine structure lines, which are mainly originated in the AGN narrow line regions, namely [OIV]26 μm , [NeV]14.3 μm and [NeV]24.3 μm with the bolometric luminosities. All correlations are given in Table 5 and are shown in Figs. 4 – 9.

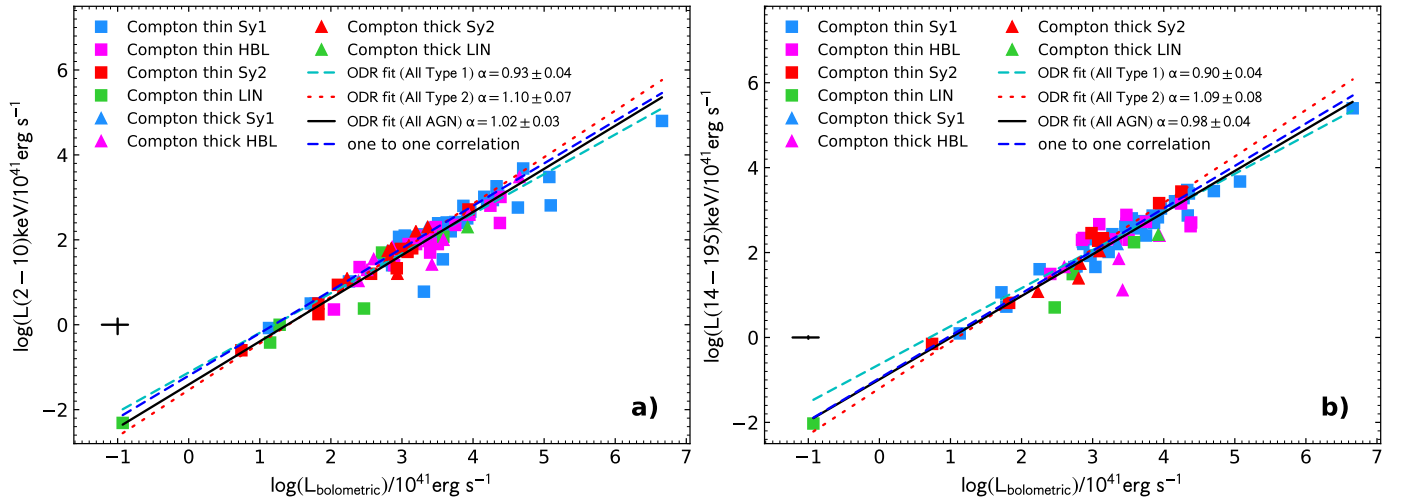
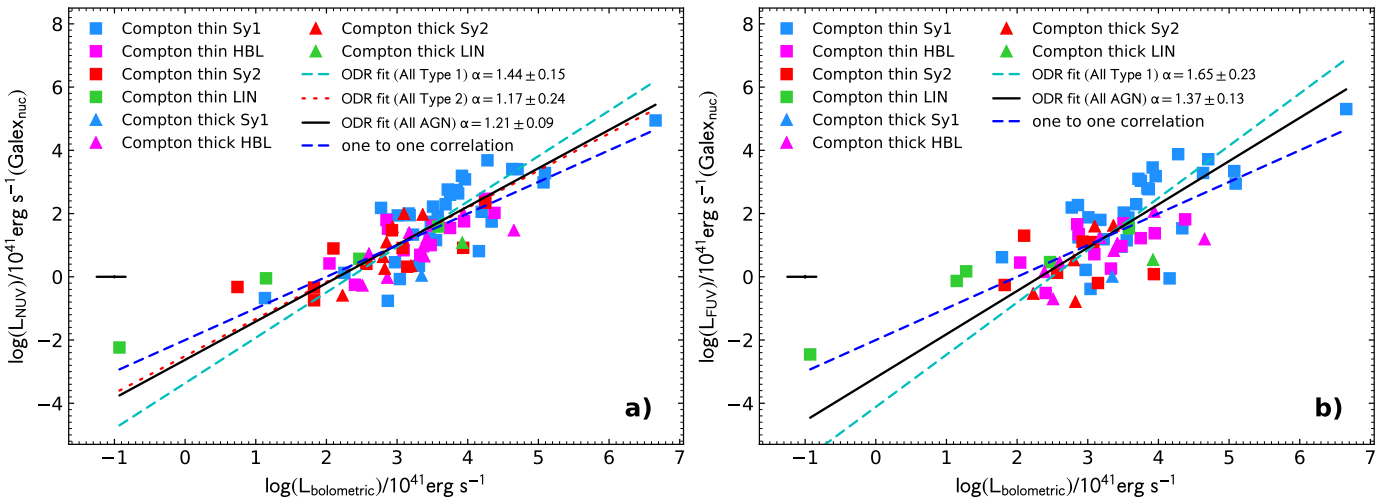
In Fig. 4a the well known correlation between the 2-10 keV *absorption-corrected* luminosity and the computed bolometric luminosity is shown: including all classes of AGN the correlation is linear (slope 1.00 ± 0.04) and becomes slightly flatter for the type 1 AGN (slope ~ 0.90) and slightly steeper for the type 2 AGN (slope ~ 1.04), while remaining linear within 2σ . The harder X-ray 14-195 keV (Fig.4b) observed luminosity has also a good and almost linear (slope 0.94 ± 0.04) correlation with the bolometric luminosity if all classes are included, while it becomes significantly steeper for type 2 objects only.

In Fig. 5a and b are shown the correlations between the NUV and FUV corrected luminosities with the bolometric luminosity, respectively. The NUV luminosity for all classes together correlates almost linearly (within 2σ) with the bolometric luminosity, while the correlation becomes steeper for the type 1 class ($\alpha \sim 1.40$), showing that type 1 objects have a stronger UV-excess at higher luminosities. For the same reason, the FUV luminosity has a correlation steeper than linear with the bolometric luminosity. The slope is ~ 1.3 for the whole sample and ~ 1.6 for type 1 AGN only, while no correlation is apparent for the type 2 AGN. This is partly due to the increased contribution of the accretion disk energy in the UV for the more luminous AGN (Sun & Malkan 1989). Moreover, in these two plots, most AGN at bolometric lumi-

Table 4. Correlation of various luminosities with the best bolometric indicators (2-10 keV, nuclear $12\mu\text{m}$ and [OIV] $26\mu\text{m}$ line luminosities).

Considered variables (1)	Subset (2)	N (3)	ρ (P_{null}) (4)	$\beta \pm \Delta\beta$ (5)	$\alpha \pm \Delta\alpha$ (6)	σ (7)
$L_{12\mu\text{m}}^{\text{nuc}}$ vs. $L_{2-10\text{keV}}$	All	87	0.85 (3.3×10^{-25})	0.33 ± 0.14	1.08 ± 0.07	0.203
" " "	Type 1	49	0.82 (4.4×10^{-13})	0.11 ± 0.25	1.17 ± 0.11	0.145
" " "	Type 2	19	0.58 (8.4×10^{-3})	0.36 ± 0.39	1.04 ± 0.26	0.316
L_K^{nuc} vs. $L_{2-10\text{keV}}$	All	90	0.79 (1.7×10^{-20})	-0.34 ± 0.16	1.04 ± 0.08	0.242
" " "	Type 1	55	0.81 (6.8×10^{-14})	-0.82 ± 0.26	1.27 ± 0.11	0.145
" " "	Type 2	18	0.45 (5.9×10^{-2})	0.12 ± 0.31	0.68 ± 0.22	0.296
$L_{[\text{OIV}]26\mu\text{m}}$ vs. $L_{2-10\text{keV}}$	all	96	0.83 (5.0×10^{-25})	-1.56 ± 0.12	0.87 ± 0.06	0.202
" " "	Type 1	57	0.83 (1.0×10^{-15})	-1.49 ± 0.16	0.84 ± 0.07	0.105
" " "	Type 2	18	0.73 (5.9×10^{-4})	-1.61 ± 0.28	0.91 ± 0.18	0.167

Notes. Fit results. The columns give for each correlation: (1) variables; (2) Subset of the sample on which the fit was computed: "all" indicates the entire sample and Type 1 and Type 2 the Seyfert type subsets; (3) Number of sources; (4) Pearson correlation coefficient ρ (1: completely correlated variables, 0: uncorrelated variables) with the relative null hypothesis (zero correlation) probability; (5) and (6): Parameters of the linear regression fit using the equation: $\log(L_y) = \beta + \alpha \times \log(L_x)$; (7): residual variance of the fit σ .

**Figure 4.** (a): Corrected 2-10 keV luminosity versus bolometric luminosity. (b): 14-195 keV luminosity versus bolometric luminosity.**Figure 5.** (a): GALEX NUV luminosity versus bolometric luminosity. (b): GALEX FUV luminosity versus bolometric luminosity.

nosities greater than $\sim 10^{45}\text{erg s}^{-1}$ are Seyfert type 1, known to have more powerful directly observed accretion disks.

Figure 6a shows the correlation between the radio 8.4 GHz luminosity and the bolometric luminosity, respectively. The

Table 5. Logarithmic correlations of various continuum and line luminosities and their combinations with the bolometric luminosities.

Considered variables (1)	Subset (2)	N (3)	ρ (P_{null}) (4)	$\beta \pm \Delta\beta$ (5)	$\alpha \pm \Delta\alpha$ (6)	σ (7)
$L_{2-10\text{keV}}$ vs. L_{bol}	all	95	0.95 (3.2×10^{-49})	-1.41 ± 0.11	1.02 ± 0.03	0.052
" " "	Type 1	57	0.94 (4.8×10^{-27})	-1.12 ± 0.16	0.93 ± 0.04	0.048
" " "	Type 2	18	0.97 (4.8×10^{-11})	-1.54 ± 0.19	1.10 ± 0.07	0.019
$L_{14-195\text{keV}}$ vs. L_{bol}	all	68	0.95 (1.6×10^{-34})	-0.99 ± 0.14	0.98 ± 0.04	0.057
" " "	Type 1	47	0.95 (8.8×10^{-25})	-0.63 ± 0.15	0.90 ± 0.04	0.037
" " "	Type 2	11	0.98 (3.1×10^{-7})	-1.20 ± 0.24	1.10 ± 0.08	0.027
L_{NUV} vs. L_{bol}	all	79	0.81 (2.0×10^{-19})	-2.63 ± 0.30	1.21 ± 0.09	0.245
" " "	Type 1	45	0.79 (9.7×10^{-11})	-3.36 ± 0.55	1.44 ± 0.15	0.221
" " "	Type 2	18	0.71 (8.5×10^{-4})	-2.51 ± 0.68	1.17 ± 0.24	0.221
L_{FUV} vs. L_{bol}	all	67	0.75 (3.0×10^{-13})	-3.19 ± 0.44	1.37 ± 0.13	0.354
" " "	Type 1	39	0.71 (4.0×10^{-7})	-4.12 ± 0.85	1.65 ± 0.23	0.311
" " "	Type 2	12	0.24 (4.4×10^{-1})	undefined	undefined	0.334
$L_{8.4\text{GHz}}^{\text{nuc}}$ vs. L_{bol}	all	80	0.76 (1.5×10^{-16})	-7.13 ± 0.40	1.41 ± 0.12	0.324
" " "	Type 1	48	0.81 (1.9×10^{-12})	-8.39 ± 0.60	1.70 ± 0.16	0.227
" " "	Type 2	14	0.77 (1.3×10^{-3})	-7.34 ± 0.92	1.55 ± 0.33	0.181
L_K^{nuc} vs. L_{bol}	All	88	0.90 (5.8×10^{-33})	-1.86 ± 0.18	1.06 ± 0.05	0.110
" " "	Type 1	54	0.90 (3.1×10^{-20})	-1.81 ± 0.25	1.06 ± 0.07	0.089
" " "	Type 2	18	0.82 (2.4×10^{-5})	-1.65 ± 0.43	0.99 ± 0.15	0.106
$L_{12\mu\text{m}}^{\text{nuc}}$ vs. L_{bol}	All	83	0.94 (1.7×10^{-39})	-1.24 ± 0.14	1.09 ± 0.04	0.076
" " "	Type 1	48	0.94 (9.7×10^{-23})	-0.91 ± 0.20	1.01 ± 0.05	0.057
" " "	Type 2	17	0.87 (7.1×10^{-6})	-1.57 ± 0.46	1.19 ± 0.16	0.089
$L_{[\text{OIV}]26\mu\text{m}}$ vs. L_{bol}	all	94	0.87 (8.3×10^{-30})	-3.15 ± 0.18	0.99 ± 0.05	0.140
" " "	Type 1	57	0.83 (1.4×10^{-15})	-2.40 ± 0.23	0.78 ± 0.06	0.112
" " "	Type 2	18	0.87 (3.2×10^{-6})	-3.23 ± 0.41	1.08 ± 0.14	0.099
$L_{[\text{NeV}]14.3\mu\text{m}}$ vs. L_{bol}	all	84	0.85 (2.1×10^{-24})	-3.53 ± 0.20	0.95 ± 0.06	0.110
" " "	Type 1	54	0.85 (7.8×10^{-16})	-3.33 ± 0.25	0.88 ± 0.07	0.114
" " "	Type 2	16	0.89 (3.8×10^{-6})	-3.65 ± 0.38	1.01 ± 0.13	0.078
$L_{[\text{NeV}]24.3\mu\text{m}}$ vs. L_{bol}	all	73	0.79 (1.1×10^{-16})	-3.42 ± 0.26	0.93 ± 0.08	0.119
" " "	Type 1	46	0.83 (8.2×10^{-13})	-2.90 ± 0.26	0.78 ± 0.07	0.097
" " "	Type 2	15	0.80 (3.2×10^{-4})	-4.03 ± 0.65	1.17 ± 0.21	0.087
$L_{[\text{OIII}]5007\text{Å}}$ vs. L_{bol}	all	87	0.83 (1.4×10^{-23})	-3.76 ± 0.25	1.14 ± 0.07	0.142
" " "	Type 1	53	0.83 (1.1×10^{-14})	-3.27 ± 0.30	1.00 ± 0.08	0.116
" " "	Type 2	18	0.65 (3.3×10^{-3})	-4.46 ± 0.89	1.32 ± 0.31	0.260
$7.0 \times L_{12\mu\text{m}}^{\text{nuc}} + 389 \times L_{[\text{OIV}]26\mu\text{m}}$ vs. L_{bol}	all	81	0.94 (2.0×10^{-39})	-0.05 ± 0.14	1.04 ± 0.04	0.070
" " "	Type 1	48	0.94 (8.4×10^{-24})	0.37 ± 0.17	0.93 ± 0.05	0.047
" " "	Type 2	16	0.88 (7.9×10^{-6})	-0.06 ± 0.40	1.04 ± 0.14	0.078
$5.4 \times L_{12\mu\text{m}}^{\text{nuc}} + 2132 \times L_{[\text{NeV}]14.3\mu\text{m}}$ vs. L_{bol}	all	63	0.87 (2.7×10^{-20})	0.14 ± 0.23	0.98 ± 0.07	0.080
" " "	Type 1	39	0.92 (2.8×10^{-16})	0.67 ± 0.21	0.84 ± 0.06	0.051
" " "	Type 2	14	0.70 (5.1×10^{-3})	0.08 ± 0.71	0.99 ± 0.24	0.085
$17.3 \times L_K^{\text{nuc}} + 881 \times L_{[\text{OIII}]5007\text{Å}}$ vs. L_{bol}	all	79	0.94 (9.3×10^{-37})	0.00 ± 0.14	1.01 ± 0.04	0.047
" " "	Type 1	50	0.93 (5.0×10^{-23})	0.11 ± 0.19	0.99 ± 0.05	0.044
" " "	Type 2	17	0.92 (1.5×10^{-7})	0.41 ± 0.25	0.83 ± 0.09	0.039

Notes. Fit results. The columns give for each correlation: (1) variables; (2) Subset of the sample on which the fit was computed: "all" indicates the entire sample and Type 1 and Type 2 the Seyfert type subsets; (3) Number of sources; (4) Pearson correlation coefficient ρ (1: completely correlated variables, 0: uncorrelated variables) with the relative null hypothesis (zero correlation) probability; (5) and (6): Parameters of the linear regression fit using the equation: $\log(L_y) = \beta + \alpha \times \log(L_x)$; (7): residual variance of the fit σ .

8.4 GHz luminosity has always a steeper than linear correlation with the bolometric luminosity, and its slope increases from the whole sample through type 1 AGN to type 2 objects, showing that at higher luminosities radio loudness is increasing.

The nuclear K-band luminosity (Fig. 6b) has a very good linear correlation with the bolometric luminosity, for all types of objects (slope $\sim 1.04 \pm 0.05$). Therefore the nuclear K-band flux, once corrected for starlight emission, is a good indicator for the bolometric flux.

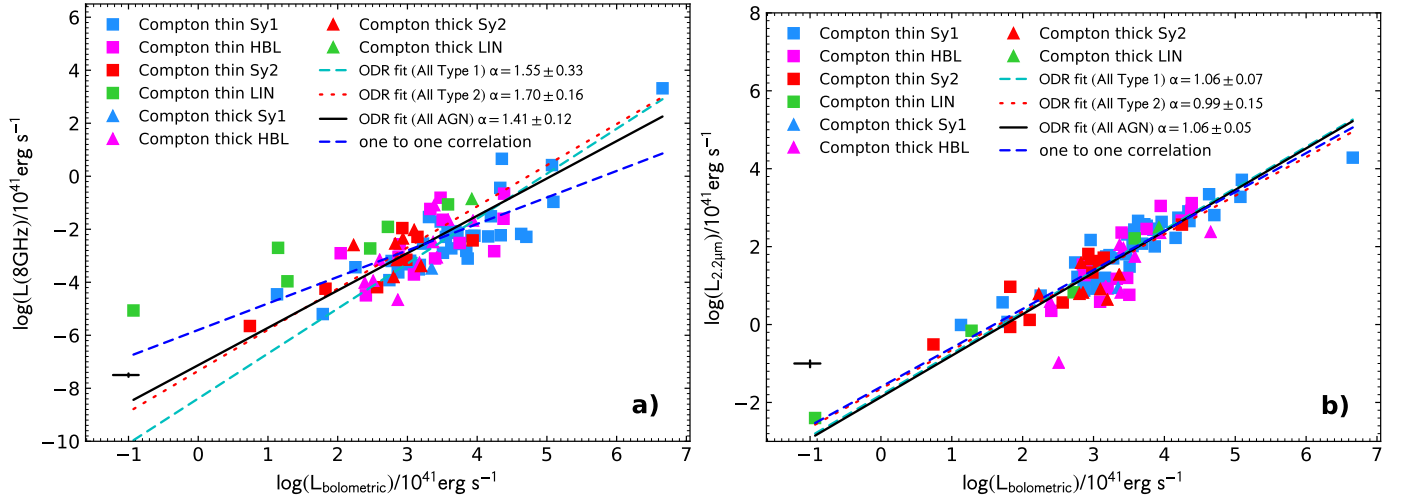


Figure 6. (a): 8.4 GHz luminosity versus bolometric luminosity. (b): Nuclear K-band luminosity versus bolometric luminosity.

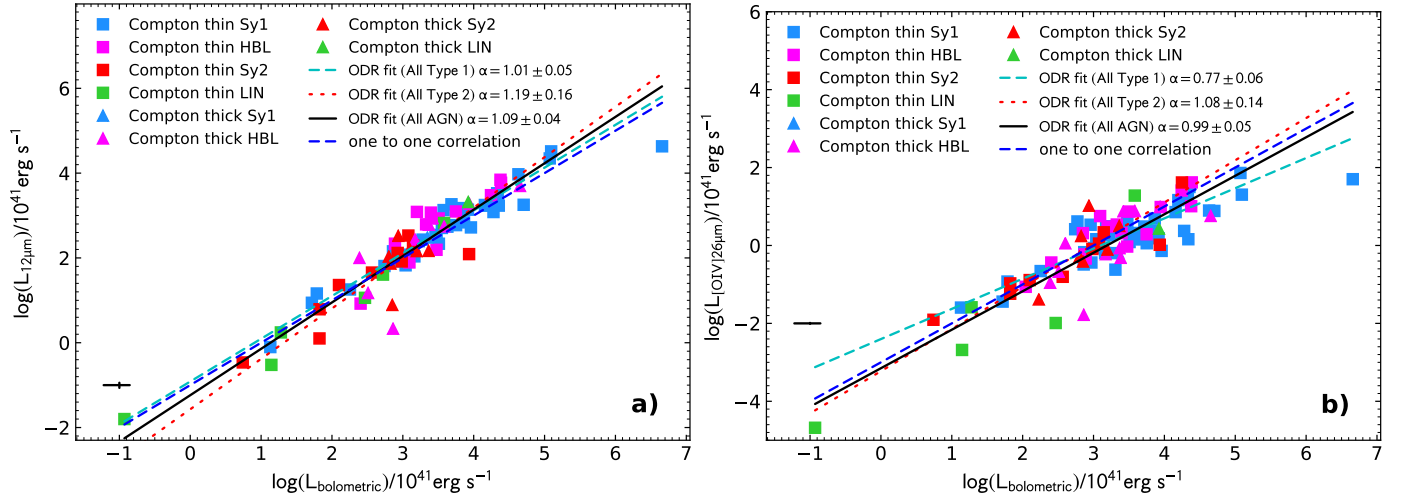


Figure 7. (a): Nuclear $12\mu\text{m}$ luminosity versus bolometric luminosity. (b): [OIV] $26\mu\text{m}$ luminosity versus bolometric luminosity.

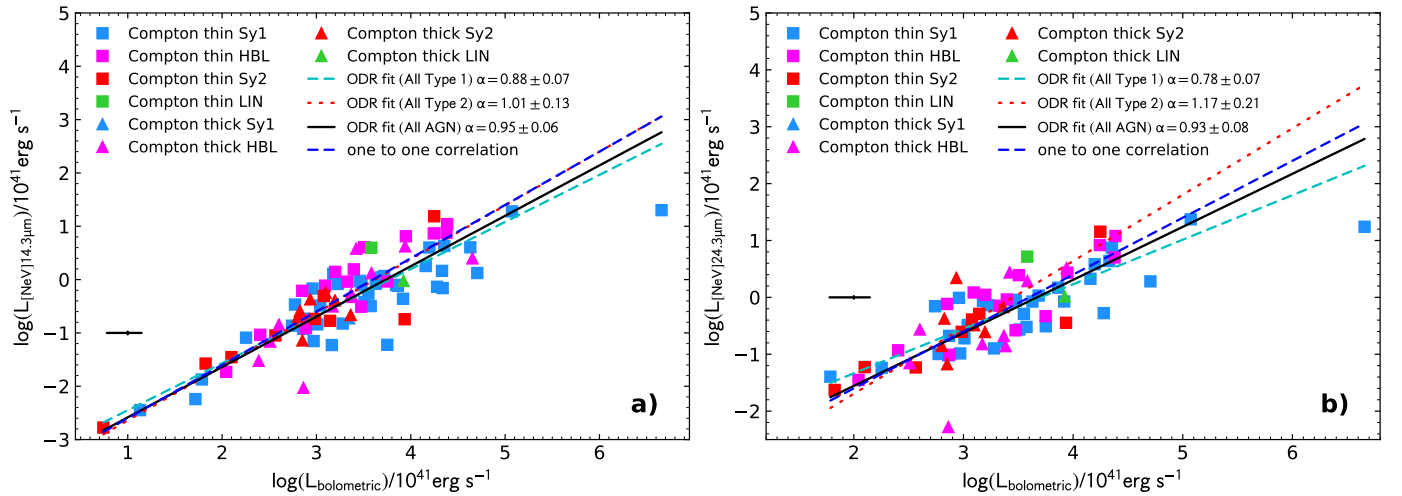


Figure 8. (a): [NeV] $14.3\mu\text{m}$ luminosity versus bolometric luminosity. (b): [NeV] $24.3\mu\text{m}$ luminosity versus bolometric luminosity.

Fig. 7a and b show the correlations between the nuclear $12\mu\text{m}$ luminosity and the [OIV] $26\mu\text{m}$ luminosity and the

bolometric luminosity, respectively. The nuclear $12\mu\text{m}$ lu-

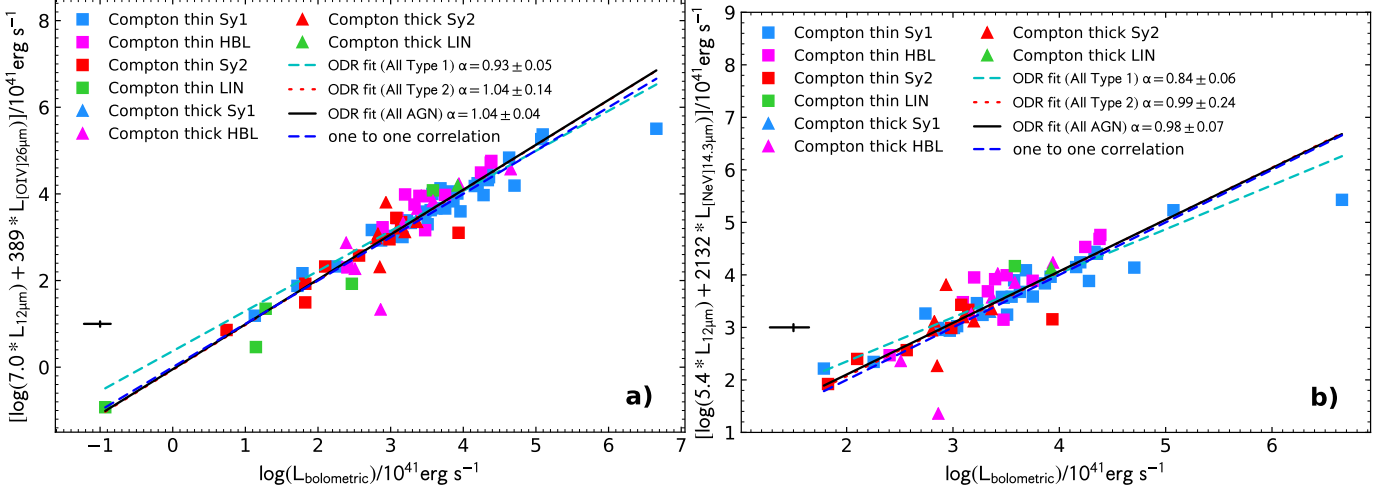


Figure 9. (a): Composite $12\mu\text{m}$ and $[\text{OIV}]26\mu\text{m}$ luminosity versus bolometric luminosity. (b): Composite $12\mu\text{m}$ and $[\text{NeV}]14.3\mu\text{m}$ luminosity versus bolometric luminosity.

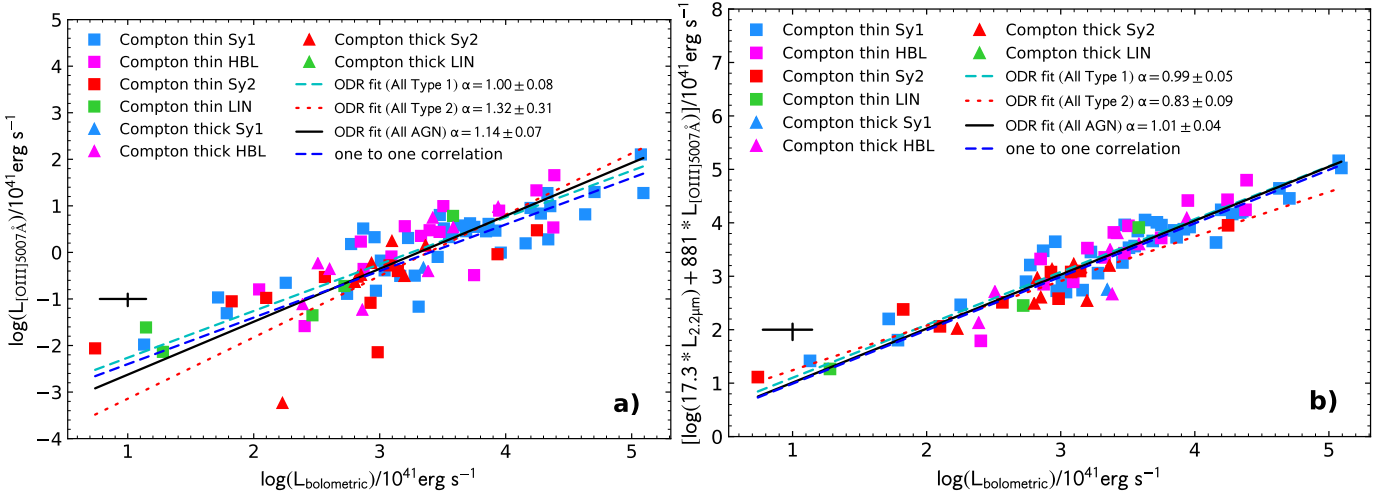


Figure 10. (a): $[\text{OIII}]5007\text{\AA}$ luminosity versus bolometric luminosity. (b): Composite nuclear K-band and $[\text{OIII}]5007\text{\AA}$ luminosity versus bolometric luminosity.

minosity has a strong and linear correlation with the bolometric luminosity. This linearity is known since the pioneering work of [Spinoglio & Malkan \(1989\)](#), who selected galaxies in the IRAS $12\mu\text{m}$ band to produce an unbiased sample of active galaxies. The IRAS large-aperture flux densities were indeed contaminated in galaxies by stellar emission, however for the Seyfert galaxies the emission from the AGN tends to dominate the power in this spectral region. Also the $[\text{OIV}]26\mu\text{m}$ luminosity, originating mostly in the NLR of the AGN, has an almost linear correlation for the whole AGN sample ($\alpha = 0.96 \pm 0.05$), with the AGN bolometric luminosity, albeit with a larger scatter with slopes ranging from 0.7 for the type 1 objects to 1.1 for the type 2’s. We note that the higher bolometric luminosity type 1 AGN have a weaker emission in the NLR mid-IR fine structure lines, which flattens the slope of the correlation.

Figures 8a and b show the correlations between the $[\text{NeV}]14.3\mu\text{m}$ luminosity and the $[\text{NeV}]24.3\mu\text{m}$ luminosity with the bolometric luminosity, respectively. These correlations are shallower than linear for the whole sample and especially for the brighter type 1 objects, showing again, as for the case of $[\text{OIV}]26\mu\text{m}$, that at high bolometric luminosity the NLR becomes relatively weaker than expected from a linear correlation. This indicates that the relation between the NLR fine structure mid-IR lines and the bolometric luminosity may not extend linearly up to the regime of quasars, i.e. AGN with bolometric luminosities above $10^{46}\text{ erg s}^{-1}$. Studies based on brighter AGN samples suggest that at these high luminosities, the forbidden line luminosities can no longer “keep up” with the non-stellar continuum (see discussion of $[\text{OIII}]$ in the Appendix of [Malkan et al. 2017](#)). A possible explanation for this “forbidden line saturation” may be that

the narrow line region is becoming “matter-bounded” (Pronik & Chuvaev 1972; Gaskell et al. 2021). There may not be enough gas around luminous quasars to intercept as many of their ionizing photons.

Figures 9a and b, respectively, show the correlations between a combination of the nuclear $12\mu\text{m}$ luminosity and the NLR [OIV] $26\mu\text{m}$ and [NeV] $14.3\mu\text{m}$ line luminosities with the bolometric luminosity. The addition of a particular percentage of the luminosity of one of the mid-IR high-ionization fine-structure lines of [OIV] $26\mu\text{m}$ or [NeV] $14.3\mu\text{m}$ to the nuclear $12\mu\text{m}$ luminosity has the effect of linearizing the correlation with the bolometric luminosity.

Table 6. Single and composite continuum- and line-based bolometric corrections in AGN.

Continuum
$L_{\text{bol}} = 24.4 \times (L_{2-10\text{keV}})^{0.98 \pm 0.03}$
$L_{\text{bol}} = 10.2 \times (L_{14-195\text{keV}})^{1.02 \pm 0.04}$
$L_{\text{bol}} = 13.5 \times (L_{12\mu\text{m}}^{\text{nuc}})^{0.91 \pm 0.04}$
$L_{\text{bol}} = 56.2 \times (L_{\text{K}}^{\text{nuc}})^{0.94 \pm 0.05}$
Line
$L_{\text{bol}} = 1542 \times (L_{[\text{OIV}]26})^{1.01 \pm 0.06}$
$L_{\text{bol}} = 5420 \times (L_{[\text{NeV}]14.3})^{1.06 \pm 0.07}$
$L_{\text{bol}} = 4667 \times (L_{[\text{NeV}]24.3})^{1.07 \pm 0.09}$
$L_{\text{bol}} = 2042 \times (L_{[\text{OIII}]5007})^{0.88 \pm 0.06}$
Composite
$L_{\text{bol}} = 7.0 \times L_{12\mu\text{m}}^{\text{nuc}} + 389 \times L_{[\text{OIV}]26}$
$L_{\text{bol}} = 5.4 \times L_{12\mu\text{m}}^{\text{nuc}} + 2132 \times L_{[\text{NeV}]14.3}$
$L_{\text{bol}} = 17.3 \times L_{\text{K}}^{\text{nuc}} + 881 \times L_{[\text{OIII}]5007}$

Finally, Figures 10a and b show, respectively, the [OIII] 5007\AA luminosity as a function of the bolometric luminosity and a combination of the nuclear K-band luminosity and the [OIII] 5007\AA line luminosity with the bolometric luminosity. The K-band nuclear luminosity was chosen in this case because: (i) it has a good linear correlation with the bolometric luminosity (see Table 5) and it is at the closest wavelength (about four times longer) to the [OIII] 5007\AA line, which has already been used to estimate the bolometric luminosity of AGN.

The combination of a continuum band nuclear luminosity in the IR (both mid-IR and near-IR) with a line luminosity – when this line is mainly powered by the AGN – gives a better correlation with the bolometric luminosity, compared to the correlations between the line luminosities and the bolometric luminosity. This can be clearly seen comparing Fig. 7b with Fig. 9a, Fig. 8a with Fig. 9b and finally Fig. 10a with Fig. 10b. Moreover, in analogy with the measure of the

star formation rate (SFR) in galaxies using both the $24\mu\text{m}$ continuum and the optical $\text{H}\alpha$ line by Kennicutt & Evans (2012), the logic behind the composite tracers is that lines are complementary to continuum, because they account for photons that are not captured by the dust, so the combination of the two is expected to reduce the scatter, as we show in Figs. 7, 8, 9 and 10.

In Table 6 we give our derived bolometric corrections for the full AGN population. The bolometric corrections are given for the continuum X-ray (both 2-10 keV and 14-195 keV) and IR luminosities (nuclear $12\mu\text{m}$ and K-band), for the luminosities of the brightest lines emitted by the NLR ([OIV] $26\mu\text{m}$, [NeV] $14.3\mu\text{m}$, [NeV] $24.3\mu\text{m}$ and [OIII] 5007\AA) and for a combination of the mid-IR and near-IR luminosities with the mid-IR fine structure and the [OIII] 5007\AA line luminosities, respectively.

We note here that our derived bolometric correction for the [OIII] 5007\AA line luminosity is lower by about a factor two, compared to the derivation of Heckman et al. (2004), who give a linear correlation ($L_{\text{bol}} \sim 3500 L_{[\text{OIII}]5007\text{\AA}}$), while we find a shallower slope of $\alpha \sim 0.90$.

Similar correlations were found for the AGN monochromatic vs. bolometric luminosities when the luminosities are expressed in Eddington units, as shown in Figs. 26, 27, 28 and Table 11 in Appendix B.

3.3. Flux-flux correlations

We show in Fig. 11a and b the correlations between the observed $12\mu\text{m}$ flux and the [OIV] $26\mu\text{m}$ line flux, respectively, with the derived bolometric flux of our sample galaxies. The statistics of these correlations are given in Table 12. Although the scatter is large, these correlations are consistent with linearity, within 2σ . We show this example to demonstrate that our luminosity-luminosity correlations, even if they are boosted by the distance-squared factors, are indeed real, because the corresponding correlations in flux are almost linear. Additionally, we also explored the flux-flux correlations for the 2-10 keV and $2.2\mu\text{m}$ bands. Fig. 29 and Table 12 in Appendix C show that the correlation with the bolometric flux is also significant without the distance term.

3.4. Median spectral energy distributions

We have computed the median SEDs of the four classes of AGN in our sample: Seyfert type 1, HBL, Seyfert type 2, and LINER galaxies, which are shown in Figs. 12–15, respectively, and the relevant values, for each of the 10 photometric bands, are reported in Table 7. The individual SEDs of all galaxies of our sample, normalized to their bolometric luminosity, are shown in the Appendix A. The Seyfert type 1 galaxies are shown in Figs. 21–22, the Hidden Broad Line Galaxies (HBL) galaxies in Fig. 23, the Seyfert type 2 in Fig. 24, while in Fig. 25 are shown the normalized SED of

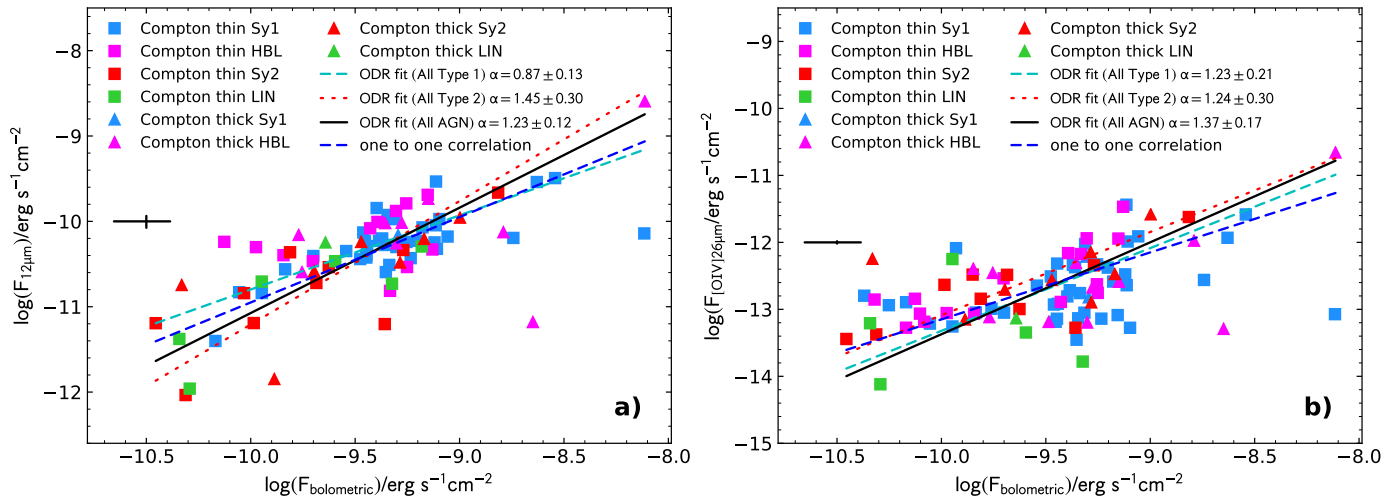


Figure 11. (a): $12\mu\text{m}$ nuclear flux as a function of the estimated bolometric flux. (b): $[\text{OIV}]26\mu\text{m}$ line flux as a function of the estimated bolometric flux.

the non-Seyfert galaxies, including LINERs, a galaxy classified as a non-Seyfert (NGC 1056) and another one classified as a Starburst (NGC 6810).

Our purpose is twofold. First, we define the median distributions of the four classes of AGN, because they can be used as local templates, to be compared with SED of high-redshift AGN. Secondly, we want to explore if and how the four subsamples of AGN may still include, even after the aperture corrections we have applied to subtract the galaxy contribution, a significant contribution from starlight emission, or may be affected by dust obscuration (see Section 4.1).

For each AGN class, the median SED has been derived from the median value of the individual SED distribution evaluated at each frequency sampled (solid line and symbols in Figs. 12–15). Prior to the median computation, the individual SEDs were normalized to their median νL_ν value over the frequency range. This approach avoids the arbitrary selection of a reference wavelength for the normalization that would produce a zero dispersion band in the median SED. To account for the dispersion around the median SED we also compute, at each wavelength, the 10, 30, 70, and 90 percentiles (see Table 7). The dark-shaded areas in Figs. 12–15 indicate the SED distribution between percentiles 30 and 70, whereas the light-shaded areas correspond to the interval between percentiles 10 and 90.

4. DISCUSSION

4.1. Median SEDs and host galaxy contribution

Overall, the median SEDs show two maximum values, one in the mid-IR and another in the X-ray range. Sy1 galaxies clearly show a rising optical/UV continuum with increasing frequency, whereas HBL, Sy2 and LINER galaxies tend to show a rather flat or a depressed optical/UV continuum, possibly contaminated by the host galaxy light (see discussion below). For comparison, we have included in Fig. 12 the me-

dian SED of the radio-quiet quasars of the sample of Shang et al. (2011). The two determinations agree very well in the spectral region from the radio to the UV, while at X-ray frequencies the derivation of Shang et al. (2011) is about one order of magnitude fainter. The blue optical/UV continuum in Sy1 nuclei is similar to the big blue bump associated with the accretion disk emission in bright quasars (Malkan & Sargent 1982), although the median quasar SEDs show a more pronounced blue bump, a relatively fainter IR bump and fainter X-ray emission (Elvis et al. 1994; Krawczyk et al. 2013; Saccheo et al. 2023). This is in agreement with the median SED changes reported by Krawczyk et al. (2013) for the less luminous quasars in their sample ($\sim 10^{44.9} \text{ erg s}^{-1}$), which show a less pronounced blue bump component. The median Sy1 SED in Fig. 12 extends this trend to lower luminosities, with a prominent IR bump brighter than the blue bump component in agreement with the median Seyfert SEDs derived from sub-arcsecond resolution observations by Prieto et al. (2010). These changes in the SED are probably due to the decreasing contribution of the accretion disk to the total energy output, or to the increasing fraction of the reprocessed emission in AGN with decreasing luminosity.

When compared to Seyfert galaxies, the median SED of LINERs is brighter at radio wavelengths, in agreement with the results obtained by Ho (2008). For comparison, we have included in Fig. 15 the median SED of the radio-loud quasars of the sample of Shang et al. (2011). These SEDs do agree to first order, showing a certain radio loudness in the LINER SED, in spite of the fact that our LINER sample is small and not fully representative. Obscured nuclei, namely HBL and Sy2, shown in Fig. 13 and in Fig. 14, respectively, have a depressed optical/UV continuum when compared to Seyfert 1 nuclei and a larger scatter in both optical/UV and X-ray ranges, suggesting that obscuration by dust and gas is still a source of scatter even after the absorption corrections have

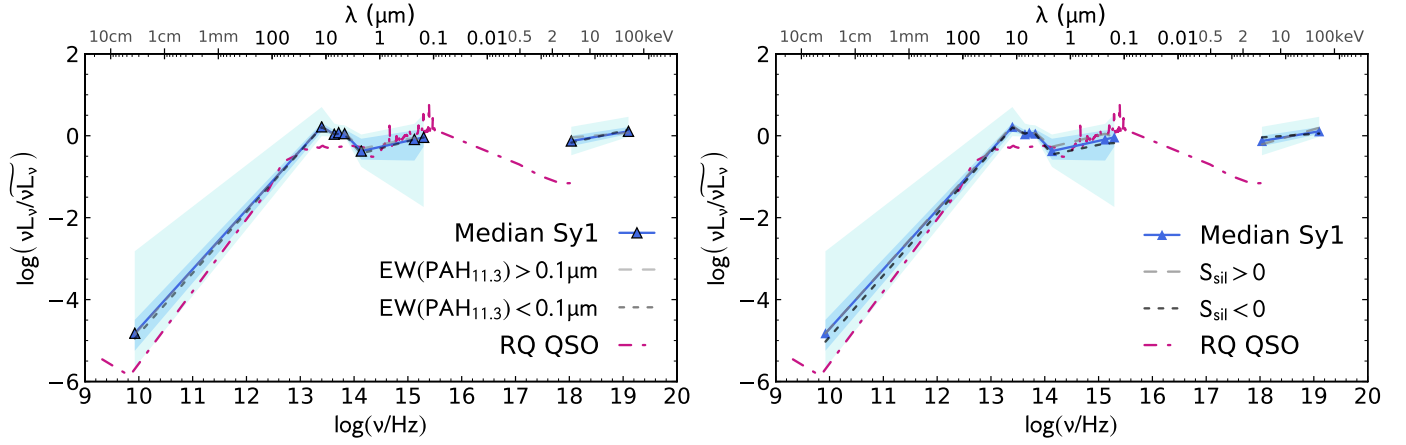


Figure 12. Median rest-frame SED for the Seyfert type 1 galaxies, compared to the SED of the radio-quiet quasar population from Shang et al. (2011), shown as a red dot-dashed line. (a:) The population has been divided between the galaxies with high and low value of the EW of the PAH11.3 μm feature (b:) The population has been divided between the galaxies with the silicates 9.7 μm feature in emission and in absorption.

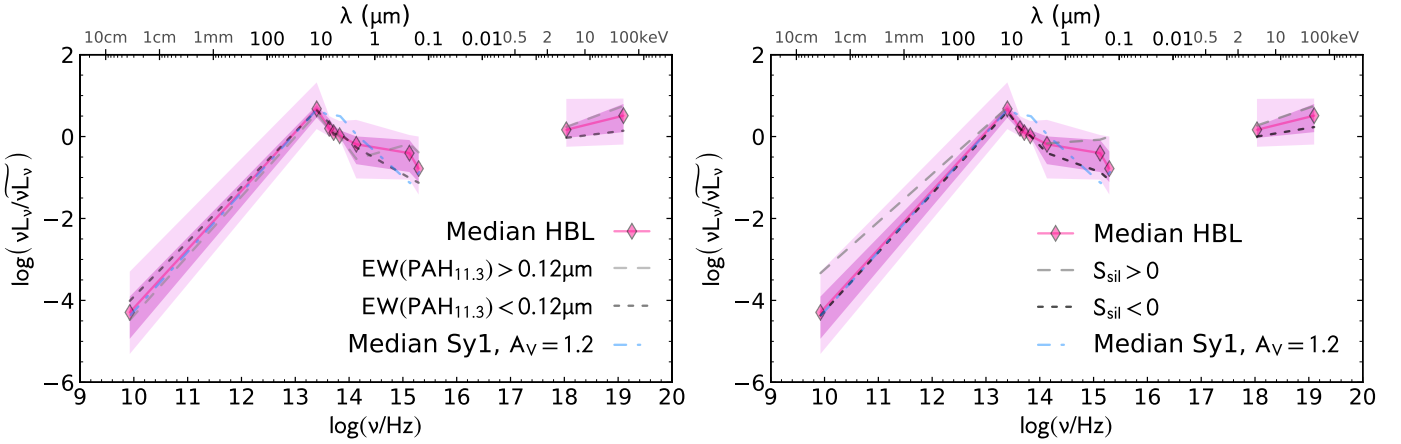


Figure 13. Median rest-frame SED for the HBL galaxies. (a:) Same as in Fig. 12a (b:) Same as in Fig. 12b.

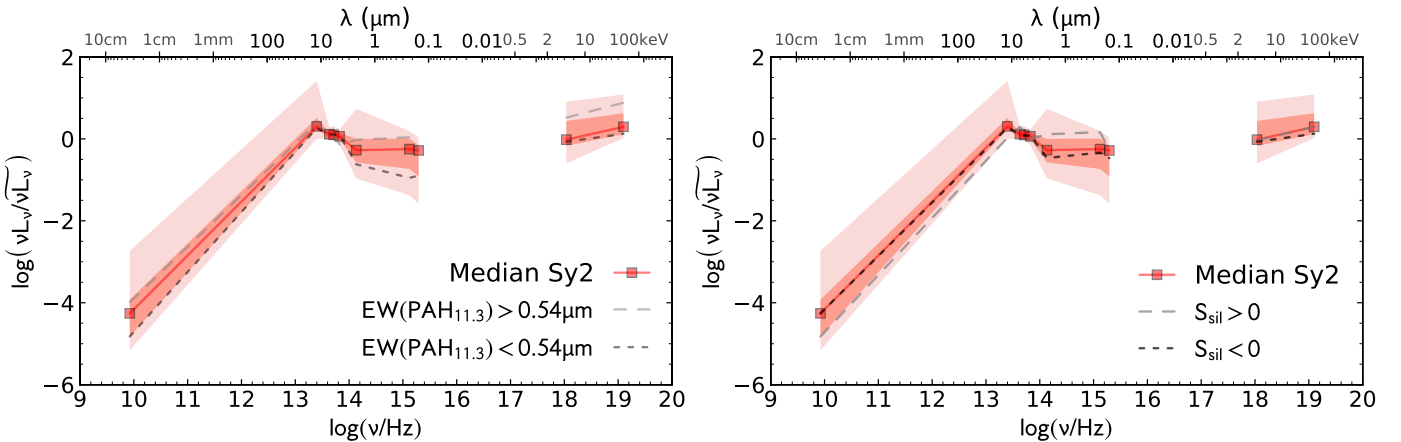


Figure 14. Median rest-frame SED for the Seyfert type 2 galaxies. (a:) Same as in Fig. 12a (b:) Same as in Fig. 12b.

been applied. On the other hand, LINERs show a relatively flat SED in the optical/UV range, possibly dominated by the starlight contribution from the host galaxy.

Irrespective of the type of AGN considered, the four median SEDs have their minimum scatter in the mid-IR, namely in the four photometric bands at 4.5, 5.8, 7.0 μm and, to a

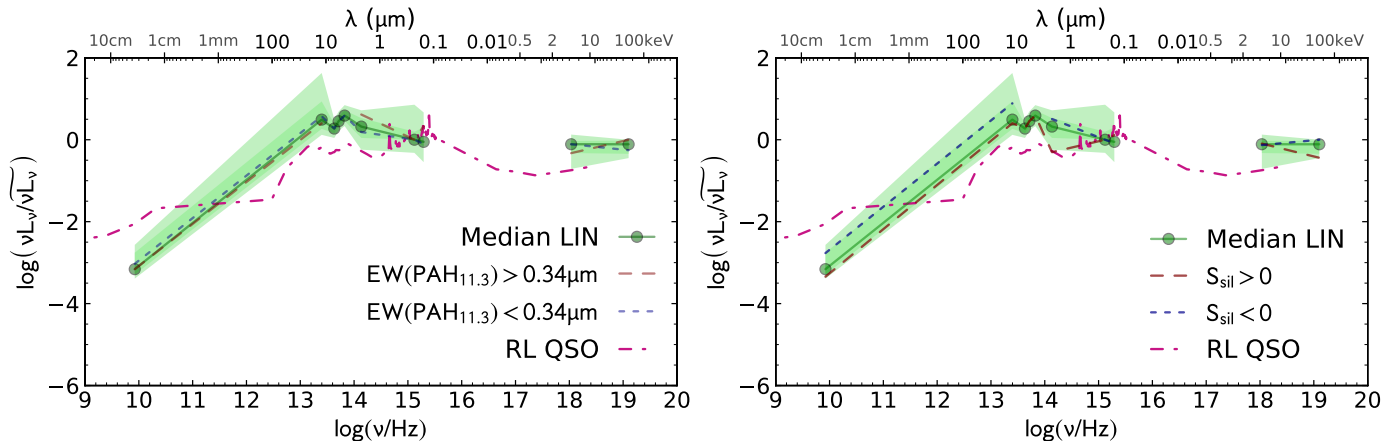


Figure 15. Median rest-frame SED for the LINER galaxies, compared to the SED of the radio-loud quasar population from [Shang et al. \(2011\)](#), shown as a red dot-dashed line. **(a):** Same as in Fig. 12a **(b):** Same as in Fig. 12b.

lesser extent, at $12 \mu\text{m}$. This result confirms that the mid-IR continuum contains a constant fraction of the bolometric flux for all types of active galaxies ([Spinoglio & Malkan 1989](#)), a discovery that was initially based on large-aperture flux densities from IRAS ([Neugebauer et al. 1984](#)). In this work we come to the same conclusion using nuclear $12 \mu\text{m}$ flux measurements at sub-arcsecond resolution, avoiding most of the contribution by the host galaxy emission, and the corresponding corrected mid-IR fluxes from *Spitzer*.

To evaluate the possible contamination in the optical/UV range of the median AGN SEDs due to current star formation in the host galaxies, we use the equivalent width of the PAH feature at $11.25 \mu\text{m}$ as a proxy for the star formation rate (see, e.g. [Förster Schreiber et al. 2004](#); [Mordini et al. 2021](#)), which is not affected by AGN contamination (e.g. [Lai et al. 2022](#)). Additionally, dust obscuration can also affect the shape of the optical/UV continuum, either due to nuclear dust (i.e. the torus) or due to host galaxy dust. To investigate this scenario we use the strength of the silicate feature at $9.7 \mu\text{m}$ (S_{sil} ; [Spoon et al. 2007](#)), which becomes negative for obscured sources but can also be positive for unobscured sources if dust irradiated by the active nucleus is seen along the line of sight. We have therefore divided the objects in each of the four classes on the basis of these two observed quantities, using as threshold (between low and high values) the median value of the PAH at $11.25 \mu\text{m}$, and negative or positive values of S_{sil} . The spectroscopic data have been taken from [Wu et al. \(2009\)](#), who measured most of the $12 \mu\text{m}$ AGN with the *Spitzer*-IRS spectrograph in the low resolution mode.

Fig. 12a shows the median SEDs obtained from the Seyfert 1 sample with $\text{EW}(\text{PAH } 11.25 \mu\text{m})$ values below (dotted-green line) and above (dashed-red line) $0.1 \mu\text{m}$. Following the SFR calibration based on the luminosity of the PAH $11.25 \mu\text{m}$ derived by [Xie & Ho \(2019\)](#), we obtain a median $\text{SFR} \sim 0.7\text{--}0.8 M_{\odot} \text{yr}^{-1}$ for both sub-samples, con-

sistent with moderate star formation in the host galaxies of Seyfert 1s. Analogously, in Fig. 12b, the population of type 1 Seyferts has been divided in those with the silicates in emission (dashed-red line) and in absorption (dotted-green line). The differences in the median SEDs between the Seyfert 1 sub-samples separated by $\text{EW}(\text{PAH } 11.25 \mu\text{m})$ or S_{sil} are negligible for all the wavelengths sampled, suggesting that the median Seyfert type 1 SED is not contaminated by stellar light and does not suffer from heavy dust absorption.

Figs. 13a and b show the same analysis for HBL galaxies, which present a similar median $\text{EW}(\text{PAH } 11.25 \mu\text{m})$ value of $0.12 \mu\text{m}$ as Seyfert galaxies. Nevertheless, the HBL populations with $\text{EW}(\text{PAH } 11.25 \mu\text{m}) > 0.12 \mu\text{m}$ or positive S_{sil} values show a significantly higher continuum in both NUV and FUV bands (dashed-green lines in Figs. 13a and b) when compared with those below $\text{EW}(\text{PAH } 11.25 \mu\text{m}) < 0.12 \mu\text{m}$ or negative S_{sil} (dotted-blue lines). When the PAH $11.25 \mu\text{m}$ luminosities are translated into SFRs, the sub-sample with $\text{EW}(\text{PAH } 11.25 \mu\text{m}) > 0.12 \mu\text{m}$ has a median $\text{SFR} \sim 0.9 M_{\odot} \text{yr}^{-1}$, while the sub-sample with $\text{EW}(\text{PAH } 11.25 \mu\text{m}) < 0.12 \mu\text{m}$ shows a median $\text{SFR} \sim 0.6 M_{\odot} \text{yr}^{-1}$. As in the case of Seyfert 1 nuclei, the contribution from star formation is moderate, however HBL nuclei are dust obscured and therefore, at similar SFR values, the host galaxy dominates in the UV range. Sources with lower star formation rates tend to show a decreasing IR-to-UV continuum and the silicate feature in absorption, consistent with a reddened nuclear continuum, as discussed in Section 4.2.

Seyfert 2 galaxies have significantly larger $\text{EW}(\text{PAH } 11.25 \mu\text{m})$ with a median value of $0.54 \mu\text{m}$, i.e. about five times that of Seyfert 1 and HBL galaxies, meaning that their host galaxies are relatively more active at forming stars in agreement with previous studies ([Edelson et al. 1987](#); [Maiolino et al. 1995](#); [Buchanan et al. 2006](#)). As in the case of HBL, Figs. 14a and b show that the median SED of the Seyfert 2 population with large $\text{EW}(\text{PAH } 11.25 \mu\text{m})$ or pos-

Table 7. Percentiles of the normalized SED distribution as a function of frequency for the four AGN classes.

Seyfert 1									
$\log \nu$ [Hz]	$\log(\nu F_\nu)_{10}$	$\log(\nu F_\nu)_{30}$	$\log(\nu F_\nu)_{\text{med}}$	$\log(\nu F_\nu)_{70}$	$\log(\nu F_\nu)_{90}$	$\log(\nu F_\nu)_{\text{med}}^{<EW113}$	$\log(\nu F_\nu)_{\text{med}}^{>EW113}$	$\log(\nu F_\nu)_{\text{med}}^{-Ssil}$	$\log(\nu F_\nu)_{\text{med}}^{+Ssil}$
	[normalized to median νF_ν]								
9.937	-5.657	-5.249	-4.821	-4.495	-2.82	-4.952	-4.849	-5.027	-4.824
13.411	-0.01	0.097	0.217	0.309	0.7	0.208	0.227	0.2	0.249
13.645	-0.021	0.011	0.037	0.137	0.297	0.04	0.016	0.051	0.014
13.726	-0.01	0.019	0.075	0.115	0.268	0.044	0.087	0.084	0.018
13.837	-0.015	0.009	0.051	0.154	0.254	0.026	0.069	0.044	0.069
14.147	-0.76	-0.584	-0.373	-0.073	0.029	-0.433	-0.316	-0.456	-0.269
15.134	-1.592	-0.606	-0.091	0.131	0.29	-0.093	-0.046	-0.19	0.047
15.306	-1.739	-0.266	-0.039	0.133	0.522	-0.043	-0.171	-0.179	-0.032
18.049	-0.476	-0.253	-0.128	0.0	0.218	-0.169	-0.04	-0.04	-0.209
19.112	-0.027	0.04	0.108	0.211	0.462	0.152	0.071	0.053	0.195
HBL									
$\log \nu$ [Hz]	$\log(\nu F_\nu)_{10}$	$\log(\nu F_\nu)_{30}$	$\log(\nu F_\nu)_{\text{med}}$	$\log(\nu F_\nu)_{70}$	$\log(\nu F_\nu)_{90}$	$\log(\nu F_\nu)_{\text{med}}^{<EW113}$	$\log(\nu F_\nu)_{\text{med}}^{>EW113}$	$\log(\nu F_\nu)_{\text{med}}^{-Ssil}$	$\log(\nu F_\nu)_{\text{med}}^{+Ssil}$
	[normalized to median νF_ν]								
9.936	-5.309	-4.936	-4.293	-3.907	-3.298	-4.011	-4.478	-4.368	-3.335
13.41	0.182	0.462	0.676	0.766	1.322	0.644	0.569	0.611	0.709
13.644	0.006	0.131	0.197	0.431	0.499	0.328	0.168	0.197	—
13.725	0.008	0.045	0.096	0.28	0.445	0.047	0.118	0.096	—
13.836	-0.056	-0.002	0.02	0.156	0.38	0.087	0.0	0.02	—
14.146	-1.023	-0.674	-0.189	0.003	0.407	-0.266	-0.546	-0.402	-0.168
15.133	-1.052	-0.866	-0.405	-0.085	0.038	-1.009	-0.18	-0.866	-0.077
15.305	-1.416	-1.112	-0.783	-0.364	0.0	-1.128	-0.387	-1.064	0.0
18.049	-0.25	-0.033	0.165	0.253	0.919	-0.032	0.236	0.0	0.269
19.112	-0.195	0.108	0.51	0.796	0.927	0.142	0.747	0.231	0.747
Seyfert 2									
$\log \nu$ [Hz]	$\log(\nu F_\nu)_{10}$	$\log(\nu F_\nu)_{30}$	$\log(\nu F_\nu)_{\text{med}}$	$\log(\nu F_\nu)_{70}$	$\log(\nu F_\nu)_{90}$	$\log(\nu F_\nu)_{\text{med}}^{<EW113}$	$\log(\nu F_\nu)_{\text{med}}^{>EW113}$	$\log(\nu F_\nu)_{\text{med}}^{-Ssil}$	$\log(\nu F_\nu)_{\text{med}}^{+Ssil}$
	[normalized to median νF_ν]								
9.937	-5.163	-4.825	-4.26	-3.924	-2.734	-4.825	-3.989	-4.26	-4.825
13.411	0.007	0.236	0.306	0.51	1.417	0.261	0.393	0.27	0.024
13.645	-0.011	0.036	0.115	0.155	0.289	0.115	0.073	0.115	0.298
13.726	-0.028	0.05	0.097	0.239	0.313	0.105	0.097	0.079	0.158
13.837	-0.151	-0.005	0.063	0.148	0.231	0.097	-0.142	0.081	0.0
14.147	-0.967	-0.577	-0.275	0.0	0.733	-0.622	-0.024	-0.466	0.112
15.134	-1.375	-0.733	-0.25	0.008	0.192	-0.951	0.038	-0.335	0.165
15.306	-1.582	-0.919	-0.282	-0.167	0.031	-0.898	-0.271	-0.47	-0.271
18.05	-0.599	-0.172	-0.019	0.438	0.908	-0.069	0.52	-0.069	-0.038
19.113	0.021	0.117	0.293	0.625	1.085	0.123	0.881	0.124	0.293
LINERs									
$\log \nu$ [Hz]	$\log(\nu F_\nu)_{10}$	$\log(\nu F_\nu)_{30}$	$\log(\nu F_\nu)_{\text{med}}$	$\log(\nu F_\nu)_{70}$	$\log(\nu F_\nu)_{90}$	$\log(\nu F_\nu)_{\text{med}}^{<EW113}$	$\log(\nu F_\nu)_{\text{med}}^{>EW113}$	$\log(\nu F_\nu)_{\text{med}}^{-Ssil}$	$\log(\nu F_\nu)_{\text{med}}^{+Ssil}$
	[normalized to median νF_ν]								
9.927	-3.537	-3.372	-3.225	-3.084	-2.64	-3.289	-3.196	-3.098	-3.437
13.401	0.046	0.198	0.357	0.646	1.394	0.357	0.495	0.627	0.27
13.635	-0.054	0.053	0.159	0.266	0.373	0.159	—	—	0.159
13.716	0.119	0.229	0.339	0.449	0.559	0.339	—	—	0.339
13.827	0.237	0.357	0.476	0.596	0.715	0.476	—	—	0.476
14.137	-0.36	-0.079	0.106	0.321	0.542	-0.066	0.214	0.321	-0.416
15.124	-0.747	-0.21	0.0	0.019	0.209	0.048	-0.515	0.0	-0.134
15.296	-0.995	-0.304	-0.205	-0.058	0.237	-0.163	-0.567	-0.205	-0.019
18.039	-0.353	0.0	0.0	0.0	0.049	0.0	0.0	0.0	0.0
19.102	-0.039	0.027	0.135	0.25	0.293	0.0	0.207	0.278	-0.032

Notes. For each observed frequency (Hz) (col.1), are given the percentiles 10, 30, 50 (median), 70, and 90 (cols. 2-6) calculated at each frequency for the νF_ν distribution of individual sources. The latter have been previously normalized by their median νF_ν over the frequency range. The last four columns (cols. 7-10) correspond to the median νF_ν distribution for sources below ($<EW113$) or above ($>EW113$) the median EW(PAH11.3 μm) value of their class (0.095 for Sy1, 0.119 for HBL, 0.539 for Sy2), and sources with negative ($-Ssil$) or positive ($+Ssil$) silicate strength values.

itive S_{sil} values present a brighter continuum in the UV but also the K -band (dashed-green line in Figs. 14), in agreement with their higher median SFR of $\sim 4 M_{\odot} \text{yr}^{-1}$. However, the population with lower EW(PAH 11.25 μm) or negative S_{sil} values may still be affected by this contribution, since they show a relatively flat IR-to-UV continuum (dotted-blue line), although their median SFR $\sim 0.6 M_{\odot} \text{yr}^{-1}$ is comparable to that of Seyfert 1 and HBL host galaxies.

The differences between Seyfert 1, HBL, and Seyfert 2 galaxies are clearly shown in the diagram of the silicate strength at 9.7 μm as a function of the PAH 11.25 μm feature – S_{sil} vs. EW(PAH 11.25 μm) – reported in Fig. 16. Both HBL and Seyfert 2 galaxies are obscured by a similar amount according to their median $S_{\text{sil}} \sim -0.23$, which is larger than that in Seyfert 1s (median $S_{\text{sil}} \sim 0.0$). However, the host galaxies of HBLs and Seyfert 1s form stars at a similar rate (0.6–0.9 $M_{\odot} \text{yr}^{-1}$), about 4–6 times lower than that of Seyfert 2 hosts with EW(PAH 11.25 μm) $> 0.54 \mu\text{m}$.

The LINER population in our sample is less numerous and more heterogeneous with a large dispersion in EW(PAH 11.25 μm) and S_{sil} (Fig. 16). The median EW(PAH 11.25 μm) of 0.34 μm is not representative of the population, with about half of the sources showing values similar to the Seyfert 1 nuclei (median SFR $\sim 0.1 M_{\odot} \text{yr}^{-1}$) and the others showing high values indicative of more intense star formation activity (median SFR $\sim 1.7 M_{\odot} \text{yr}^{-1}$). On the other hand, only two sources show strong silicate absorption, with a median $S_{\text{sil}} \sim -0.05$. This dual behavior in the IR spectroscopic properties of LINERs is in agreement with previous studies (Dudik et al. 2009; Fernández-Ontiveros & Muñoz-Darias 2021). The differences between the median SEDs for the sub-populations with large/small EW(PAH 11.25 μm) or positive/negative S_{sil} are relatively small (Figs. 15a and b) and may be attributed to the small number statistics and the large heterogeneity in the LINER class.

In summary, as can be seen in Fig. 16, most of the Seyfert type 1 AGN have a low 11.25 μm PAH EW (only 5 Sy1 have EW(PAH 11.25 μm) $> 0.4 \mu\text{m}$) and have silicate strength around zero. Hidden Broad Line (HBL) galaxies have a larger spread in the silicate strength, while keeping a low number of high PAH EW (6 HBL have EW(PAH 11.25 μm) $> 0.4 \mu\text{m}$). In contrast, the majority of the Seyfert type 2 galaxies have a large PAH EW (14 Sy2 have EW(PAH 11.25 μm) $> 0.4 \mu\text{m}$, while only 7 have EW(PAH 11.25 μm) $< 0.4 \mu\text{m}$).

4.2. Dust properties in obscured Seyferts

Figures 13a and b show that the continuum shape of the median HBL SED with low star formation rates (low EW(PAH 11.25 μm) or negative S_{sil} (dashed-green lines) can be reproduced by the median Sy1 template after applying a

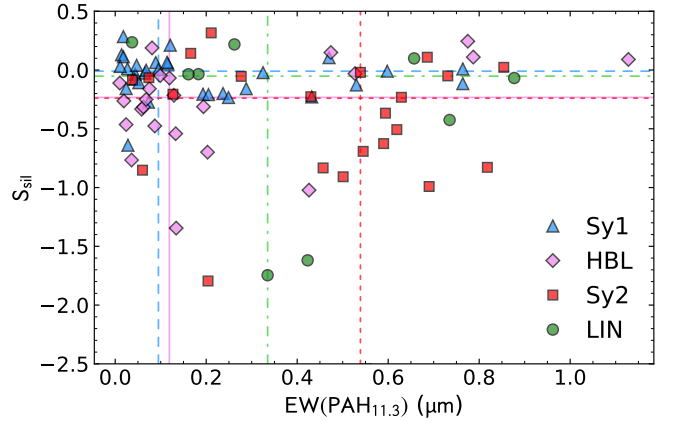


Figure 16. Silicate strength as a function of the EW of the PAH11.3 μm feature for the four AGN populations of Sy1 (blue triangles), HBL (pink diamonds), Sy2 (red squares) and LINERs (green circles). The median EW(PAH11.3 μm) and silicate strength values for Sy1 (dashed blue), HBL (solid pink), Sy2 (dotted red) and LINERs (dot-dashed green) are indicated by the horizontal and vertical lines, respectively.

moderate amount of dust reddening. Assuming a foreground dust screen and the extinction curve from Cardelli et al. (1989), a total extinction of $A_V \sim 1.2$ mag (dashed-blue line in Figs. 13a and b) is required. This moderate amount of dust obscuration is enough to hide the continuum emission of a Sy1 and thus reproduce the observed SED shape of an HBL nucleus.

An additional estimate of the dust extinction in these nuclei is provided by the strength of the silicate feature. For a foreground dust screen, the silicate strength corresponds to the optical depth ($S_{\text{sil}} = -\Delta\tau_{9.7}$). Comparing the differential extinction in the optical between Seyfert 1 and HBL nuclei ($A_V \sim 1.2$ mag), and the silicate optical depth ($\Delta\tau_{9.7} \sim 0.23$) provides some information about the dust properties. We obtain a ratio of $A_V/\Delta\tau_{9.7} \sim 5.2$, in agreement with typical values in AGN (e.g. Lyu et al. 2014), as opposed to the much larger $A_V/\Delta\tau_{9.7} \sim 18$ derived for the local ISM dust in the Milky Way (Roche & Aitken 1984). This suggests that the obscuration may be dominated by large grains that lead to a flatter and featureless extinction curve (Maiolino et al. 2001a,b; Shao et al. 2017). Nevertheless, the effect of a more complex geometry in the dust distribution should be explored in the future to confirm this scenario.

4.3. Comparison with other bolometric corrections

We compare here the bolometric luminosities derived for type 1 and type 2 AGN in our sample with those from other methods. First, in Fig. 17 we compare them with the bolometric luminosities computed from the 2–10 keV intrinsic flux using the bolometric correction of Lusso et al. (2012). We adopted the polynomial formula for the bolometric luminosity $y = a_1 \times x + a_2 \times x^2 + a_3 \times x^3 + b$, where

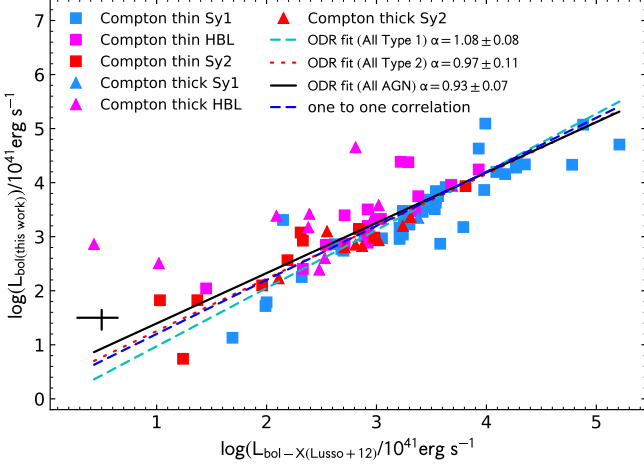


Figure 17. Correlation between the bolometric luminosity computed in this work and the bolometric luminosity computed from the 2-10 keV corrected flux using the bolometric correction of Lusso et al. (2012).

$x = \log(L) - 12$, L is the bolometric luminosity in units of L_{\odot} , $y = \log[L/L_{2-10\text{keV}}]$, and the coefficients depend on the AGN type (type 1 AGN: $a_1 = 0.288$, $a_2 = 0.111$, $a_3 = -0.007$ and $b = 1.308$; type 2 AGN: $a_1 = 0.230$, $a_2 = 0.050$, $a_3 = 0.001$ and $b = 1.256$; see table 2 in Lusso et al. 2012). It appears from Fig. 17 that the two determinations of the bolometric luminosities do agree very well, as shown by the linear slope of the correlation ($\alpha = 0.98 \pm 0.06$).

In Fig. 18 we show the comparison of our determination of the bolometric luminosity with the one derived using the $[\text{OIII}]5007\text{\AA}$ line compiled in Spinoglio et al. (2022) using the bolometric correction of $L_{\text{bol}} \sim 3500 L_{[\text{OIII}]5007\text{\AA}}$ (Heckman et al. 2004). The correlation here is flatter than linear, especially for type 2 objects ($\alpha = 0.66 \pm 0.16$), indicating a deficit of optical forbidden line emission from type 2 AGN, possibly due to obscuration of the emitting NLR.

A recent computation of the hard X-ray 2-10 keV bolometric correction has been provided by Duras et al. (2020), who emphasize the dependence of their bolometric corrections on the bolometric luminosity and separately analyze type 1 and type 2 AGN. In the luminosity range of $10^{40} \lesssim L_{\text{bol}} \lesssim 10^{45.5} \text{ erg s}^{-1}$, we have a similar result when we compare our constant of 15.3, with no dependence on luminosity (see the first line in Table 6), with their result presented in the lower panel of their Fig. 4, relative to the average values for type 1 and type 2 sources. Only at higher bolometric luminosities, i.e. for $L_{\text{bol}} \gtrsim 10^{46} \text{ erg s}^{-1}$ the predictions of Duras et al. (2020) show higher bolometric corrections by factors of 3–4, with a strong dependence on luminosity. This discrepancy can be due to the fact that our study is based on a local sample of AGN with moderate luminosities, with $L_{\text{bol}} \lesssim 10^{46} \text{ erg s}^{-1}$, with the only exception of 3C 273 with $L_{\text{bol}} \sim 4 \times 10^{47} \text{ erg s}^{-1}$ (see Table 3). In contrast, Duras

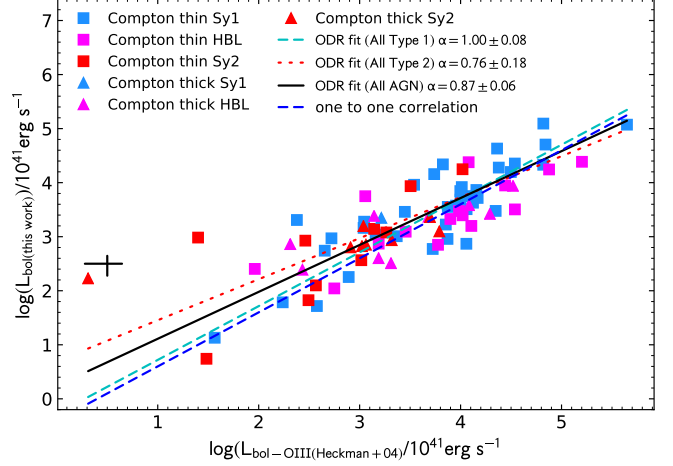


Figure 18. Correlation between the bolometric luminosity computed in this work and the bolometric luminosity computed from the $[\text{OIII}]5007\text{\AA}$ line compiled in Spinoglio et al. (2022) using the bolometric correction of $L_{\text{bol}} \sim 3500 L_{[\text{OIII}]5007\text{\AA}}$ (Heckman et al. 2004).

et al. (2020) include in their study various samples of AGN, X-ray selected, covering different redshift ranges. In particular they include 41 sources of the WISE-SDSS Selected Hyper-luminous sample (WISSH) with $L_{\text{bol}} > 10^{47} \text{ erg s}^{-1}$ in the redshift range $2 < z < 4$, observed in the X-rays (Martocchia et al. 2017), as well as 31 high luminosity type 1 AGN with $L_{\text{bol}} > 10^{46.5} \text{ erg s}^{-1}$ in the redshift range $0.9 < z < 5$ from the XXL sample (see Table 2 of Liu et al. 2016). The inclusion of these high luminosity type 1 AGN has the effect of strongly increasing the 2-10 keV bolometric correction, as can be seen from the upper panel of Fig. 4 of Duras et al. (2020).

We show in Fig. 19 our 2-10 keV bolometric correction as a function of the bolometric luminosity. For comparison, we have included in the plot the fit of the hard X-ray bolometric correction derived from Duras et al. (2020) (see their equation (2) and Fig. 4) for both the general case and for type 1 AGN. In the luminosity range shown in the figure, our results are in a reasonably good agreement with their result. Nevertheless, it can be seen that the derived statistics shown in Fig. 19 indicates a poor correlation, that is consistent with a flat distribution, i.e. a constant bolometric correction as a function of luminosity. The same conclusion of a constant bolometric correction is also valid for the combination of the $12\mu\text{m}$ luminosity and the $[\text{OIV}]26\mu\text{m}$ line luminosity, as is shown in Fig. 20.

5. SUMMARY AND CONCLUSIONS

In this work we have used the $12\mu\text{m}$ sample of local AGN to derive the nuclear SED and the AGN bolometric luminosities, as much as possible free from galactic contamination.

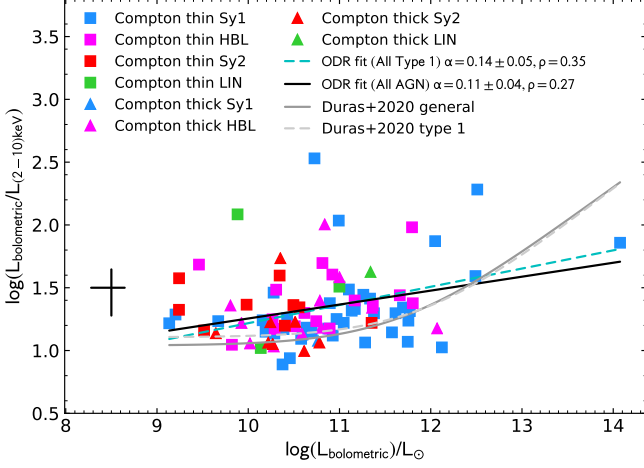


Figure 19. The 2-10 keV bolometric correction as a function of the bolometric luminosity. The ODR fits to the total population and to the type 1 AGN samples have a low Pearson correlation coefficient ($\rho=0.46$ and $\rho=0.36$ for 57 and 90 objects, with $P(\text{null}) = 3 \times 10^{-4}$ and 4×10^{-4} , respectively) indicating that the correlations are not strong. For comparison the hard X-ray bolometric correction from Duras et al. (2020) has been included for both the general case and for type 1 AGN.

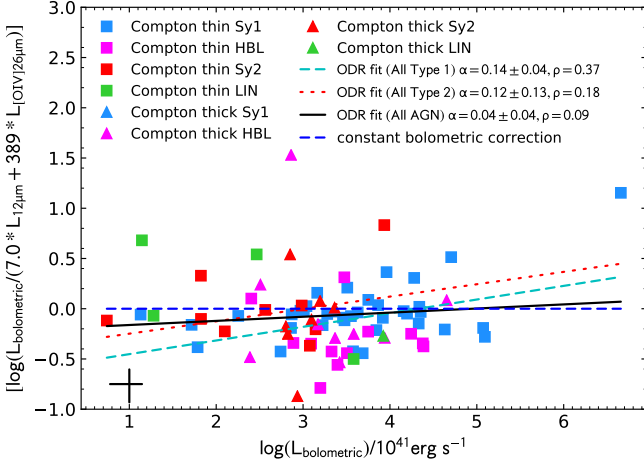


Figure 20. The composite $12\mu\text{m}$ and $[\text{OIV}]26\mu\text{m}$ bolometric correction as a function of the bolometric luminosity. The ODR fits to all populations show very low Pearson correlation coefficients, indicating a constant bolometric correction.

For each galaxy we used a 10-band spectral energy distribution, from the radio to the hard X-rays. To isolate genuine AGN continuum, we included sub-arcsecond photometric data where available, and corrected the bands contaminated by stellar light from the host galaxy. Both the radio observations at 8.4 GHz and most of the $12\mu\text{m}$ photometric data are taken with sub-arcsecond apertures, while the mid-IR bands at 7.0, 5.8, and $4.5\mu\text{m}$ have been corrected using the $12\mu\text{m}$ data. The nuclear K-band photometry was taken from Spinoglio et al. (2022) and the UV data from GALEX

have been corrected for the telescope PSF in the two NUV and FUV bands. Finally, the absorption-corrected 2-10 keV and observed 14-195 keV X-ray fluxes intrinsically originate in the active nuclei.

Using the 10-band *nuclear* photometric data, we derived the median Spectral Energy Distributions (SED) for each AGN type, namely Seyfert type 1, Seyfert nuclei with hidden broad-lines (HBL), Seyfert type 2 and LINERs. The median Seyfert 1 SED shows the characteristic big blue bump feature in the UV, nevertheless the largest contribution to the bolometric luminosity comes from the IR peak and the X-ray continuum. The median SEDs of both HBL and type 2 nuclei are affected by starlight contamination in the optical/UV range. The median nuclear SED of obscured type 1 nuclei can be reproduced by applying a moderate foreground dust extinction of $A_V \sim 1.2$ mag to the median Seyfert 1 SED.

We find that the $12\mu\text{m}$ and the K-band nuclear luminosities have good linear correlations with the bolometric luminosity, similar to those in the X-rays. We derive bolometric corrections for either continuum bands (K-band, $12\mu\text{m}$, 2-10 keV and 14-195 keV) and narrow emission lines (mid-IR high ionization lines of $[\text{OIV}]$ and $[\text{NeV}]$ and optical $[\text{OIII}]5007\text{\AA}$) as well as for combinations of IR continuum and line emission. We find that a combination of continuum plus line emission accurately predicts the bolometric luminosity up to quasar luminosities ($10^{46} \text{ erg s}^{-1}$). This is the case of the $12\mu\text{m}$ continuum plus the $[\text{OIV}]26\mu\text{m}$ or the $[\text{NeV}]14.3\mu\text{m}$ mid-IR lines, and the $2.2\mu\text{m}$ continuum plus the $[\text{OIII}]5007\text{\AA}$ optical line. This result reflects the fact that the IR continuum includes a large fraction of (and is proportional to) the bolometric luminosity of the AGN, through both the nuclear continuum emission from hot dust/torus and the gas emission from the narrow-line region.

The *James Webb Space Telescope* (Gardner et al. 2006) will be able to measure this bolometric luminosity in virtually any AGN in the local Universe. For AGN at redshifts $z < 1$ the $[\text{NeV}]14.3\mu\text{m}$ line can also be used.

1 This research is based on ultraviolet observations made
 2 with the Galaxy Evolution Explorer, obtained from the
 3 MAST data archive at the Space Telescope Science In-
 4 stitute, which is operated by the Association of Universi-
 5 ties for Research in Astronomy, Inc., under NASA con-
 6 tract NAS 5–26555. This research has made use of the
 7 NASA/IPAC Extragalactic Database (NED), which is oper-
 8 ated by the Jet Propulsion Laboratory, California Institute
 9 of Technology, under contract with the National Aeronau-
 10 tics and Space Administration. JAFO acknowledges financial
 11 support by the Spanish Ministry of Science and Innovation
 12 (MCIN/AEI/10.13039/501100011033) and “ERDF A way
 13 of making Europe” through the grant PID2021-124918NB-
 14 C44; MCIN and the European Union – NextGenerationEU
 15 through the Recovery and Resilience Facility project ICTS-
 16 MRR-2021-03-CEFCA. We thank the anonymous referee for
 17 his/her constructive report that helped to improve the paper
 18 and correct an error in the X-ray fluxes conversion.

REFERENCES

- Akylas, A., & Georgantopoulos, I. 2009, *A&A*, 500, 999,
 doi: [10.1051/0004-6361/200811371](https://doi.org/10.1051/0004-6361/200811371)
- Asmus, D., Hönig, S. F., Gandhi, P., Smette, A., & Duschl, W. J.
 2014, *MNRAS*, 439, 1648, doi: [10.1093/mnras/stu041](https://doi.org/10.1093/mnras/stu041)
- Bassani, L., Dadina, M., Maiolino, R., et al. 1999, *ApJS*, 121, 473,
 doi: [10.1086/313202](https://doi.org/10.1086/313202)
- Bi, S., Feng, H., & Ho, L. C. 2020, *ApJ*, 900, 124,
 doi: [10.3847/1538-4357/aba761](https://doi.org/10.3847/1538-4357/aba761)
- Boissay, R., Ricci, C., & Paltani, S. 2016, *A&A*, 588, A70,
 doi: [10.1051/0004-6361/201526982](https://doi.org/10.1051/0004-6361/201526982)
- Braitto, V., Reeves, J. N., Della Ceca, R., et al. 2009, *A&A*, 504, 53,
 doi: [10.1051/0004-6361/200811516](https://doi.org/10.1051/0004-6361/200811516)
- Brightman, M., & Nandra, K. 2008, *MNRAS*, 390, 1241,
 doi: [10.1111/j.1365-2966.2008.13841.x](https://doi.org/10.1111/j.1365-2966.2008.13841.x)
- . 2011, *MNRAS*, 413, 1206,
 doi: [10.1111/j.1365-2966.2011.18207.x](https://doi.org/10.1111/j.1365-2966.2011.18207.x)
- Buchanan, C. L., Gallimore, J. F., O’Dea, C. P., et al. 2006, *AJ*,
 132, 401, doi: [10.1086/505022](https://doi.org/10.1086/505022)
- Cardamone, C. N., Moran, E. C., & Kay, L. E. 2007, *AJ*, 134,
 1263, doi: [10.1086/520801](https://doi.org/10.1086/520801)
- Cardelli, J. A., Clayton, G. C., & Mathis, J. S. 1989, *ApJ*, 345, 245,
 doi: [10.1086/167900](https://doi.org/10.1086/167900)
- Chen, S., Laor, A., & Behar, E. 2022, *MNRAS*, 515, 1723,
 doi: [10.1093/mnras/stac1891](https://doi.org/10.1093/mnras/stac1891)
- Conti, A., Bianchi, L., & Shiao, B. 2011, *Ap&SS*, 335, 329,
 doi: [10.1007/s10509-011-0667-0](https://doi.org/10.1007/s10509-011-0667-0)
- Corral, A., Georgantopoulos, I., Watson, M. G., et al. 2014, *A&A*,
 569, A71, doi: [10.1051/0004-6361/201424129](https://doi.org/10.1051/0004-6361/201424129)
- Cusumano, G., La Parola, V., Segreto, A., et al. 2010, *A&A*, 524,
 A64, doi: [10.1051/0004-6361/201015249](https://doi.org/10.1051/0004-6361/201015249)
- Della Ceca, R., Caccianiga, A., Severgnini, P., et al. 2008, *A&A*,
 487, 119, doi: [10.1051/0004-6361:20079319](https://doi.org/10.1051/0004-6361:20079319)
- Deluit, S. J. 2004, *A&A*, 415, 39,
 doi: [10.1051/0004-6361:20034593](https://doi.org/10.1051/0004-6361:20034593)
- Dudik, R. P., Satyapal, S., & Marcu, D. 2009, *ApJ*, 691, 1501,
 doi: [10.1088/0004-637X/691/2/1501](https://doi.org/10.1088/0004-637X/691/2/1501)
- Duras, F., Bongiorno, A., Ricci, F., et al. 2020, *A&A*, 636, A73,
 doi: [10.1051/0004-6361/201936817](https://doi.org/10.1051/0004-6361/201936817)
- Edelson, R. A., Malkan, M. A., & Rieke, G. H. 1987, *ApJ*, 321,
 233, doi: [10.1086/165627](https://doi.org/10.1086/165627)
- Elvis, M., Wilkes, B. J., McDowell, J. C., et al. 1994, *ApJS*, 95, 1,
 doi: [10.1086/192093](https://doi.org/10.1086/192093)
- Fazio, G. G., Hora, J. L., Allen, L. E., et al. 2004, *ApJS*, 154, 10,
 doi: [10.1086/422843](https://doi.org/10.1086/422843)
- Fernández-Ontiveros, J. A., & Muñoz-Darias, T. 2021, *MNRAS*,
 504, 5726, doi: [10.1093/mnras/stab1108](https://doi.org/10.1093/mnras/stab1108)
- Förster Schreiber, N. M., Roussel, H., Sauvage, M., &
 Charmandaris, V. 2004, *A&A*, 419, 501,
 doi: [10.1051/0004-6361:20040963](https://doi.org/10.1051/0004-6361:20040963)
- Gallimore, J. F., Yzaguirre, A., Jakoboski, J., et al. 2010, *ApJS*,
 187, 172, doi: [10.1088/0067-0049/187/1/172](https://doi.org/10.1088/0067-0049/187/1/172)
- Gardner, J. P., Mather, J. C., Clampin, M., et al. 2006, *SSRv*, 123,
 485, doi: [10.1007/s11214-006-8315-7](https://doi.org/10.1007/s11214-006-8315-7)
- Gaskell, C. M., Bartel, K., Deffner, J. N., & Xia, I. 2021, *MNRAS*,
 508, 6077, doi: [10.1093/mnras/stab2443](https://doi.org/10.1093/mnras/stab2443)

- Ghosh, K. K., & Soundararajaperumal, S. 1992, *MNRAS*, 259, 175, doi: [10.1093/mnras/259.1.175](https://doi.org/10.1093/mnras/259.1.175)
- Gorjian, V., Werner, M. W., Jarrett, T. H., Cole, D. M., & Ressler, M. E. 2004, *ApJ*, 605, 156, doi: [10.1086/381791](https://doi.org/10.1086/381791)
- Guainazzi, M., Matt, G., & Perola, G. C. 2005, *A&A*, 444, 119, doi: [10.1051/0004-6361:20053643](https://doi.org/10.1051/0004-6361:20053643)
- Heckman, T. M., Kauffmann, G., Brinchmann, J., et al. 2004, *ApJ*, 613, 109, doi: [10.1086/422872](https://doi.org/10.1086/422872)
- Helou, G., Madore, B. F., Schmitz, M., et al. 1991, in *Astrophysics and Space Science Library*, Vol. 171, Databases and On-line Data in Astronomy, ed. M. A. Albrecht & D. Egret, 89–106, doi: [10.1007/978-94-011-3250-3_10](https://doi.org/10.1007/978-94-011-3250-3_10)
- Hewitt, A., & Burbidge, G. 1991, *ApJS*, 75, 297, doi: [10.1086/191533](https://doi.org/10.1086/191533)
- Ho, L. C. 2008, *ARA&A*, 46, 475, doi: [10.1146/annurev.astro.45.051806.110546](https://doi.org/10.1146/annurev.astro.45.051806.110546)
- Hopkins, P. F., Richards, G. T., & Hernquist, L. 2007, *ApJ*, 654, 731, doi: [10.1086/509629](https://doi.org/10.1086/509629)
- Houck, J. R., Roellig, T. L., van Cleve, J., et al. 2004, *ApJS*, 154, 18, doi: [10.1086/423134](https://doi.org/10.1086/423134)
- Iyomoto, N., Fukazawa, Y., Nakai, N., & Ishihara, Y. 2001, *ApJL*, 561, L69, doi: [10.1086/324056](https://doi.org/10.1086/324056)
- Iyomoto, N., Makishima, K., Fukazawa, Y., et al. 1996, *PASJ*, 48, 231, doi: [10.1093/pasj/48.2.231](https://doi.org/10.1093/pasj/48.2.231)
- Kellermann, K. I., Sramek, R., Schmidt, M., Shaffer, D. B., & Green, R. 1989, *AJ*, 98, 1195, doi: [10.1086/115207](https://doi.org/10.1086/115207)
- Kennicutt, R. C., & Evans, N. J. 2012, *ARA&A*, 50, 531, doi: [10.1146/annurev-astro-081811-125610](https://doi.org/10.1146/annurev-astro-081811-125610)
- Krawczyk, C. M., Richards, G. T., Mehta, S. S., et al. 2013, *ApJS*, 206, 4, doi: [10.1088/0067-0049/206/1/4](https://doi.org/10.1088/0067-0049/206/1/4)
- Lagage, P. O., Pel, J. W., Authier, M., et al. 2004, *The Messenger*, 117, 12
- Lai, T. S. Y., Armus, L., U, V., et al. 2022, *ApJL*, 941, L36, doi: [10.3847/2041-8213/ac9ebf](https://doi.org/10.3847/2041-8213/ac9ebf)
- Levenson, N. A., Radomski, J. T., Packham, C., et al. 2009, *ApJ*, 703, 390, doi: [10.1088/0004-637X/703/1/390](https://doi.org/10.1088/0004-637X/703/1/390)
- Liu, Z., Merloni, A., Georgakakis, A., et al. 2016, *MNRAS*, 459, 1602, doi: [10.1093/mnras/stw753](https://doi.org/10.1093/mnras/stw753)
- Lusso, E., Comastri, A., Simmons, B. D., et al. 2012, *MNRAS*, 425, 623, doi: [10.1111/j.1365-2966.2012.21513.x](https://doi.org/10.1111/j.1365-2966.2012.21513.x)
- Lutz, D., Maiolino, R., Spoon, H. W. W., & Moorwood, A. F. M. 2004, *A&A*, 418, 465, doi: [10.1051/0004-6361:20035838](https://doi.org/10.1051/0004-6361:20035838)
- Lyu, J., Hao, L., & Li, A. 2014, *ApJL*, 792, L9, doi: [10.1088/2041-8205/792/1/L9](https://doi.org/10.1088/2041-8205/792/1/L9)
- Maiolino, R., Marconi, A., & Oliva, E. 2001a, *A&A*, 365, 37, doi: [10.1051/0004-6361:20000012](https://doi.org/10.1051/0004-6361:20000012)
- Maiolino, R., Marconi, A., Salvati, M., et al. 2001b, *A&A*, 365, 28, doi: [10.1051/0004-6361:20000177](https://doi.org/10.1051/0004-6361:20000177)
- Maiolino, R., Ruiz, M., Rieke, G. H., & Keller, L. D. 1995, *ApJ*, 446, 561, doi: [10.1086/175815](https://doi.org/10.1086/175815)
- Malkan, M. A., Jensen, L. D., Rodriguez, D. R., Spinoglio, L., & Rush, B. 2017, *ApJ*, 846, 102, doi: [10.3847/1538-4357/aa8302](https://doi.org/10.3847/1538-4357/aa8302)
- Malkan, M. A., & Sargent, W. L. W. 1982, *ApJ*, 254, 22, doi: [10.1086/159701](https://doi.org/10.1086/159701)
- Marconi, A., Risaliti, G., Gilli, R., et al. 2004, *MNRAS*, 351, 169, doi: [10.1111/j.1365-2966.2004.07765.x](https://doi.org/10.1111/j.1365-2966.2004.07765.x)
- Marinucci, A., Bianchi, S., Nicastro, F., Matt, G., & Goulding, A. D. 2012, *ApJ*, 748, 130, doi: [10.1088/0004-637X/748/2/130](https://doi.org/10.1088/0004-637X/748/2/130)
- Martocchia, S., Piconcelli, E., Zappacosta, L., et al. 2017, *A&A*, 608, A51, doi: [10.1051/0004-6361/201731314](https://doi.org/10.1051/0004-6361/201731314)
- Meléndez, M., Kraemer, S. B., Armentrout, B. K., et al. 2008, *ApJ*, 682, 94, doi: [10.1086/588807](https://doi.org/10.1086/588807)
- Mordini, S., Spinoglio, L., & Fernández-Ontiveros, J. A. 2021, *A&A*, 653, A36, doi: [10.1051/0004-6361/202140696](https://doi.org/10.1051/0004-6361/202140696)
- Morrissey, P., Conrow, T., Barlow, T. A., et al. 2007, *ApJS*, 173, 682, doi: [10.1086/520512](https://doi.org/10.1086/520512)
- Moshir, M., & et al. 1990, *IRAS Faint Source Catalogue*, 0
- Neugebauer, G., Habing, H. J., van Duinen, R., et al. 1984, *ApJL*, 278, L1, doi: [10.1086/184209](https://doi.org/10.1086/184209)
- Oh, K., Koss, M., Markwardt, C. B., et al. 2018, *ApJS*, 235, 4, doi: [10.3847/1538-4365/aaa7fd](https://doi.org/10.3847/1538-4365/aaa7fd)
- Osorio-Clavijo, N., González-Martín, O., Sánchez, S. F., et al. 2022, *MNRAS*, 510, 5102, doi: [10.1093/mnras/stab3752](https://doi.org/10.1093/mnras/stab3752)
- Osorio-Clavijo, N., Gonzalez-Martín, O., Sánchez, S. F., Guainazzi, M., & Cruz-González, I. 2023, *MNRAS*, 522, 5788, doi: [10.1093/mnras/stad1262](https://doi.org/10.1093/mnras/stad1262)
- Osterbrock, D. E., & Pogge, R. W. 1985, *ApJ*, 297, 166, doi: [10.1086/163513](https://doi.org/10.1086/163513)
- Pier, E. A., & Krolik, J. H. 1992, *ApJ*, 401, 99, doi: [10.1086/172042](https://doi.org/10.1086/172042)
- Pozzi, F., Vignali, C., Comastri, A., et al. 2010, *A&A*, 517, A11, doi: [10.1051/0004-6361/200913043](https://doi.org/10.1051/0004-6361/200913043)
- Prieto, M. A., Reunanen, J., Tristram, K. R. W., et al. 2010, *MNRAS*, 402, 724, doi: [10.1111/j.1365-2966.2009.15897.x](https://doi.org/10.1111/j.1365-2966.2009.15897.x)
- Pronik, V. I., & Chuvpov, K. K. 1972, *Astrophysics*, 8, 112, doi: [10.1007/BF01002159](https://doi.org/10.1007/BF01002159)
- Rees, M. J. 1984, *ARA&A*, 22, 471, doi: [10.1146/annurev.aa.22.090184.002351](https://doi.org/10.1146/annurev.aa.22.090184.002351)
- Reeves, J. N., & Turner, M. J. L. 2000, *MNRAS*, 316, 234, doi: [10.1046/j.1365-8711.2000.03510.x](https://doi.org/10.1046/j.1365-8711.2000.03510.x)
- Ricci, C., Trakhtenbrot, B., Koss, M. J., et al. 2017, *ApJS*, 233, 17, doi: [10.3847/1538-4365/aa96ad](https://doi.org/10.3847/1538-4365/aa96ad)
- Richards, G. T., Lacy, M., Storrie-Lombardi, L. J., et al. 2006, *ApJS*, 166, 470, doi: [10.1086/506525](https://doi.org/10.1086/506525)
- Rieke, G. H. 1978, *ApJ*, 226, 550, doi: [10.1086/156639](https://doi.org/10.1086/156639)
- Rigby, J. R., Diamond-Stanic, A. M., & Aniano, G. 2009, *ApJ*, 700, 1878, doi: [10.1088/0004-637X/700/2/1878](https://doi.org/10.1088/0004-637X/700/2/1878)
- Rivers, E., Markowitz, A., & Rothschild, R. 2013, *ApJ*, 772, 114, doi: [10.1088/0004-637X/772/2/114](https://doi.org/10.1088/0004-637X/772/2/114)

- Roche, P. F., & Aitken, D. K. 1984, *MNRAS*, 208, 481, doi: [10.1093/mnras/208.3.481](https://doi.org/10.1093/mnras/208.3.481)
- Rush, B., Malkan, M. A., & Spinoglio, L. 1993, *ApJS*, 89, 1, doi: [10.1086/191837](https://doi.org/10.1086/191837)
- Saade, M. L., Brightman, M., Stern, D., Malkan, M. A., & García, J. A. 2022, *ApJ*, 936, 162, doi: [10.3847/1538-4357/ac88cf](https://doi.org/10.3847/1538-4357/ac88cf)
- Saccheo, I., Bongiorno, A., Piconcelli, E., et al. 2023, *A&A*, 671, A34, doi: [10.1051/0004-6361/202244296](https://doi.org/10.1051/0004-6361/202244296)
- Sanders, D. B., Phinney, E. S., Neugebauer, G., Soifer, B. T., & Matthews, K. 1989, *ApJ*, 347, 29, doi: [10.1086/168094](https://doi.org/10.1086/168094)
- Schmidt, M., & Green, R. F. 1983, *ApJ*, 269, 352, doi: [10.1086/161048](https://doi.org/10.1086/161048)
- Scoville, N., Aussel, H., Benson, A., et al. 2007, *ApJS*, 172, 150, doi: [10.1086/516751](https://doi.org/10.1086/516751)
- Shang, Z., Brotherton, M. S., Wills, B. J., et al. 2011, *ApJS*, 196, 2, doi: [10.1088/0067-0049/196/1/2](https://doi.org/10.1088/0067-0049/196/1/2)
- Shao, Z., Jiang, B. W., & Li, A. 2017, *ApJ*, 840, 27, doi: [10.3847/1538-4357/aa6ba4](https://doi.org/10.3847/1538-4357/aa6ba4)
- Spinoglio, L., Fernández-Ontiveros, J. A., & Malkan, M. A. 2022, *ApJ*, 941, 46, doi: [10.3847/1538-4357/ac9da2](https://doi.org/10.3847/1538-4357/ac9da2)
- Spinoglio, L., & Malkan, M. A. 1989, *ApJ*, 342, 83, doi: [10.1086/167577](https://doi.org/10.1086/167577)
- Spinoglio, L., Malkan, M. A., Rush, B., Carrasco, L., & Recillas-Cruz, E. 1995, *ApJ*, 453, 616, doi: [10.1086/176425](https://doi.org/10.1086/176425)
- Spoon, H. W. W., Marshall, J. A., Houck, J. R., et al. 2007, *ApJL*, 654, L49, doi: [10.1086/511268](https://doi.org/10.1086/511268)
- Sun, W.-H., & Malkan, M. A. 1989, *ApJ*, 346, 68, doi: [10.1086/167986](https://doi.org/10.1086/167986)
- Tan, Y., Wang, J. X., Shu, X. W., & Zhou, Y. 2012, *ApJL*, 747, L11, doi: [10.1088/2041-8205/747/1/L11](https://doi.org/10.1088/2041-8205/747/1/L11)
- Tanimoto, A., Ueda, Y., Odaka, H., Yamada, S., & Ricci, C. 2022, *ApJS*, 260, 30, doi: [10.3847/1538-4365/ac5f59](https://doi.org/10.3847/1538-4365/ac5f59)
- Thean, A., Pedlar, A., Kukula, M. J., Baum, S. A., & O’Dea, C. P. 2000, *MNRAS*, 314, 573, doi: [10.1046/j.1365-8711.2000.03401.x](https://doi.org/10.1046/j.1365-8711.2000.03401.x)
- Thompson, A. R., Clark, B. G., Wade, C. M., & Napier, P. J. 1980, *ApJS*, 44, 151, doi: [10.1086/190688](https://doi.org/10.1086/190688)
- Tommasin, S., Spinoglio, L., Malkan, M. A., & Fazio, G. 2010, *ApJ*, 709, 1257, doi: [10.1088/0004-637X/709/2/1257](https://doi.org/10.1088/0004-637X/709/2/1257)
- Vasudevan, R. V., & Fabian, A. C. 2007, *MNRAS*, 381, 1235, doi: [10.1111/j.1365-2966.2007.12328.x](https://doi.org/10.1111/j.1365-2966.2007.12328.x)
- Vasylenko, A. A. 2018, *Ap&SS*, 363, 228, doi: [10.1007/s10509-018-3447-2](https://doi.org/10.1007/s10509-018-3447-2)
- Veron-Cetty, M. P., & Veron, P. 1991, *European Southern Observatory Scientific Report*, 10, 1
- Wall, R. E., Kilic, M., Bergeron, P., et al. 2019, *MNRAS*, 489, 5046, doi: [10.1093/mnras/stz2506](https://doi.org/10.1093/mnras/stz2506)
- Walton, D. J., Baloković, M., Fabian, A. C., et al. 2021, *MNRAS*, 506, 1557, doi: [10.1093/mnras/stab1290](https://doi.org/10.1093/mnras/stab1290)
- Wu, Y., Charmandaris, V., Huang, J., Spinoglio, L., & Tommasin, S. 2009, *ApJ*, 701, 658, doi: [10.1088/0004-637X/701/1/658](https://doi.org/10.1088/0004-637X/701/1/658)
- Xie, Y., & Ho, L. C. 2019, *ApJ*, 884, 136, doi: [10.3847/1538-4357/ab4200](https://doi.org/10.3847/1538-4357/ab4200)
- Yamada, S., Ueda, Y., Herrera-Endoqui, M., et al. 2023, *ApJS*, 265, 37, doi: [10.3847/1538-4365/acb349](https://doi.org/10.3847/1538-4365/acb349)
- Zhou, X.-L., & Zhang, S.-N. 2010, *ApJL*, 713, L11, doi: [10.1088/2041-8205/713/1/L11](https://doi.org/10.1088/2041-8205/713/1/L11)

Table 8. The AGN sample: coordinates, redshift, types and radio loudness (flagged as RL).(Note: This table is the full version of Table 1 and will be published in electronic form).

n. Name	R.A. (J2000.0)	Dec. (J2000.0)	z	Type	Radio
(1)	(2)	(3)	(4)	(5)	(6)
1 MRK0335	00:06:19.5	+20:12:10	0.0258	Sy1	
2 NGC34=Mrk938=N17	00:11:06.5	-12:06:26	0.0196	Sy2	
3 IRASF00198-7926	00:21:57.0	-79:10:14	0.0728	Sy2	
4 ESO012-G021	00:40:47.8	-79:14:27	0.0300	Sy1	
5 NGC0262=MRK348	00:48:47.1	+31:57:25	0.0150	HBL	RL
6 Izw001=UGC00545	00:53:34.9	+12:41:36	0.0611	Sy1	
7 IRASF00521-7054	00:53:56.2	-70:38:03	0.0689	HBL	
8 ESO541-IG012	01:02:17.5	-19:40:09	0.0566	Sy2	
9 NGC0424	01:11:27.5	-38:05:01	0.0118	HBL CT	
10 NGC0526A	01:23:54.2	-35:03:56	0.0191	Sy1	
11 NGC0513	01:24:26.8	+33:47:58	0.0195	HBL	
12 IRASF01475-0740	01:50:02.7	-07:25:48	0.0177	HBL	RL
13 MRK1034NED02	02:23:22.0	+32:11:50	0.0338	Sy1	
14 ESO545-G013	02:24:40.2	-19:08:27	0.0337	Sy1	
15 NGC0931=Mrk1040	02:28:14.5	+31:18:42	0.0167	Sy1	
16 NGC1068	02:42:40.7	-00:00:48	0.0038	HBL CT	
17 NGC1056	02:42:48.5	+28:34:29	0.0052	Sy2	
18 NGC1097	02:46:19.1	-30:16:28	0.0042	LIN	
19 NGC1125	02:51:40.4	-16:39:02	0.0109	HBL CT	
20 NGC1144	02:55:12.2	-00:11:01	0.0288	Sy2	
21 MCG-02-08-039	03:00:29.8	-11:24:59	0.0299	HBL	
22 NGC1194	03:03:49.2	-01:06:12	0.0136	Sy1 CT	
23 NGC1241	03:11:14.7	-08:55:20	0.0135	Sy2	
24 NGC1320	03:24:48.7	-03:02:33	0.0089	Sy2	
25 NGC1365	03:33:36.4	-36:08:25	0.0055	Sy1	
26 NGC1386	03:36:45.4	-35:59:57	0.0029	HBL CT	
27 IRASF03362-1642	03:38:34.5	-16:32:16	0.0369	Sy2	
28 IRASF03450+0055	03:47:40.2	+01:05:14	0.0310	Sy1	RL
29 NGC1566	04:20:00.6	-54:56:17	0.0050	Sy1	
30 3C120	04:33:11.1	+05:21:16	0.0330	Sy1	RL
31 MRK0618	04:36:22.2	-10:22:34	0.0356	Sy1	
32 IRASF04385-0828	04:40:54.9	-08:22:22	0.0151	HBL	
33 NGC1667	04:48:37.1	-06:19:12	0.0152	Sy2	
34 ESO033-G002	04:55:59.6	-75:32:27	0.0181	Sy2	
35 ESO362-G018	05:19:35.5	-32:39:30	0.0124	Sy1	
36 IRASF05189-2524	05:21:01.4	-25:21:45	0.0426	HBL	
37 ESO253-G003	05:25:18.3	-46:00:20	0.0425	Sy2	
38 IRASF05563-3820	05:58:02.0	-38:20:05	0.0339	Sy1	
39 MRK0006	06:52:12.2	+74:25:37	0.0188	Sy1	
40 MRK0009	07:36:57.0	+58:46:13	0.0399	Sy1	
41 MRK0079	07:42:32.8	+49:48:35	0.0222	Sy1	
42 IRASF07599+6508	08:04:30.5	+64:59:53	0.1483	Sy1	
43 NGC2639	08:43:38.0	+50:12:20	0.0111	Sy1	
44 IRASF08572+3915	09:00:25.3	+39:03:54	0.0583	Sy2/LIN	
45 MRK0704	09:18:26.0	+16:18:19	0.0292	Sy1	

Table 8. continued.

n. Name	R.A. (J2000.0)	Dec. (J2000.0)	z	Type	Radio
(1)	(2)	(3)	(4)	(5)	(6)
46 UGC05101	09:35:51.6	+61:21:11	0.0394	LIN CT	RL
47 NGC2992	09:45:42.0	-14:19:35	0.0077	Sy1	
48 MRK1239	09:52:19.1	-01:36:43	0.0199	Sy1	
49 M81	09:55:33.2	+69:03:55	-0.00013	LIN	
50 3C234	10:01:49.5	+28:47:09	0.1849	Sy1	RL
51 NGC3079	10:01:57.8	+55:40:47	0.0037	Sy2 CT	
52 NGC3227	10:23:30.6	+19:51:54	0.0039	Sy1	
53 NGC3511	11:03:23.7	-23:05:11	0.0037	Sy1	
54 NGC3516	11:06:47.5	+72:34:07	0.0088	Sy1	
55 MCG+00-29-023	11:21:12.2	-02:59:03	0.0249	Sy2	
56 NGC3660	11:23:32.2	-08:39:30	0.0123	Sy2	
57 NGC3982	11:56:28.1	+55:07:31	0.0037	HBL	
58 NGC4051	12:03:09.6	+44:31:53	0.0023	Sy1	
59 UGC07064	12:04:43.3	+31:10:38	0.0250	HBL	
60 NGC4151	12:10:32.6	+39:24:21	0.0033	Sy1	
61 NGC4253=MRK766	12:18:26.5	+29:48:46	0.0129	Sy1	
62 NGC4388	12:25:46.7	+12:39:41	0.0084	HBL	
63 3C273	12:29:06.7	+02:03:09	0.1583	Sy1	RL
64 NGC4501=M88	12:31:59.0	+14:25:10	0.0076	Sy2	
65 NGC4579=M58	12:37:43.5	+11:49:05	0.0051	LIN	
66 NGC4593	12:39:39.4	-05:20:39	0.0090	Sy1	
67 NGC4594=M104	12:39:58.8	-11:37:28	0.0034	LIN	
68 NGC4602	12:40:36.5	-05:07:55	0.0085	Sy1	
69 TO1238-36=I3639	12:40:52.9	-36:45:22	0.0109	HBL CT	
70 M-2-33-34=N4748	12:52:12.4	-13:24:54	0.0146	Sy1	
71 MRK0231	12:56:14.2	+56:52:25	0.0422	Sy1	RL
72 NGC4922	13:01:24.5	+29:18:30	0.0236	Sy2	
73 NGC4941	13:04:13.1	-05:33:06	0.0037	Sy2	
74 NGC4968	13:07:06.0	-23:40:43	0.0099	Sy2	
75 NGC5005	13:10:56.2	+37:03:33	0.0032	LIN	
76 NGC5033	13:13:27.5	+36:35:38	0.0029	Sy1	
77 MCG-03-34-064	13:22:24.4	-16:43:43	0.0165	HBL	
78 NGC5135	13:25:44.0	-29:50:02	0.0137	Sy2 CT	
79 NGC5194=M51A	13:29:52.3	+47:11:54	0.0015	Sy2	
80 MCG-06-30-015	13:35:53.7	-34:17:45	0.0077	Sy1	
81 IRASF13349+2438	13:37:18.7	+24:23:03	0.1076	Sy1	
82 NGC5256=Mrk266	13:38:17.8	+48:16:35	0.0279	Sy2	
83 MRK0273	13:44:42.1	+55:53:13	0.0378	LIN	
84 IC4329A	13:49:19.3	-30:18:34	0.0161	Sy1	
85 NGC5347	13:53:17.8	+33:29:27	0.0078	HBL CT	
86 MRK0463=UGC8850	13:56:02.9	+18:22:19	0.0504	HBL	
87 NGC5506	14:13:14.8	-03:12:27	0.0062	Sy2	
88 NGC5548	14:17:59.5	+25:08:12	0.0172	Sy1	
89 MRK0817	14:36:22.1	+58:47:39	0.0315	Sy1	
90 IRASF15091-2107	15:11:59.8	-21:19:02	0.0446	Sy1	
91 NGC5929	15:26:06.1	+41:40:14	0.0083	HBL	

Table 8. continued.

n. Name	R.A. (J2000.0)	Dec. (J2000.0)	z	Type	Radio
(1)	(2)	(3)	(4)	(5)	(6)
92 NGC5953	15:34:32.3	+15:11:42	0.0066	nSy	
93 ARP220=UGC9913	15:34:57.3	+23:30:12	0.0181	Sy2	
94 N5995=M-2-40-4	15:48:24.9	-13:45:28	0.0252	HBL	
95 IRASF15480-0344	15:50:41.5	-03:53:18	0.0303	HBL	
96 ESO141-G055	19:21:14.3	-58:40:13	0.0371	Sy1	
97 IRASF19254-7245	19:31:22.5	-72:39:20	0.0617	HBL CT	RL
98 NGC6810	19:43:34.1	-58:39:21	0.0068	LIN	
99 NGC6860	20:08:46.1	-61:05:56	0.0149	Sy1	
100 NGC6890	20:18:18.1	-44:48:23	0.0081	Sy2	
101 MRK0509	20:44:09.7	-10:43:25	0.0344	Sy1	
102 IC5063	20:52:02.0	-57:04:09	0.0113	HBL	
103 MRK0897	21:07:45.8	+03:52:40	0.0263	Sy2	
104 NGC7130	21:48:19.5	-34:57:09	0.0162	Sy2 CT	
105 NGC7172	22:02:01.7	-31:52:18	0.0087	Sy2 CT	
106 IRASF22017+0319	22:04:19.2	+03:33:50	0.0611	HBL	
107 NGC7213	22:09:16.2	-47:10:00	0.0058	LIN	
108 3C445	22:23:49.6	-02:06:12	0.0562	Sy1	RL
109 NGC7314	22:35:46.0	-26:03:02	0.0048	HBL	
110 MCG+03-58-007	22:49:36.9	-19:16:24	0.0315	HBL	
111 NGC7469	23:03:15.6	+08:52:26	0.0163	Sy1	
112 NGC7496	23:09:47.2	-43:25:40	0.0055	Sy2	
113 NGC7582	23:18:23.5	-42:22:14	0.0053	Sy2 CT	
114 NGC7590	23:18:55.0	-42:14:17	0.0053	Sy2	
115 NGC7603	23:18:56.6	+00:14:38	0.0295	Sy1	
116 NGC7674	23:27:56.7	+08:46:45	0.0289	HBL CT	
117 CGCG381-051	23:48:41.3	+02:14:21	0.0307	Sy2	

Table 9. Low frequency nuclear photometry of the AGN sample. (Note: This table is the full version of Table 2 and will be published in electronic form).

n. Name	z	Type	F(8.4GHz)	F(12 μ m)	F(12 μ m)	R12	F(7.0 μ m)	F(5.8 μ m)	F(4.5 μ m)	F(K)
			VLA	VLT	IRS	IRS/VLT	IRSCOR	IRSCOR	IRSCOR	Keck/2MASS
(1)	(2)	(3)	(4)	(5)	(6)	(7)	(8)	(9)	(10)	(11)
1 MRK0335	0.0258	Sy1	2.1	151.†	190.52	1.26	100.32	77.91	67.53	16.00
2 NGC34=Mrk938=N17	0.0196	Sy2	14.5	57.8	210.38	3.64	—	—	—	5.25
3 IRASF00198-7926	0.0728	Sy2	—	—	—	—	—	—	—	2.15
4 ESO012-G021	0.0300	Sy1	—	—	115.67	—	—	—	—	5.10
5 NGC0262=MRK348	0.0150	HBL	346.0	117.†	304.83	2.61	47.89	37.73	28.48	2.17
6 IZw001=UGC00545	0.0611	Sy1	0.9	425.9	—	—	—	—	—	18.40
7 IRASF00521-7054	0.0689	HBL	—	—	—	—	—	—	—	7.24
8 ESO541-IG012	0.0566	Sy2	0.8	—	—	—	—	—	—	6.85
9 NGC0424	0.0118	HBL	11.9	736.2	979.81	1.33	415.77	310.84	226.16	24.90
10 NGC0526A	0.0191	Sy1	7.1	236.4	239.51	1.01	101.73	97.91	82.61	8.79
11 NGC0513	0.0195	HBL	1.2	—	91.37	—	—	—	—	1.51
12 IRASF01475-0740	0.0177	HBL	129.8	—	197.32	—	—	—	—	0.66
13 MRK1034NED02	0.0338	Sy1	11.6	—	—	—	—	—	—	—
14 ESO545-G013	0.0337	Sy1	0.2	—	—	—	—	—	—	1.53
15 NGC0931=Mrk1040	0.0167	Sy1	<0.4	212.†	453.62	2.14	106.49	95.99	66.69	7.11
16 NGC1068	0.0038	HBL	30.3	10205.8	—	—	—	—	—	196.00
17 NGC1056	0.0052	NSy	0.6	—	102.82	—	—	—	—	—
18 NGC1097	0.0042	LIN	3.1	16.8	448.86	26.72	—	—	—	1.22
19 NGC1125	0.0109	HBL	3.0	—	136.08	—	—	—	—	—
20 NGC1144	0.0288	Sy2	2.3	25.1	95.73	3.81	—	—	—	—
21 MCG-02-08-039	0.0299	HBL	<0.3	230.7	199.59	0.87	60.46	26.01	16.53	0.29
22 NGC1194	0.0136	Sy1	0.9	276.6	272.17	0.98	167.06	139.23	81.20	1.46
23 NGC1241	0.0135	Sy2	6.8	—	65.32	—	—	—	—	—
24 NGC1320=MRK607	0.0089	Sy2	1.0	230.	408.25	1.77	89.86	65.97	41.41	2.40
25 NGC1365	0.0055	Sy1	2.0	360.7	1406.21	3.90	—	—	—	40.20
26 NGC1386	0.0029	HBL	6.8	299.3	522.57	1.75	121.18	90.09	56.59	0.39
27 IRASF03362-1642	0.0369	SY2	1.5	148.†	—	—	—	—	—	—
28 IRASF03450+0055	0.0310	Sy1	6.8	98.†	250.40	2.56	42.04	36.08	29.04	9.91
29 NGC1566	0.0050	Sy1	—	59.3	149.69	2.52	32.77	30.38	26.07	4.61
30 3C120	0.0330	Sy1	2105.2	266.0	—	—	—	—	—	12.90
31 MRK0618	0.0356	Sy1	2.9	—	—	—	—	—	—	9.20
32 IRASF04385-0828	0.0151	HBL	6.0	161.†	498.98	3.10	—	—	—	4.70
33 NGC1667	0.0152	Sy2	1.5	5.7	74.98	13.15	—	—	—	0.89
34 ESO033-G002	0.0181	Sy2	—	174.2	250.40	1.44	76.43	54.82	41.81	4.05
35 ESO362-G018	0.0124	Sy1	1.0	157.5	157.25	1.00	53.43	57.19	31.85	1.94
36 IRASF05189-2524	0.0426	HBL	6.9	650.9	—	—	—	—	—	14.30
37 ESO253-G003	0.0425	Sy2	<2.4	—	—	—	—	—	—	3.08
38 IRASF05563-3820	0.0339	Sy1	2.6	426.5	—	—	—	—	—	21.70
39 MRK0006	0.0188	Sy1	27.9	160.†	244.95	1.53	75.08	68.52	66.30	18.00
40 MRK0009	0.0399	Sy1	0.6	58.†	—	—	—	—	—	8.95
41 MRK0079	0.0222	Sy1	0.8	237.†	340.21	1.44	124.72	101.78	75.44	6.37
42 IRASF07599+6508	0.1483	Sy1	5.8	180.†	—	—	—	—	—	13.20

Table 9. continued.

n. Name	z	Type	F(8.4GHz)	F(12 μ m)	F(12 μ m)	R12	F(7.0 μ m)	F(5.8 μ m)	F(4.5 μ m)	F(K)
			VLA	VLT	IRS	IRS/VLT	IRSCOR	IRSCOR	IRSCOR	Keck/2MASS
(1)	(2)	(3)	(4)	(5)	(6)	(7)	(8)	(9)	(10)	(11)
43 NGC2639	0.0111	Sy1	118.0	—	41.33	—	—	—	—	—
44 IRASF08572+3915	0.0583	LIN	3.8	602.1	—	—	—	—	—	0.96
45 MRK0704	0.0292	Sy1	0.9	297.†	367.43	1.24	154.57	106.70	86.73	9.91
46 UGC05101	0.0394	LIN	45.1	227.0	—	—	—	—	—	6.25
47 NGC2992	0.0077	Sy1	5.5	191.2	443.85	2.32	56.91	62.38	45.79	4.36
48 MRK1239	0.0199	Sy1	10.5	574.3	843.73	1.47	282.48	234.22	188.55	21.50
49 M81=NGC3031	0.00014	LIN	221.0	136.9	—	—	—	—	—	6.31
50 3C234	0.1849	Sy1	38.8	110.†	—	—	—	—	—	1.72
51 NGC3079	0.0037	Sy2	93.3	—	244.95	—	—	—	—	13.70
52 NGC3227	0.0039	Sy1	12.2	200.5	468.97	2.34	75.77	66.01	41.81	11.30
53 NGC3511	0.0037	Sy1	<0.3	—	54.43	—	—	—	—	—
54 NGC3516	0.0088	Sy1	3.1	230.‡	381.04	1.66	117.89	85.77	70.98	6.02
55 MCG+00-29-023	0.0249	Sy2	<0.3	58.†	160.44	2.77	18.39	19.88	8.97	1.98
56 NGC3660	0.0123	Sy2	<0.3	25.7	35.31	1.37	8.73	6.04	7.13	0.27
57 NGC3982	0.0037	HBL	0.8	26.5	89.43	3.37	—	—	—	—
58 NGC4051	0.0023	Sy1	0.6	464.0	508.05	1.09	218.00	151.79	109.41	6.85
59 UGC07064	0.0250	HBL	<0.3	—	102.06	—	—	—	—	1.72
60 NGC4151	0.0033	Sy1	10.9	1287.4	2041.28	1.59	411.51	328.46	243.44	21.10
61 NGC4253=MRK766	0.0129	Sy1	8.7	253.†	381.04	1.51	86.45	69.65	56.04	11.30
62 NGC4388	0.0084	HBL	1.4	187.8	520.15	2.77	75.55	59.46	29.64	1.69
63 3C273	0.1583	Sy1	41725.0	289.5	—	—	—	—	—	23.80
64 NGC4501=M88	0.0076	Sy2	<0.2	3.7	55.16	14.91	—	—	—	0.47
65 NGC4579=M58	0.0051	LIN	36.5	74.6	93.43	1.25	51.09	65.31	73.22	—
66 NGC4593	0.0090	Sy1	1.9	227.4	399.18	1.76	126.09	92.97	76.22	6.08
67 NGC4594=M104	0.0034	LIN	86.6	4.4	103.92	23.62	—	—	—	—
68 NGC4602	0.0085	Sy1	<0.2	—	41.24	—	—	—	—	—
69 TOL1238-36=I3639	0.0109	HBL	2.3	386.1	497.68	1.29	95.84	69.59	39.10	2.51
70 M-2-33-34=N4748	0.0146	Sy1	1.5	—	84.13	—	—	—	—	2.44
71 MRK0231	0.0422	Sy1	234.5	1235.†	—	—	—	—	—	46.60
72 NGC4922	0.0236	Sy2	<0.3	162.†	—	—	—	—	—	—
73 NGC4941	0.0037	Sy2	2.1	76.1	92.12	1.21	27.28	23.46	21.89	21.10
74 NGC4968	0.0099	Sy2	2.1	250.†	367.43	1.47	67.55	48.44	29.60	1.38
75 NGC5005	0.0032	LIN	8.8	7.0	149.69	21.38	—	—	—	6.79
76 NGC5033	0.0029	Sy1	2.1	15.9	149.25	9.39	—	—	—	3.60
77 MCG-03-34-064	0.0165	HBL	42.2	530.6	—	—	—	—	—	0.66
78 NGC5135	0.0137	Sy2	<2.3	132.0	349.63	2.65	43.09	14.12	11.25	3.19
79 NGC5194=M51A	0.0015	Sy2	0.5	25.8	—	—	—	—	—	4.25
80 MCG-06-30-015	0.0077	Sy1	<0.3	340.8	344.75	1.01	180.99	155.50	126.34	12.20
81 IRASF13349+2438	0.1076	Sy1	4.7	476.4	—	—	—	—	—	13.90
82 NGC5256=Mrk266	0.0279	Sy2	2.9	72.†	108.87	1.51	17.64	28.64	11.77	1.91
83 MRK0273	0.0378	LIN	30.5	79.†	—	—	—	—	—	3.53
84 IC4329A	0.0161	Sy1	10.4	1157.7	1197.55	1.03	928.28	467.70	369.68	20.10

Table 9. continued.

n. Name	z	Type	F(8.4GHz)	F(12 μ m)	F(12 μ m)	R12	F(7.0 μ m)	F(5.8 μ m)	F(4.5 μ m)	F(K)
			VLA	VLT	IRS	IRS/VLT	IRSCOR	IRSCOR	IRSCOR	Keck/2MASS
(1)	(2)	(3)	(4)	(5)	(6)	(7)	(8)	(9)	(10)	(11)
85 NGC5347	0.0078	HBL	0.8	278.0	337.49	1.21	74.48	50.66	30.64	1.96
86 MRK0463=UGC8850	0.0504	HBL	43.6	395.†	—	—	—	—	—	16.00
87 NGC5506	0.0062	Sy2	67.6	870.8	1290.86	1.48	519.14	494.00	383.37	42.10
88 NGC5548	0.0172	Sy1	2.2	123.8	299.39	2.42	39.63	31.14	21.42	3.22
89 MRK0817	0.0315	Sy1	2.8	234.†	299.39	1.28	84.80	81.21	58.54	9.04
90 IRASF15091-2107	0.0446	Sy1	7.8	145.†	—	—	—	—	—	8.63
91 NGC5929	0.0083	HBL	9.1	—	24.68	—	—	—	—	—
92 NGC5953	0.0066	nSy	1.1	<29.5	174.47	>5.91	—	—	—	—
93 ARP220=UGC9913	0.0181	Sy2	63.0	142.†	—	—	—	—	—	3.25
94 N5995=M-2-40-4	0.0252	HBL	2.4	332.4	482.13	1.45	176.72	112.52	88.94	13.90
95 IRASF15480-0344	0.0303	HBL	12.4	102.†	217.74	2.13	30.50	17.05	11.52	1.87
96 ESO141-G055	0.0371	Sy1	—	148.7	—	—	—	—	—	11.20
97 IRASF19254-7245	0.0617	HBL	—	221.5	—	—	—	—	—	1.94
98 NGC6810	0.0068	SB	—	44.4	518.94	11.69	—	—	—	2.96
99 NGC6860	0.0149	Sy1	—	206.1	217.74	1.06	123.24	102.04	71.56	6.98
100 NGC6890	0.0081	Sy2	0.5	116.6	174.19	1.49	52.79	35.21	24.90	1.74
101 MRK0509	0.0344	Sy1	2.2	256.4	—	—	—	—	—	16.90
102 IC5063	0.0113	HBL	230.	820.6	1052.39	1.28	329.95	170.84	96.92	3.63
103 MRK0897	0.0263	Sy2	3.5	8.2	97.98	11.95	—	—	—	8.55
104 NGC7130	0.0162	Sy2	18.1	104.5	319.80	3.06	—	—	—	0.96
105 NGC7172	0.0087	Sy2	4.7	185.0	217.74	1.18	108.32	154.89	107.56	8.87
106 IRASF22017+0319	0.0611	HBL	0.2	137.†	—	—	—	—	—	3.87
107 NGC7213	0.0058	LIN	183.8	203.3	293.94	1.45	76.81	94.75	95.17	6.19
108 3C445	0.0562	Sy1	58.1	180.0	—	—	—	—	—	—
109 NGC7314	0.0048	HBL	0.7	61.5	122.48	1.99	15.88	16.37	13.91	3.02
110 MCG+03-58-007	0.0315	HBL	0.4	200.†	293.94	1.47	91.05	79.00	61.31	7.18
111 NGC7469	0.0163	Sy1	16.0	1173.8	1001.59	0.85	308.16	317.36	176.85	13.90
112 NGC7496	0.0055	Sy2	3.8	169.5	199.31	1.18	33.81	40.40	17.86	0.71
113 NGC7582	0.0053	Sy2	51.8	443.2	952.60	2.15	186.13	240.12	132.50	42.50
114 NGC7590	0.0053	Sy2	<0.2	<10.6	60.48	>5.71	—	—	—	16.30
115 NGC7603	0.0295	Sy1	3.3	102.†	281.24	2.76	72.01	64.88	56.76	15.40
116 NGC7674	0.0289	HBL	12.8	382.2	533.45	1.40	139.15	105.68	67.56	8.39
117 CGCG381-051	0.0307	Sy2	0.6	68.†	113.06	1.66	15.59	9.38	5.05	0.67

Notes. The columns give for each AGN in the sample: (1) name; (2) AGN type: Sy1 = Seyfert type 1; Sy2 = Seyfert type 2; HBL = Hidden Broad Line Region AGN; LIN = LINER galaxy; (3) redshift; (4) 8.4GHz nuclear flux density (Thean et al. 2000); (5) VLT-VISIR subarcsecond nuclear 12 μ m flux density from Asmus et al. (2014), †: for these 27 AGN, no sub-arcsec detection is available at 12 μ m, we used instead the 10.8 μ m flux density measured with a 1.5'' aperture, from Gorjian et al. (2004), ‡: for these 2 objects, we use the 10.6 μ m flux density measured with a 3.9'' aperture, from Rieke (1978); (6) *Spitzer*-IRS 12 μ m continuum flux density as derived from Gallimore et al. (2010), using the [NeII]12.8 μ m line flux and the correspondent equivalent width; (7) R12 is the ratio between the *Spitzer*-IRS continuum and the VLT-VISIR subarcsecond flux density at 12 μ m; (8) *Spitzer*-IRS 7 μ m continuum flux density as derived from Gallimore et al. (2010), using the [ArII]7.0 μ m line flux and the correspondent equivalent width corrected for R12; (9) *Spitzer*-IRAC 5.8 μ m flux density corrected for R12; (10) *Spitzer*-IRAC 4.5 μ m flux density corrected for R12; (11) 2.2 μ m nuclear emission derived from Keck/2MASS (Spinoglio et al. 2022).

Table 10. High frequency nuclear photometry of the AGN sample (**Note: This table is the full version of Table 3 and will be published in electronic form.**)

n. Name	z	Type	F_{NUV}	F_{FUV}	$F_{2-10keV}$	$F_{14-195keV}$	F_{bol}	L_{bol}	Γ_1	Γ_2	Ref ₁	Ref ₂	Flag
(1)	(2)	(3)	(4)	(5)	(6)	(7)	(8)	(9)	(10)	(11)	(12)	(13)	(14)
			(mJy)		$(10^{-12} \text{ergs}^{-1} \text{cm}^{-2})$			$\log(\text{erg s}^{-1})$					
1 MRK0335	0.0258	Sy1	3.517	1.880	16.69	15.97	402.72	44.751	2.03	2.31	(1)	(32)	
2 NGC34=Mrk938=N17	0.0196	Sy2	0.072	0.246	2.35	—	105.68	43.927	1.9	—	(2)		
3 IRASF00198-7926	0.0728	Sy2	—	0.133	—	21.80	148.25	45.248	—	—		(33)	
4 ESO012-G021	0.0300	Sy1	—	—	5.51	4.00	47.86	43.959	1.21	—	(3)	(34)	
5 NGC0262=MRK348	0.0150	HBL	0.089	0.143	37.45	144.81	642.69	44.475	1.68	1.90	(1)	(32)	
6 IZw001=UGC00545	0.0611	Sy1	1.108	2.196	6.51	—	516.42	45.631	2.16	—	(4)		
7 IRASF00521-7054	0.0689	HBL	0.011	0.038	3.46	—	83.37	44.948	1.80	—	(5)		
8 ESO541-IG012	0.0566	Sy2	0.047	—	—	—	> 68.23	> 44.682	—	—			L
9 NGC0424	0.0118	HBL	0.103	0.212	28.40	21.51	814.70	44.368	2.11	1.91	(6)	(32)	
10 NGC0526A	0.0191	Sy1	0.084	0.127	23.10	73.91	468.81	44.551	1.51	1.93	(1)	(32)	
11 NGC0513	0.0195	HBL	0.126	0.280	5.57	24.47	93.97	43.872	1.69	1.74	(1)	(32)	
12 IRASF01475-0740	0.0177	HBL	—	0.046	21.50	—	372.39	44.384	2.19	—	(7)		
13 MRK1034NED02	0.0338	Sy1	0.031	0.087	—	—	> 77.62	> 44.275	—	—			L
14 ESO545-G013	0.0337	Sy1	0.119	0.250	4.19	—	62.37	44.178	—	—	(8)		
15 NGC0931=Mrk1040	0.0167	Sy1	<0.029	<0.188	29.19	62.22	498.88	44.460	2.01	2.09	(6)	(32)	
16 NGC1068	0.0038	HBL	1.714	3.778	76.40	37.90	8994.98	44.421	1.84	1.82	(6)	(32)	
17 NGC1056	0.0052	NSy	—	—	—	—	—	—	—	—			N
18 NGC1097	0.0042	LIN	0.182	—	2.39	—	53.09	42.279	1.80	—	(9)		
19 NGC1125	0.0109	HBL	0.052	0.143	12.50	16.23	164.06	43.602	1.9	2.13	(6)	(32)	
20 NGC1144	0.0288	Sy2	0.003	0.032	26.40	74.31	492.04	44.935	1.69	1.73	(6)	(32)	
21 MCG-02-08-039	0.0299	HBL	—	—	3.75	—	83.56	44.199	1.9	—	(1)		
22 NGC1194	0.0136	Sy1	0.012	0.019	42.50	36.22	583.45	44.347	1.9	1.86	(6)	(32)	
23 NGC1241	0.0135	Sy2	—	0.058	—	11.64	> 117.22	> 43.644	—	—		(32)	L
24 NGC1320=MRK607	0.0089	Sy2	0.092	0.173	29.30	13.13	390.84	43.802	1.9	—	(1)	(32)	
25 NGC1365	0.0055	Sy1	—	—	44.15	63.52	893.31	43.741	2.81	1.99	(1)	(32)	
26 NGC1386	0.0029	HBL	0.051	0.202	97.90	—	1892.34	43.509	3.35	—	(10)		
27 IRASF03362-1642	0.0369	SY2	—	—	—	—	> 18.66	> 43.735	—	—			L
28 IRASF03450+0055	0.0310	Sy1	3.241	4.740	—	—	> 159.96	> 44.512	—	—			L
29 NGC1566	0.0050	Sy1	—	—	5.34	19.54	102.57	42.717	1.73	1.96	(11)	(32)	
30 3C120	0.0330	Sy1	—	—	42.52	95.38	977.24	45.354	1.75	2.01	(1)	(32)	
31 MRK0618	0.0356	Sy1	2.135	1.450	8.37	18.30	192.75	44.717	2.08	2.00	(1)	(32)	
32 IRASF04385-0828	0.0151	HBL	—	—	4.70	—	164.44	43.889	1.60	—	(12)		
33 NGC1667	0.0152	Sy2	<0.070	<0.171	11.53	—	148.59	43.851	1.9	—			
34 ESO033-G002	0.0181	Sy2	0.083	0.080	6.70	24.49	176.20	44.078	1.82	2.04	(13)	(32)	
35 ESO362-G018	0.0124	Sy1	2.598	1.350	6.90	48.89	229.09	43.861	1.53	—	(1)	(32)	
36 IRASF05189-2524	0.0426	HBL	0.078	0.185	5.80	9.71	610.94	45.378	2.08	2.06	(6)	(32)	
37 ESO253-G003	0.0425	Sy2	0.585	0.805	—	15.51	> 123.31	> 44.681	—	—		(32)	L
38 IRASF05563-3820	0.0339	Sy1	0.064	0.155	46.26	27.45	891.25	45.338	1.67	2.47	(1)	(32)	
39 MRK0006	0.0188	Sy1	0.054	0.495	15.04	56.70	408.32	44.477	1.50	1.91	(1)	(32)	
40 MRK0009	0.0399	Sy1	—	—	6.80	9.84	124.45	44.629	1.86	2.23	(6)	(32)	
41 MRK0079	0.0222	Sy1	2.572	2.819	54.07	42.72	709.58	44.864	1.57	2.13	(1)	(32)	
42 IRASF07599+6508	0.1483	Sy1	0.644	3.100	—	—	> 239.33	> 46.119	—	—			L
43 NGC2639	0.0111	Sy1	<0.011	<0.058	2.06	—	805.38	44.309	1.9	—	(14)		

Table 10. continued.

Table 10. High frequency nuclear photometry of the AGN sample (Note: This table is the full version of Table 3 and will be published in electronic form).

n. Name	z	Type	F_{NUV}	F_{FUV}	$F_{2-10keV}$	$F_{14-195keV}$	F_{bol}	L_{bol}	Γ_1	Γ_2	Ref ₁	Ref ₂	Flag
(1)	(2)	(3)	(4)	(5)	(6)	(7)	(8)	(9)	(10)	(11)	(12)	(13)	(14)
			(mJy)		$(10^{-12} \text{ergs}^{-1} \text{cm}^{-2})$			$\log(\text{erg s}^{-1})$					
44 IRASF08572+3915	0.0583	LIN	0.020	0.047	—	—	> 416.87	> 45.495	—	—			L
45 MRK0704	0.0292	Sy1	1.584	2.083	12.44	36.84	387.26	44.844	1.73	2.02	(1)	(32)	
46 UGC05101	0.0394	LIN	0.005	0.025	5.40	7.13	251.19	44.923	1.00	2.11	(15)	(32)	
47 NGC2992	0.0077	Sy1	0.015	0.046	89.67	32.65	903.65	44.039	1.59	1.89	(1)	(32)	
48 MRK1239	0.0199	Sy1	0.407	0.672	3.70	—	456.04	44.575	—	—	(16)		
49 M81=NGC3031	0.00014	LIN	0.385	0.945	10.50	20.26	297.85	40.071	1.83	1.99	(6)	(32)	
50 3C234	0.1849	Sy1	0.139	0.090	3.73	5.82	132.13	46.073	1.31	2.28	(6)	(32)	
51 NGC3079	0.0037	Sy2	0.046	0.060	38.0	36.74	609.54	43.228	2.42	1.77	(17)	(32)	
52 NGC3227	0.0039	Sy1	—	0.280	29.07	112.47	580.76	43.254	1.54	2.08	(18)	(32)	
53 NGC3511	0.0037	Sy1	—	0.093	—	—	—	—	—	—			N
54 NGC3516	0.0088	Sy1	2.112	3.604	30.70	112.42	644.17	44.009	2.03	1.93	(6)	(32)	
55 MCG+00-29-023	0.0249	Sy2	—	—	—	—	> 14.49	> 43.275	—	—			L
56 NGC3660	0.0123	Sy2	0.284	0.166	2.43	—	40.36	43.099	—	—	(19)		
57 NGC3982	0.0037	HBL	—	0.219	208.6	—	2618.18	43.862	1.83	—	(10)		
58 NGC4051	0.0023	Sy1	1.699	—	25.2	42.49	570.16	42.786	1.70	2.22	(10)	(32)	
59 UGC07064	0.0250	HBL	0.158	0.319	2.70	13.48	53.95	43.850	1.67	1.69	(6)	(32)	
60 NGC4151	0.0033	Sy1	3.488	0.051	210.0	618.88	3349.65	43.869	1.73	1.88	(20)	(32)	
61 NGC4253=MRK766	0.0129	Sy1	0.199	0.414	28.0	26.17	489.78	44.225	2.02	2.26	(21)	(32)	
62 NGC4388	0.0084	HBL	0.158	0.313	47.54	278.91	859.01	44.093	1.60	1.77	(1)	(32)	
63 3C273	0.1583	Sy1	17.320	11.24	106.30	421.57	7177.94	47.658	1.58	1.75	(1)	(32)	
64 NGC4501=M88	0.0076	Sy2	0.021	0.025	2.31	—	56.62	42.824	4.05	—	(10)		
65 NGC4579=M58	0.0051	LIN	0.242	0.456	3.91	8.27	552.08	43.466	1.78	—	(1)	(32)	
66 NGC4593	0.0090	Sy1	<0.129	<3.961	61.26	88.30	879.02	44.163	2.03	1.84	(22)	(32)	
67 NGC4594=M104	0.0034	LIN	0.138	0.247	1.39	—	59.57	42.145	1.95	—	(1)		
68 NGC4602	0.0085	Sy1	0.012	0.039	—	—	> 0.16	> 40.384	—	—			L
69 TOL1238-36=I3639	0.0109	HBL	0.312	0.665	38.98	—	609.54	44.172	—	—	(10)		
70 M-2-33-34=N4748	0.0146	Sy1	1.568	2.268	8.32	9.35	134.90	43.773	1.91	2.06	(23)	(32)	
71 MRK0231	0.0422	Sy1	—	—	2.98	—	> 928.97	> 45.552	1.66	—	(1)		L
72 NGC4922	0.0236	Sy2	0.004	0.010	1.48	—	> 1066.60	> 45.095	—	—	(10)		L
73 NGC4941	0.0037	Sy2	<0.045	<0.042	5.48	20.16	240.44	42.825	1.95	1.64	(6)	L (32)	
74 NGC4968	0.0099	Sy2	<0.052	<0.072	68.3	—	781.63	44.196	1.33	—	(1)		
75 NGC5005	0.0032	LIN	<0.083	<0.094	0.61	—	> 57.02	> 42.074	1.57	—	(10)		L
76 NGC5033	0.0029	Sy1	<0.023	<0.081	4.2	6.26	79.07	42.130	1.72	1.63	(6)	(32)	
77 MCG-03-34-064	0.0165	HBL	0.390	0.486	12.32	30.98	567.54	44.505	2.50	2.20	(1)	(32)	
78 NGC5135	0.0137	Sy2	0.480	1.578	44.90	—	595.66	44.363	—	—	(24)		
79 NGC5194=M51A	0.0015	Sy2	—	0.676	4.7	13.26	121.06	41.741	2.61	—	(1)	(32)	
80 MCG-06-30-015	0.0077	Sy1	0.060	0.156	44.9	59.53	770.90	43.970	2.09	2.47	(1)	(32)	
81 IRASF13349+2438	0.1076	Sy1	0.165	0.527	2.36	—	451.86	46.093	2.31	—	(1)		
82 NGC5256=Mrk266	0.0279	Sy2	<0.087	<0.155	0.86	—	52.48	43.935	2.74	—	(1)		
83 MRK0273	0.0378	LIN	0.052	0.087	3.5	5.18	125.03	44.582	2.25	—	(14)	(32)	
84 IC4329A	0.0161	Sy1	0.007	0.080	168.	263.25	2679.17	45.158	1.89	2.05	(25)	(32)	

Table 10. continued.

Table 10. High frequency nuclear photometry of the AGN sample (Note: This table is the full version of Table 3 and will be published in electronic form).

n. Name	z	Type	F_{NUV}	F_{FUV}	$F_{2-10keV}$	$F_{14-195keV}$	F_{bol}	L_{bol}	Γ_1	Γ_2	Ref ₁	Ref ₂	Flag
(1)	(2)	(3)	(4)	(5)	(6)	(7)	(8)	(9)	(10)	(11)	(12)	(13)	(14)
			(mJy)		$(10^{-12} \text{ergs}^{-1} \text{cm}^{-2})$			$\log(\text{erg s}^{-1})$					
85 NGC5347	0.0078	HBL	0.051	—	7.44	—	196.34	43.388	—	—	(26)		
86 MRK0463=UGC8850	0.0504	HBL	—	—	17.0	8.48	438.53	45.386	1.64	1.71	(10)	(32)	
87 NGC5506	0.0062	Sy2	0.036	0.174	69.3	239.40	1778.28	44.144	1.80	2.11	(1)	(32)	
88 NGC5548	0.0172	Sy1	0.781	1.792	35.04	86.47	526.02	44.509	1.82	1.91	(1)	(32)	
89 MRK0817	0.0315	Sy1	6.230	5.044	13.60	28.77	393.55	44.918	2.14	1.86	(6)	(32)	
90 IRASF15091-2107	0.0446	Sy1	<0.064	<0.182	16.86	32.67	365.59	45.197	1.99	1.97	(6)	(32)	
91 NGC5929	0.0083	HBL	0.088	0.123	1.4	—	78.34	43.043	—	—	(27)		
92 NGC5953	0.0066	LIN	0.120	0.484	0.01	—	> 12.47	> 42.045	—	—	(28)		L
93 ARP220=UGC9913	0.0181	Sy2	<0.030	<0.034	0.11	—	> 107.65	> 43.865	—	—	(29)		L
94 N5995=M-2-40-4	0.0252	HBL	0.056	0.176	14.90	35.21	420.73	44.749	1.67	2.05	(6)	(32)	
95 IRASF15480-0344	0.0303	HBL	—	—	4.60	—	197.24	44.583	5.66	—	(1)		
96 ESO141-G055	0.0371	Sy1	11.82	11.21	26.5	58.77	645.65	45.279	2.05	2.06	(25)	(32)	
97 IRASF19254-7245	0.0617	HBL	0.009	0.025	33.28	—	533.33	45.653	1.9	—	(30)		
98 NGC6810	0.0068	SB	0.024	0.231	0.08	—	46.99	42.647	1.9	—	(1)		
99 NGC6860	0.0149	Sy1	—	—	25.60	51.52	413.05	44.278	2.11	2.05	(6)	(32)	
100 NGC6890	0.0081	Sy2	0.044	0.125	10.2	—	273.53	43.565	3.87	—	(1)		
101 MRK0509	0.0344	Sy1	9.498	6.855	170.80	100.14	2009.09	45.705	1.67	2.08	(31)	(32)	
102 IC5063	0.0113	HBL	0.031	0.123	41.1	67.76	810.96	44.328	1.90	1.90	(6)	(32)	
103 MRK0897	0.0263	Sy2	0.335	0.873	—	—	> 70.47	> 44.011	—	—			L
104 NGC7130	0.0162	Sy2	0.324	1.200	11.9	17.41	230.14	44.097	2.03	1.88	(24)	(32)	
105 NGC7172	0.0087	Sy2	—	—	34.10	160.02	623.73	43.984	1.46	1.84	(6)	(32)	
106 IRASF22017+0319	0.0611	HBL	—	0.251	7.20	16.16	212.32	45.244	1.69	2.24	(6)	(32)	
107 NGC7213	0.0058	LIN	—	—	62.92	39.04	767.36	43.720	1.91	1.90	(1)	(32)	
108 3C445	0.0562	Sy1	—	—	24.40	39.82	308.32	45.331	1.74	2.04	(6)	(32)	
109 NGC7314	0.0048	HBL	0.029	0.078	41.80	57.42	540.75	43.404	2.14	1.94	(6)	(32)	
110 MCG+03-58-007	0.0315	HBL	—	—	2.13	—	118.30	44.396	1.9	—	(1)		
111 NGC7469	0.0163	Sy1	1.603	2.368	25.19	70.63	883.08	44.686	2.09	2.08	(1)	(32)	
112 NGC7496	0.0055	Sy2	1.090	1.978	—	—	> 79.62	> 42.691	—	—			L
113 NGC7582	0.0053	Sy2	0.012	0.205	59.86	82.28	1169.50	43.825	1.89	2.13	(1)	(32)	
114 NGC7590	0.0053	Sy2	0.048	0.133	—	—	> 97.95	> 42.748	—	—			L
115 NGC7603	0.0295	Sy1	3.769	4.434	22.40	52.96	496.59	44.961	1.88	1.93	(6)	(32)	
116 NGC7674	0.0289	HBL	0.297	0.377	20.13	12.60	493.17	44.940	3.28	—	(1)	(32)	
117 CGCG381-051	0.0307	Sy2	0.031	—	—	—	> 26.55	> 43.724	—	—			L

Table 10. continued.

Table 10. High frequency nuclear photometry of the AGN sample (Note: This table is the full version of Table 3 and will be published in electronic form).

n. Name	z	Type	F_{NUV}	F_{FUV}	$F_{2-10keV}$	$F_{14-195keV}$	F_{bol}	L_{bol}	Γ_1	Γ_2	Ref ₁	Ref ₂	Flag
			(mJy)			(10^{-12} ergs $^{-1}$ cm $^{-2}$)		log(erg s $^{-1}$)					
(1)	(2)	(3)	(4)	(5)	(6)	(7)	(8)	(9)	(10)	(11)	(12)	(13)	(14)

Notes. The columns give for each AGN in the sample: (1) name; (2) AGN type: Sy1 = Seyfert type 1; Sy2 = Seyfert type 2; HBL = Hidden Broad Line Region AGN; LIN = LINER galaxy; (3) redshift; (4) (4) Near-ultraviolet flux (NUV) from the Mikulski Archive for Space Telescopes (MAST, [Conti et al. 2011](#)) GALEX Catalog Search; (5) Far-ultraviolet flux (FUV) from the Mikulski Archive for Space Telescopes (MAST, [Conti et al. 2011](#)) GALEX Catalog Search; (6) 2-10 keV absorption corrected X-ray flux from the references of column (10); (7) 14-195 keV observed X-ray flux from the references of column (11); (8) Computed bolometric flux (see text); (9) Logarithm of the total (bolometric) luminosity; (10) photon index of the 2-10 keV observations Γ_1 , from either [Brightman & Nandra \(2011\)](#) or [Ricci et al. \(2017\)](#); (11) photon index of the 14-195 keV observations Γ_2 , from [Oh et al. \(2018\)](#); (12) reference of the 2-10keV flux, Ref₁: (1): derived from the absorption corrected luminosity of [Brightman & Nandra \(2011\)](#), (2): derived from the absorption corrected luminosity of [Guainazzi et al. \(2005\)](#), (3): [Ghosh & Soundararajaperumal \(1992\)](#), (4): [Reeves & Turner \(2000\)](#), (5): derived from the absorption corrected luminosity of [Tan et al. \(2012\)](#), (6): [Ricci et al. \(2017\)](#), (7): derived from the absorption corrected luminosity of [Marinucci et al. \(2012\)](#), (8): [Bi et al. \(2020\)](#), (9): derived from the absorption corrected luminosity of [Iyomoto et al. \(1996\)](#), (10): derived from the absorption corrected luminosity of [Saade et al. \(2022\)](#), (11): derived from the absorption corrected luminosity of [Levenson et al. \(2009\)](#), (12): [Rivers et al. \(2013\)](#), (13): [Walton et al. \(2021\)](#), (14): [Bassani et al. \(1999\)](#), (15): [Tanimoto et al. \(2022\)](#), (16): [Della Ceca et al. \(2008\)](#), (17): [Iyomoto et al. \(2001\)](#), (18): [Boissay et al. \(2016\)](#), (19): [Brightman & Nandra \(2008\)](#), (20): derived from the absorption corrected luminosity of [Akylas & Georgantopoulos \(2009\)](#), (21): [Chen et al. \(2022\)](#), (22): derived from the absorption corrected luminosity of [Zhou & Zhang \(2010\)](#), (23): [Vasylenko \(2018\)](#), (24): derived from the absorption corrected luminosity of [Yamada et al. \(2023\)](#), (25): [Lutz et al. \(2004\)](#), (26): [Osorio-Clavijo et al. \(2022\)](#), (27): [Cardamone et al. \(2007\)](#), (28): [Osorio-Clavijo et al. \(2023\)](#), (29): [Corral et al. \(2014\)](#), (30): [Braitto et al. \(2009\)](#), (31): [Zhou & Zhang \(2010\)](#); (13) reference of the 14-195keV flux, Ref₂: (32): [Oh et al. \(2018\)](#), (33): [Deluit \(2004\)](#), (34): [Cusumano et al. \(2010\)](#); (14) Bolometric flux/luminosity flag: L = lower limit to the bolometric flux and luminosity; N = data not available for a proper integration of bolometric flux and luminosity.

APPENDIX

A. SED OF ALL GALAXIES OF THE SAMPLE

We present in Fig. 21 and Fig. 22 the individual SEDs of all Seyfert type 1 in our sample. We present in Fig. 23 the individual SEDs of all HBL galaxies. We present in Fig. 24 the individual SEDs of all Seyfert type 2. We present in Fig. 25 the individual SEDs of the LINER in our sample (two panels above) and the SEDs of those classified as non-Seyfert (NGC 1056) and Starburst (NGC 6810) (lower panel).

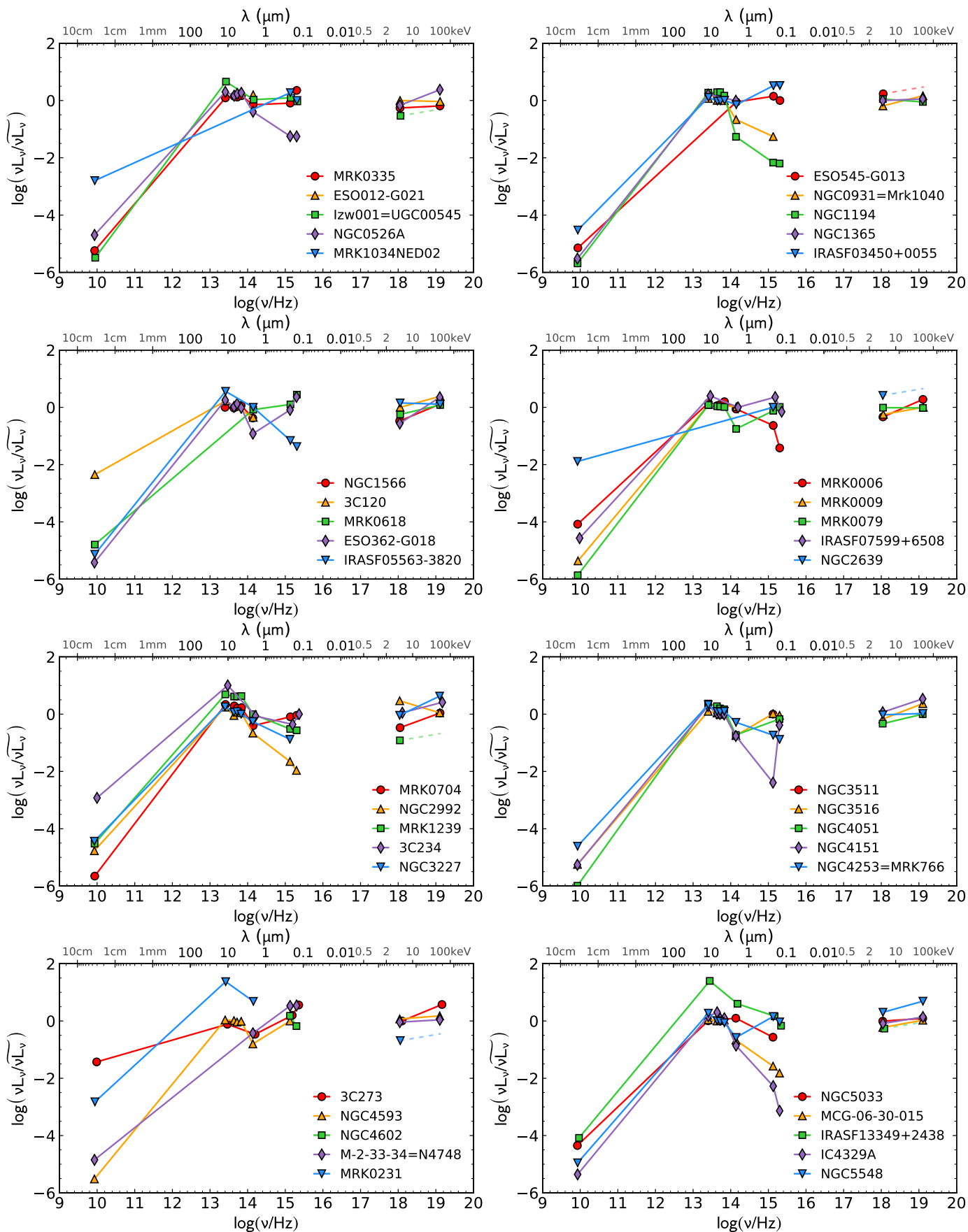


Figure 21. Normalized rest-frame SEDs of Seyfert type 1.

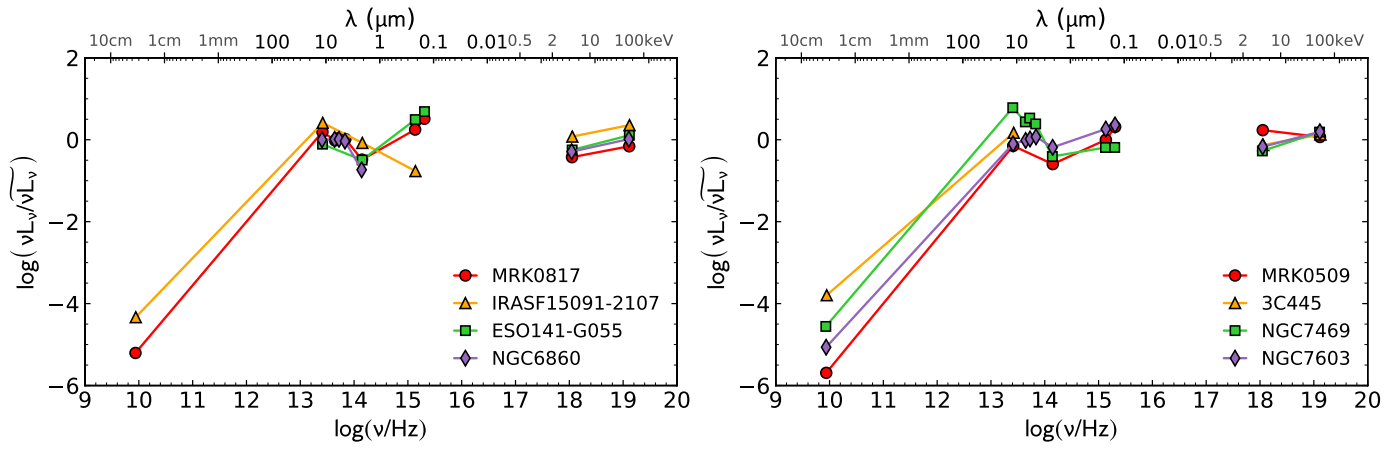


Figure 22. Normalized rest-frame SEDs of Seyfert type 1 (continued).

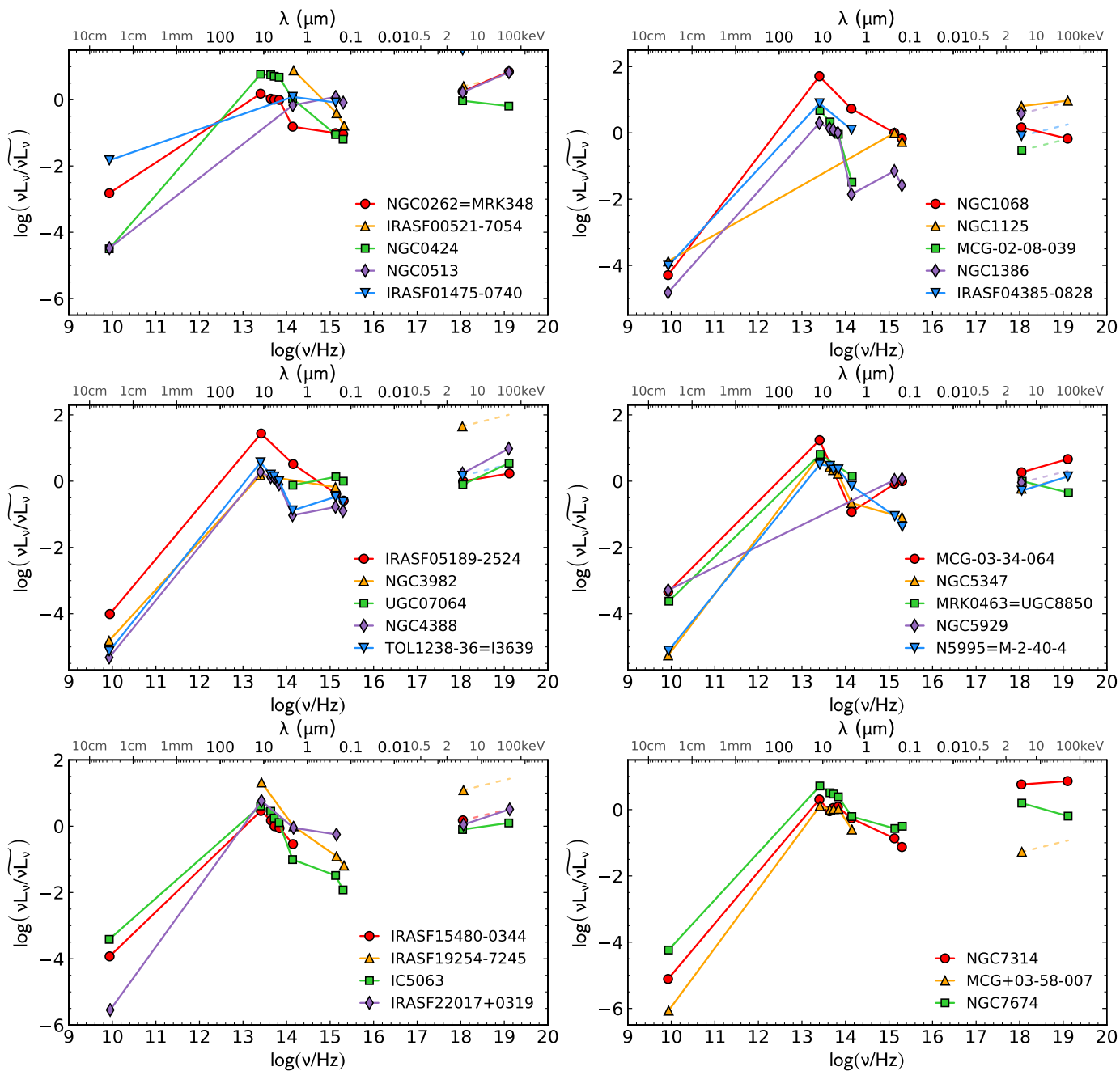


Figure 23. Normalized rest-frame SEDs of Hidden Broad Line Region Galaxies (Type 1).

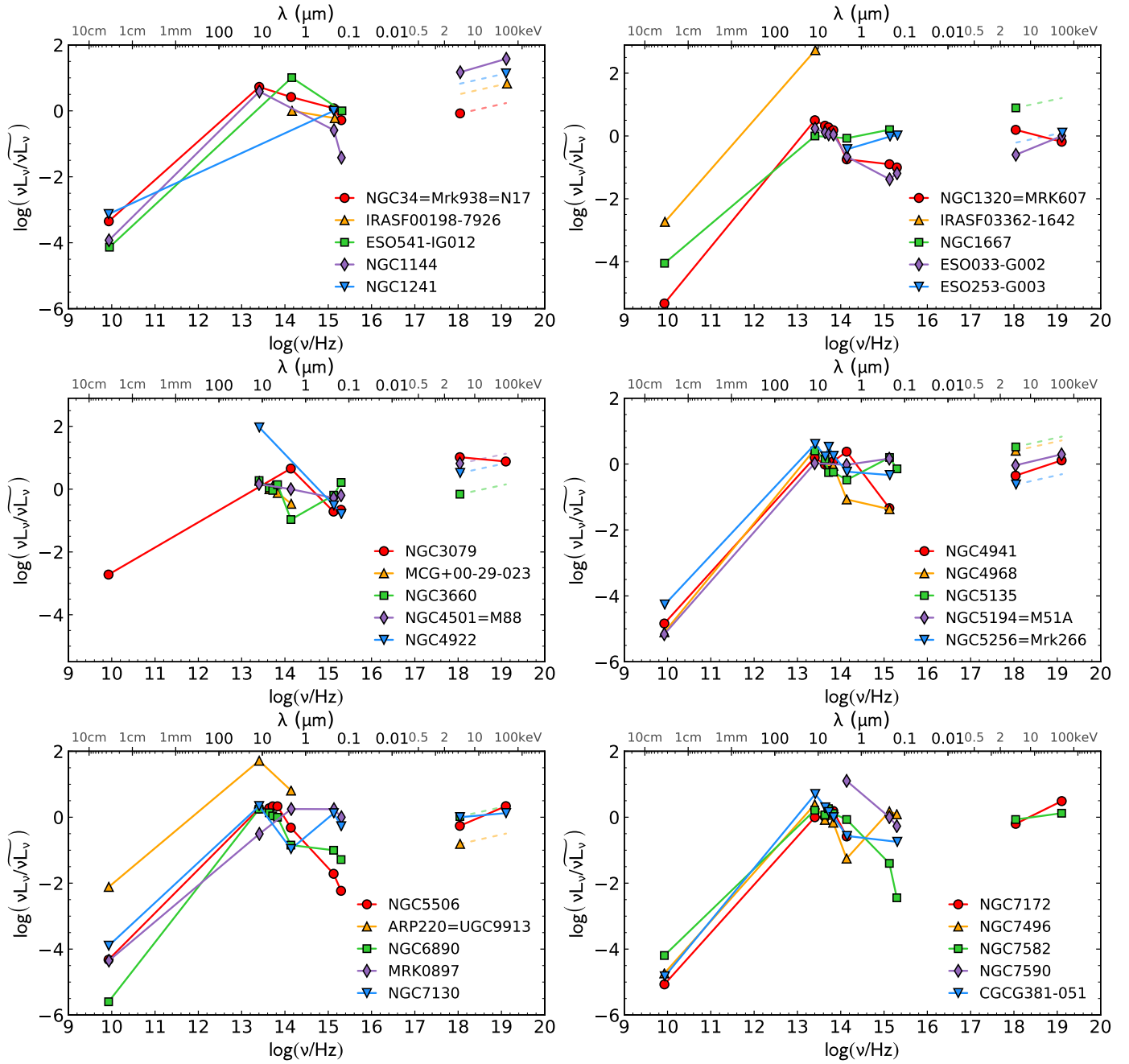


Figure 24. Normalized rest-frame SEDs of Seyfert type 2.

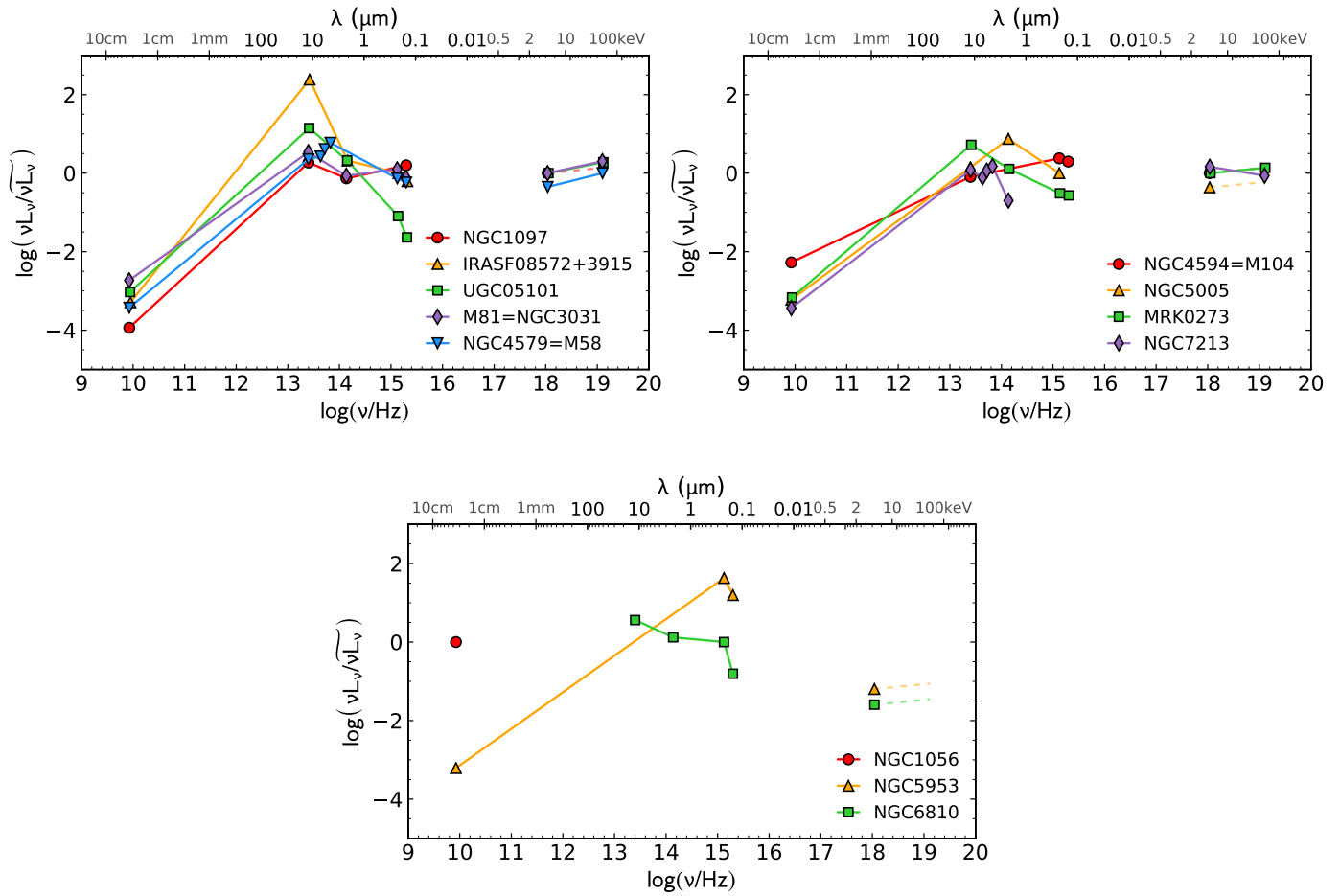


Figure 25. Normalized rest-frame SEDs of LINERs, in the above two panels and **two non-Seyfert galaxies (NGC 1056 and NGC 5953)**, one Starburst (NGC 6810) galaxies in the lower panel.

B. CORRELATIONS OF LUMINOSITIES NORMALIZED TO THE EDDINGTON LUMINOSITY

We show in Fig.26a and b the correlations of the $12\mu\text{m}$ and $[\text{OIV}]26\mu\text{m}$ line luminosities normalized to the Eddington luminosity (L_{EDD}) as a function of the ratio of $L_{\text{BOL}}/L_{\text{EDD}}$. We show in Fig.27a and b the correlations of the 2-10 keV and 14-195 keV luminosities normalized to the Eddington luminosity (L_{EDD}) as a function of the ratio of $L_{\text{BOL}}/L_{\text{EDD}}$. We show in Fig.26a and b the correlations of the composite ($12\mu\text{m}$ and $[\text{OIV}]26\mu\text{m}$) and ($12\mu\text{m}$ and $[\text{NeV}]14.3\mu\text{m}$) luminosities to the Eddington luminosity (L_{EDD}) as a function of the ratio of $L_{\text{BOL}}/L_{\text{EDD}}$. We present in Table 11 the results of the correlations of the $12\mu\text{m}$, $[\text{OIV}]26\mu\text{m}$ line, 2-10 keV and 14-195 keV luminosities normalized to the Eddington luminosity, as well as the combined continuum and line luminosities.

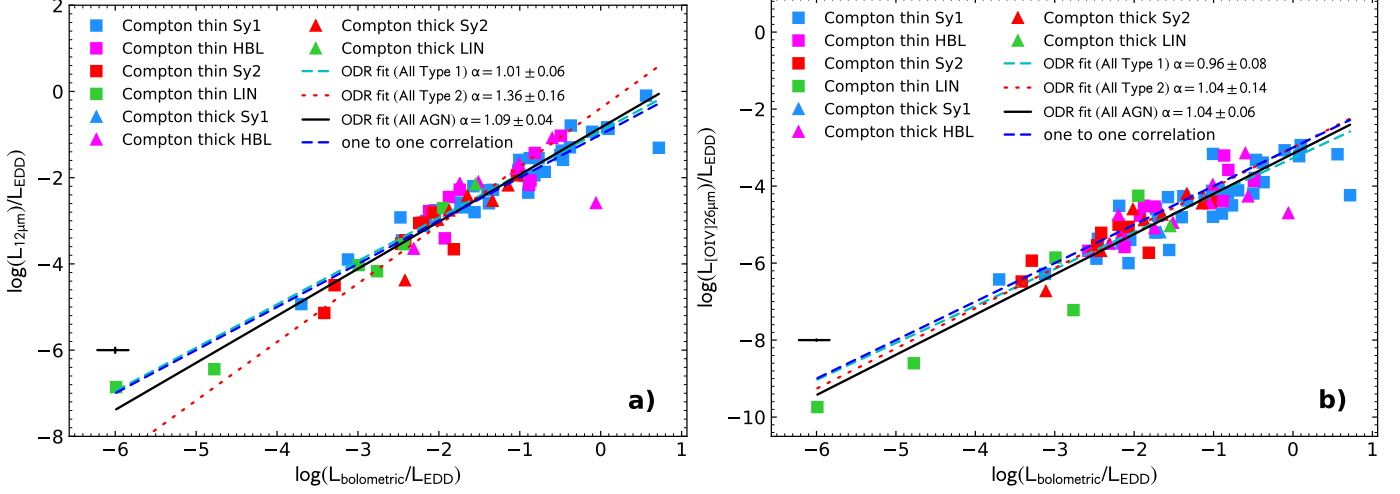


Figure 26. In each figure representing the correlations between physical quantities, the error bar at the left corner has been computed using the median value of the relative errors of the plotted data (from Fig. 26 to Fig. 29). **(a):** Ratio of the $12\mu\text{m}$ luminosity to the Eddington luminosity as a function of the ratio of the bolometric luminosity to the Eddington luminosity. **(b):** Ratio of the $[\text{OIV}]26\mu\text{m}$ luminosity to the Eddington luminosity as a function of the ratio of the bolometric luminosity to the Eddington luminosity.

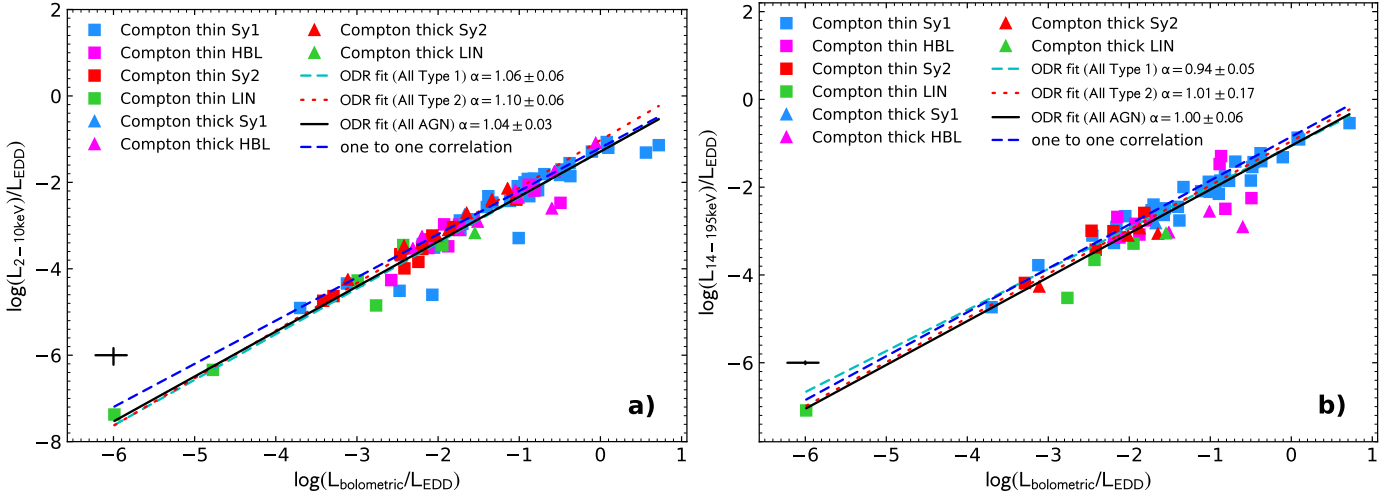


Figure 27. (a): Ratio of the 2-10 keV corrected luminosity to the Eddington luminosity as a function of the ratio of the bolometric luminosity to the Eddington luminosity. **(b):** Ratio of the (10-195) keV observed luminosity to the Eddington luminosity as a function of the ratio of the bolometric luminosity to the Eddington luminosity.

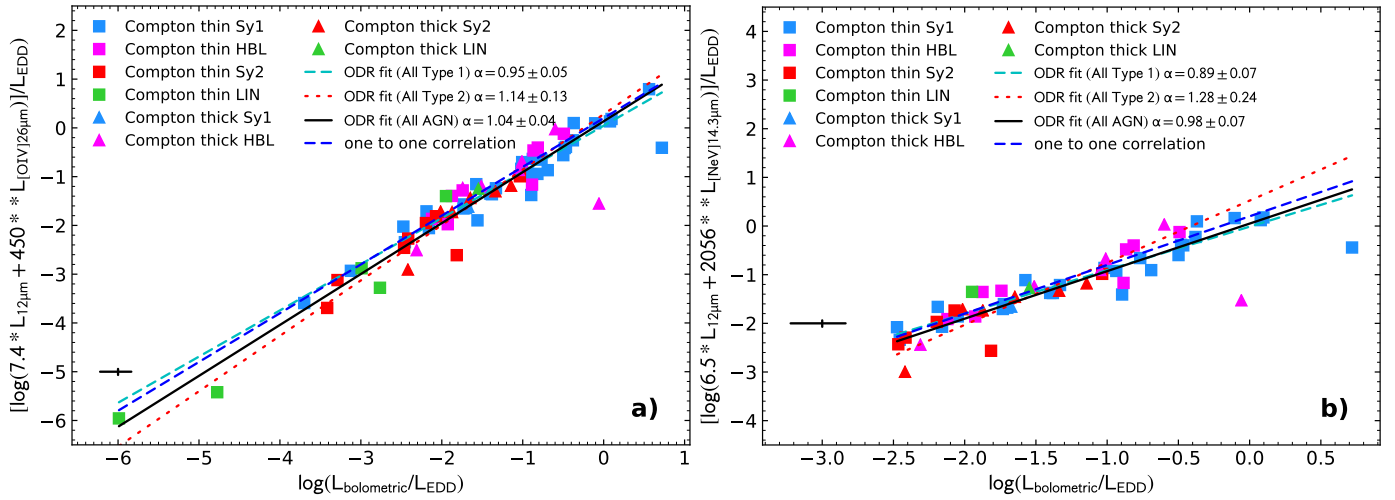


Figure 28. (a) Ratio of the composite $12\mu\text{m}$ and $[\text{OIV}]26\mu\text{m}$ luminosity to the Eddington luminosity as a function of the ratio of the bolometric luminosity to the Eddington luminosity. (b) Ratio of the composite $12\mu\text{m}$ and $[\text{NeV}]14.3\mu\text{m}$ luminosity to the Eddington luminosity as a function of the ratio of the bolometric luminosity to the Eddington luminosity.

Table 11. Correlation of various bands luminosities normalized to the Eddington luminosity with the bolometric luminosities, normalized to the Eddington luminosity.

Considered variables	Subset	N	ρ	(P_{null})	$\beta \pm \Delta\beta$	$\alpha \pm \Delta\alpha$	σ
(1)	(2)	(3)	(4)	(5)	(6)	(7)	(7)
$L_{12\mu\text{m}}^{\text{unc}}/L_{\text{EDD}}$ vs. $L_{\text{bol}}/L_{\text{EDD}}$	All	71	0.95	(9.6×10^{-36})	-0.84 ± 0.08	1.09 ± 0.04	0.075
" " "	Type 1	41	0.94	(2.9×10^{-20})	-0.92 ± 0.08	1.01 ± 0.05	0.051
" " "	Type 2	15	0.91	(2.3×10^{-6})	-0.39 ± 0.36	1.36 ± 0.16	0.056
$L_{[\text{OIV}]26\mu\text{m}}/L_{\text{EDD}}$ vs. $L_{\text{bol}}/L_{\text{EDD}}$	all	77	0.90	(8.5×10^{-29})	-3.16 ± 0.11	1.04 ± 0.06	0.131
" " "	Type 1	46	0.85	(6.4×10^{-14})	-3.27 ± 0.13	0.96 ± 0.08	0.125
" " "	Type 2	15	0.88	(1.2×10^{-5})	-3.00 ± 0.32	1.04 ± 0.14	0.069
$L_{2-10\text{keV}}/L_{\text{EDD}}$ vs. $L_{\text{bol}}/L_{\text{EDD}}$	all	79	0.96	(3.0×10^{-46})	-1.27 ± 0.06	1.04 ± 0.03	0.046
" " "	Type 1	46	0.94	(4.0×10^{-22})	-1.29 ± 0.09	1.06 ± 0.06	0.055
" " "	Type 2	16	0.98	(1.0×10^{-10})	-1.02 ± 0.15	1.10 ± 0.06	0.014
$L_{14-195\text{keV}}/L_{\text{EDD}}$ vs. $L_{\text{bol}}/L_{\text{EDD}}$	all	60	0.95	(1.0×10^{-30})	-1.06 ± 0.08	1.00 ± 0.04	0.059
" " "	Type 1	41	0.95	(5.3×10^{-21})	-1.06 ± 0.07	0.94 ± 0.05	0.039
" " "	Type 2	9	0.90	(9.1×10^{-4})	-0.95 ± 0.41	1.01 ± 0.17	0.037
$(7.4 \times L_{12\mu\text{m}}^{\text{unc}} + 450 \times L_{[\text{OIV}]26\mu\text{m}})/L_{\text{EDD}}$ vs. $L_{\text{bol}}/L_{\text{EDD}}$	all	69	0.95	(7.2×10^{-36})	0.13 ± 0.08	1.04 ± 0.04	0.063
" " "	Type 1	41	0.95	(5.7×10^{-21})	0.04 ± 0.07	0.95 ± 0.05	0.044
" " "	Type 2	14	0.92	(3.5×10^{-6})	0.28 ± 0.29	1.14 ± 0.13	0.049
$(6.5 \times L_{12\mu\text{m}}^{\text{unc}} + 2056 \times L_{[\text{NeV}]14.3\mu\text{m}})/L_{\text{EDD}}$ vs. $L_{\text{bol}}/L_{\text{EDD}}$	all	55	0.88	(1.5×10^{-18})	0.05 ± 0.10	0.98 ± 0.07	0.074
" " "	Type 1	34	0.92	(2.4×10^{-14})	-0.016 ± 0.09	0.89 ± 0.07	0.050
" " "	Type 2	12	0.83	(7.2×10^{-4})	0.52 ± 0.47	1.28 ± 0.24	0.053

Notes. Fit results. The columns give for each correlation: (1) variables; (2) Subset of the sample on which the fit was computed: "all" indicates the entire sample and Type 1 and Type 2 the Seyfert type subsets; (3) Number of sources; (4) Pearson correlation coefficient ρ (1: completely correlated variables, 0: uncorrelated variables) with the relative null hypothesis (zero correlation) probability; (5) and (6): Parameters of the linear regression fit using the equation: $\log(L_y) = \beta + \alpha \times \log(L_x)$; (7): residual variance of the fit σ .

C. FLUX-FLUX CORRELATIONS

We show in Fig.29a and b the correlations of the 2-10 keV flux and the K-band $2.2\mu\text{m}$ flux density with the bolometric flux.

We present in Table 12 the results of the correlations of the $12\mu\text{m}$, [OIV] $26\mu\text{m}$ line, 2-10 keV and K-band fluxes with the computed bolometric flux.

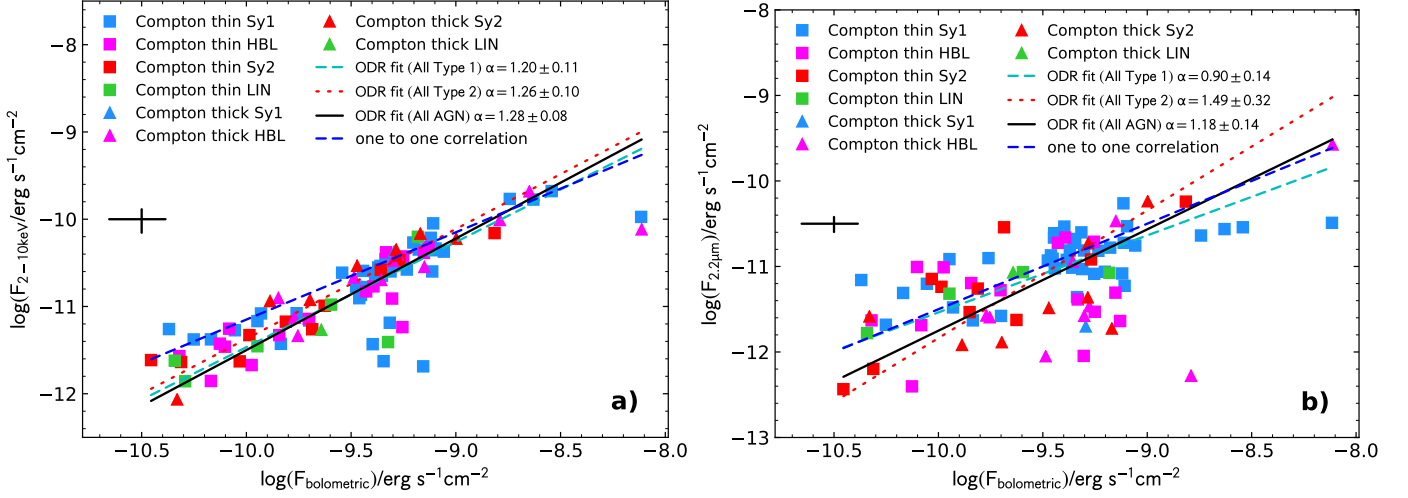


Figure 29. (a:) 2-10 keV flux as a function of the estimated bolometric flux. (b:) Nuclear K band flux as a function of the estimated bolometric flux.

Table 12. Correlation of various bands fluxes with the bolometric fluxes.

Considered variables (1)	Subset (2)	N (3)	ρ (P_{null}) (4)	$\beta \pm \Delta\beta$ (5)	$\alpha \pm \Delta\alpha$ (6)	σ (7)
$F(12\mu\text{m})_{\text{nuc}}$ vs. $F(\text{bolometric})$	All	83	0.69 (3.5×10^{-13})	1.27 ± 1.11	1.23 ± 0.12	0.077
" " "	Type 1	48	0.60 (7.4×10^{-6})	-2.11 ± 1.21	0.87 ± 0.13	0.056
" " "	Type 2	17	0.73 (8.9×10^{-4})	3.25 ± 2.90	1.45 ± 0.30	0.082
$F([\text{OIV}]26\mu\text{m})$ vs. $F(\text{bolometric})$	all	94	0.51 (1.9×10^{-7})	-0.36 ± 1.60	1.37 ± 0.17	0.133
" " "	Type 1	57	0.44 (7.2×10^{-4})	-0.97 ± 2.00	1.23 ± 0.21	0.128
" " "	Type 2	18	0.62 (5.7×10^{-3})	-0.66 ± 2.91	1.24 ± 0.30	0.097
$F(2-10\text{keV})$ vs. $F(\text{bolometric})$	all	95	0.84 (2.3×10^{-26})	1.29 ± 0.75	1.28 ± 0.08	0.045
" " "	Type 1	57	0.81 (4.4×10^{-14})	0.58 ± 1.01	1.20 ± 0.11	0.047
" " "	Type 2	18	0.95 (1.7×10^{-9})	1.21 ± 0.98	1.26 ± 0.10	0.014
$F(2.2\mu\text{m})_{\text{nuc}}$ vs. $F(\text{bolometric})$	all	88	0.56 (1.1×10^{-8})	0.10 ± 1.29	1.18 ± 0.14	0.110
" " "	Type 1	54	0.54 (2.1×10^{-5})	-2.53 ± 1.29	0.90 ± 0.14	0.089
" " "	Type 2	18	0.70 (1.2×10^{-3})	3.09 ± 3.11	1.49 ± 0.32	0.088

Notes. Fit results. The columns give for each correlation: (1) variables; (2) Subset of the sample on which the fit was computed: "all" indicates the entire sample and Type 1 and Type 2 the Seyfert type subsets; (3) Number of sources; (4) Pearson correlation coefficient ρ (1: completely correlated variables, 0: uncorrelated variables) with the relative null hypothesis (zero correlation) probability; (5) and (6): Parameters of the linear regression fit using the equation: $\log(F_y) = \beta + \alpha \times \log(F_x)$; (7): residual variance of the fit σ .